Title
Novel Tools for Ocean Biogeochemical Models

Author
Bardin, Ann Marie

Publication Date
2014

Peer reviewed|Thesis/dissertation

UNIVERSITY OF CALIFORNIA,
IRVINE

Novel Analysis Tools for Ocean Biogeochemical Models

DISSERTATION

submitted in partial satisfaction of the requirements
for the degree of

DOCTOR OF PHILOSOPHY

in Earth System Science

by

Ann Marie Bardin

Dissertation Committee:
Associate Professor François Primeau, Chair
Associate Professor Adam Martiny
Professor Keith Moore
Professor Charles Zender

2014

TABLE OF CONTENTS

LIST OF FIGURES

LIST OF TABLES

ACKNOWLEDGMENTS

I thank François Primeau, my thesis advisor, for his contributions to this work, both direct and indirect, and for his unfailing support, patience, and technical guidance. Discussions of ideas and debates over technical issues have stimulated my thinking and progress. It has been a great opportunity and a great pleasure to study with him.

I thank my thesis committee members: François Primeau, Adam Martiny, Keith Moore, and Charles Zender for their participation in the annual reviews of my work, their guidance, and their review of this document.

I give special thanks to François Primeau, Keith Moore and Adam Martiny for the marine biogeochemistry seminar series, which has provided extensive and current background information as well as lively discussions on the subject.

I thank my coauthors for allowing me to include the material resulting from our joint efforts in this dissertation. The text of Chapter 2 of this dissertation is a reformatting of the material as it appears in Ocean Modelling. Co-author François Primeau directed and supervised research which forms the basis for Chapter 2 of the dissertation. I thank co-author of Chapter 2 Keith Lindsay for contributing the capability to interface with the CESM ocean model and information on the configuration for Chapter 2, and discussions on the ongoing developments of the CESM ocean model. I thank Elsevier Ltd. for permission to include the contents of Chapter 2, which was published in Ocean Modelling 73 (2014) 45-58.

I thank Keith Moore for his contribution of the Biogeochemical Ecological Cycling (BEC) simulation output used in the work documented in Chapter 4, for illuminating discussions of the characteristics of the CESM ocean component, and aid in setting up simulations using the CESM ocean model in Chapter 2.

I thank Kathe Todd-Brown for her constructive and insightful comments on Chapter 2. I thank Nathan Garcia and Kim Gallagher for their constructive comments on Chapter 4. I thank Robert Letscher and Elliot Sherman for insightful discussions on the BEC characteristics. I thank Bryce Bardin for editing support, for endless coffee, for encouragement, and discussions of climate change.

Chapter 2 of this work was supported by a grant from the Department of Energy Biological and Environmental Sciences Division. Chapter 3 of this work was supported by NSF grant OCE-0727229. Chapter 4 of this work was supported by a grant from the Department of Energy Biological and Environmental Sciences Division.

Computing resources for running the Community Earth System Model (CESM), the parent model of the offline model developed in this work, were provided by the Climate Simulation Laboratory at the National Center for Atmospheric Research's Computational and Information Systems Laboratory, sponsored by the National Science Foundation and other agencies.

CURRICULUM VITAE

Ann Marie Bardin

EDUCATION

Doctor of Philosophy in Earth System Science **2014**
University of California, Irvine Irvine, California

Master of Science in Earth System Science **2010**
University of California, Irvine Irvine, California

Bachelor of Science in Engineering Physics **1960**
University of Colorado Boulder, Colorado

ABSTRACT OF THE DISSERTATION

Novel Analysis Tools for Ocean Biogeochemical Models

By

Ann Marie Bardin

Doctor of Philosophy in Earth System Science

University of California, Irvine, 2014

Associate Professor François Primeau, Chair

Ocean general circulation models of the IPCC class have biases even when simulating present-day conditions, which may bring into question their predictions of future conditions. This dissertation is about tools for, and results from assessing biases in the Community Earth System Model (CESM) ocean component, by itself and when combined with the Biological Ecosystem Cycling (BEC) model. Newly developed tools and their applications are listed.

1. An offline matrix tracer transport model for the ocean component of CESM.
2. A fast Newton-Krylov implicit tracer equilibrium solver for both the annually-averaged and the seasonally-varying circulation.
3. An effective preconditioner for the solver simulating ^{14}C.

   Application results:

   For a natural ^{14}C simulation, an equilibrium solution was obtained in 23 model-years, a dramatic decrease from the 4000 model-years reported for time-stepping. The modeled circulation in the deep Pacific Ocean produced ^{14}C ages twice those of observations.

4. A capability for computing the surface origin of water mass fractions as well as the age of the various water masses.

   Application results:

   > The North Atlantic was the major supplier of ventilated water to not only the Atlantic, but also the Pacific and Indian Oceans. A lack of formation of bottom water in the Southern Ocean was discovered.

5. A capability for restricting the tracer simulation domain to a limited region of the ocean while retaining the effectiveness of advection and diffusion fields on the boundary. This reduces computational costs and allows separating local versus remote impacts of tracer sources on the biogeochemical tracer concentrations. This capability has the potential to provide a platform for further biogeochemical studies.

   Application results:

   > The Indian Ocean region was isolated. Global versus regional circulation effects were determined using ^{14}C. Most of the bias within the region was eliminated by using observational, rather than globally calculated values, on the boundaries. Oxygen production and consumption from a CMIP5 BEC simulation were used to drive a regional oxygen model. Boundary values of oxygen from the CMIP5 BEC simulation were replaced with observations, resulting in less bias within the region. However, significant bias in the location of the Arabian Sea oxygen minimum zone remained.

Chapter 1

Introduction

1.1 Motivation

It has been predicted that the oceans will lose oxygen in response to climate change (Bopp et al., 2013; Stramma et al., 2008; Matear and Hirst, 2003; Bopp et al., 2002). Observations suggest that a loss of oxygen from the ocean is already underway (Whitney et al., 2007; Chan et al., 2008; Stramma et al., 2012). Unfortunately, IPCC-class Earth System models have problems matching even the present-day 3-D oxygen fields, especially at low concentrations (Bopp et al., 2013), making it problematic to predict future conditions.

Oxygen in the ocean is a very integrative quantity with respect to multiple factors: the ocean circulation, the biological impacts of production and consumption, and the air-sea gas exchange. This makes oxygen an excellent metric by which to judge the fidelity of the entire biogeochemical and physical ocean system, and its role in the Earth system.

The impacts of losing oxygen in the ocean, and the challenges of making a good model representation of the mechanisms controlling oxygen, are the major motivation for the studies encompassed in this dissertation. Methods for determining the behaviors and biases of an ocean model are applied to the Community Earth System Model (CESM) ocean component, by itself and when combined with the CESM ocean biogeochemical component, the Biogeochemical Ecological Cycling (BEC) model.

Because of the size of the models and their complexities we will demonstrate that it is advantageous to geographically isolate a region of the combined model (CESM-BGC) for study. The Indian Ocean was chosen as the study region because of the challenge it provides for the net oxygen concentrations. It has two monsoonal seasons per year, making the surface currents extremely variable. It has two oxygen minimum zones of differing size and intensity.

Oxygen Minimum Zones Naturally forming zones in the open ocean where the oxygen levels are below that required to sustain life for many ocean organisms are known as Oxygen Minimum Zones (OMZs). These zones tend to form where the productivity at the surface is high, and the circulation is weak. It was Stramma et al. (2008) that alerted people to the dangers of the loss of oxygen from the ocean. Over the last 50 years, the volumes of the OMZs have been expanding, and it is predicted that they will continue to grow (Stramma et al., 2008; Deutsch, 2011; Bopp et al., 2002). Even more dire, it is the lowest levels of oxygen that are expected to expand the most (Bianchi et al., 2013; Bopp et al., 2013), and this has the greatest potential to affect the climate and the marine habitat.

Normal, saturated levels of oxygen at the surface are on the order of 200 mmol m^{-3}. In most areas of the ocean this decreases to a minimum below the photic zone, to a level on the order of 100 mmol m^{-3}, primarily due to biological respiration. Oxygen levels generally slowly increase again with depth, because of the advection and diffusion of colder, oxygen-rich waters and decreasing biological activity with depth. In the OMZs the oxygen minimum reaches extremely low concentrations, with a core that in some cases has oxygen levels below detection level; that is to say, anoxic. In OMZs the transition from the oxygen-saturated condition in the surface to the low-oxygen condition in the subsurface, the "oxycline", can be quite sharp: on the order of 10 to 20 m thickness. Another difference is the depth of the minimum: The normal minimum is at intermediate depths of 1000 to 1500 m; in an OMZ, the low oxygen levels may occur at depths as shallow as 50 or 100 m, and extend to thicknesses of a few hundred meters (Paulmier and Ruiz-Pino, 2009; Wyrtki, 1962). In the Indian Ocean a large and intense OMZ is present in the Arabian Sea (Altabet et al., 2012). A less intense OMZ is present in the Bay of Bengal.

The major impacts of expanded OMZs are: (1) the loss of habitat for the majority of biota that require high oxygen concentrations to survive; (2) the increased denitrification, which removes an essential nutrient from its bioavailable form, and produces N_2O, a powerful greenhouse gas; and (3) changes in the effectiveness of the biological pump for sequestering CO_2. We address each of these in turn.

Impacts: Loss of habitat Many biological processes have O_2 thresholds that limit the activity and habitat of marine biota. Concentrations of O_2 below 60 mmol m^{-3} are lethal for more than 50% of marine animals. This proportion increases to more than 90% when the oxygen concentration is below 10 mmol m^{-3} (Vaquer-Sunyer and Duarte, 2008). Keeling et al. (2010), illustrates the median lethal oxygen concentration for several major taxa, with crustacea being the most sensitive, but with a wide range within taxa. The medial value for crustacea is about 60 mmol m^{-3}, and for fishes and bivalva about 50 mmol m^{-3}. Gastropoda are less sensitive, with a medial lethal oxygen concentration of about 20 mmol m^{-3} (Gray et al., 2002; Keeling et al., 2010). Vaquer-Sunyer and Duarte (2008) found that crustacea, on average, had a slightly higher lethal O_2 threshold and a shorter lethal time of exposure than fishes, but the fishes showed stress symptoms at a higher O_2 threshold than the crustacea. At O_2 concentrations considerably higher than the threshold for mortality, in the range of 125 to 190 mmol m^{-3}, adult fish reduce food intake and growth (Gray et al., 2002). The potential expansion of the OMZs will have the greatest biological consequences from decreased oxygen levels, because the volume of water with O_2 concentration below the tolerance of many animals will increase. Further, the hypoxic effects depend not only on the O_2 concentration, but is interactive with other environmental factors, such as CO_2 levels and temperature (Keeling et al., 2010).

Impacts: Denitrification Denitrification, the biogenic production of N_2 gas from chemically combined forms of N, such as NO_3, occurs in the most intense part of the OMZs, where concentrations of oxygen of less than 5 mmol m^{-3} require microbial life to rely on oxidants other than O_2, and anaerobic processes become prevalent (Ward et al., 2009; Altabet et al., 2012). Denitrification reduces the availability of NO_3 as a nutrient, and may thus limit the sequestration of atmospheric CO_2 in the ocean indirectly because of a limitation of primary production due to the fixed nitrogen loss (Falkowski, 1997). As a byproduct of the denitrification process, N_2O, a potent greenhouse gas, is produced, affecting the climate directly (Bange et al., 2005). Denitrification accounts for half of the global fixed nitrogen removal from the ocean (Codispoti et al., 2001; Bange et al., 2005). The Arabian Sea OMZ is responsible for 30 to 50% of the global fixed nitrogen loss (Bulow et al., 2010), making the contribution of the Arabian Sea OMZ disproportionately large. In the Arabian Sea, when the O_2 concentration is higher than 2 mmol m^{-3}, denitrification rates are at their lowest, leading to the conclusion that oxygen levels below that limit are needed for significant denitrification to occur (Bulow et al., 2010). Denitrification is most intense in the central Arabian Sea (Bulow et al., 2010).

Impacts: the carbon pump The effects of expanding OMZs on the carbon pump are mixed. On the one hand, the same mechanisms that form the OMZ, intense remineralization and weak circulation, form a dissolved inorganic carbon (DIC) maximum co-located with the OMZ. Remineralization occurs mainly in the subsurface layer, resulting in the largest gradient in both O_2 and DIC concentrations. The surface DIC concentration starts relatively low at the surface, increases quickly with depth, and comes to a maximum at around 2500 m. For both the Arabian Sea and the Bay of Bengal, the average DIC concentration in subsurface depths 200 to 950 m is about 2250 mmol m^{-3}, compared with about 2100 mmol m^{-3} for the southern Indian Ocean, where O_2 concentrations are high, around 200 mmol m^{-3}. The existence of the high DIC values in the sub-surface waters explains why the OMZs can be a local source of CO_2. Any water upwelled from the subsurface of the OMZ will release CO_2 to the atmosphere. This short-circuiting lowers the effectiveness of the biological pump (Paulmier et al., 2011).

On the other hand, the aerobic remineralization in the subsurface layer also produces nitrate, phosphate, and silicate from the organic matter. These released nutrients may enhance the rate of primary production when the water is transported upwards into the photic zone (Paulmier et al., 2011). The thermocline and the oxycline have strong variability and seasonality; the oxycline is shallower, at about 60 m depth during the November to January period and deeper, about 120 m depth, during the April to May period. It can become even shallower, about 30 m depth, following storms. The variability makes the nutrients available for phytoplankton in the photic zone, enhancing potential productivity, and thereby the carbon pump (Ravichandran et al., 2012).

Further, bacterial consumption of detritus within the OMZ is retarded (Rogers, 2000; Levin et al., 2000; Gooday et al., 2000), resulting in a high proportion of particulate organic matter (POM) sinking through the depths of the OMZ during peaks in phytoplankton blooms. At the bottom of the OMZ, as the oxygen concentration increases, there is a peak in the biomass supported by the sinking detritus (Levin et al., 2000), and no detritus accumulation on the seafloor (Cowie et al., 2009). However, in places where the OMZ reaches the sediments, thick aggregates of phytoplankton detritus occur. This means that during the monsoonal blooming season, the deep OMZ layer allows large amounts of detritus to sink without being recycled at mid-depth (Gage et al., 2000). This enhances the carbon pump by lowering the depth at which the organic matter is consumed.

Challenge: Recognizing the controlling factors for oxygen concentrations There is a complex balance among the major factors affecting the net result on oxygen concentrations as the climate changes. Temperature-rise in the surface waters decreases the saturation level of oxygen, resulting in decreased oxygen content in the surface waters, which then may be transported into the interior of the ocean. An increase in export production, the organic material sinking below the photic zone, increases the amount of remineralization in subsurface waters, which results in additional oxygen being consumed as part of the process. A decrease in export production, on the other hand, results in less oxygen being consumed. A decrease in the ventilation rate due to predicted declines in ocean interior circulation rates increases the residence time of the waters in the interior of the ocean, allowing more time for additional remineralization to occur before the waters reach a given location (Matear and Hirst, 2003), leading to lower oxygen levels. The accompanying predicted increase in the stratification of the upper ocean inhibits the mixing of the oxygen produced in the photic zone to below the thermocline (Deutsch, 2011; Keeling and Garcia, 2002; Bopp et al., 2002), also leading to lower oxygen levels in the interior.

Challenge: Historical data dirth in the face of variability While there is data available on the current oxygen concentrations in the ocean, the lack of substantial long-term data, and strong decadal oscillations, such as the El Niño Southern Oscillation (ENSO) and the Pacific Decadal Oscillation (PDO), make attribution of observed global changes difficult (Mecking et al., 2008; Emerson et al., 2004; Keeling et al., 2010; Ito et al., 2010). Few long-term observations exist in hypoxic regions, and none in suboxic zones (Stramma et al., 2010). The longest record is from the Southern California current system, where oxygen declines of up to 2.1 mmol m^{-3} y^{-1} have been observed throughout the system during the period 1984 to 2006. The largest relative declines have occurred below the thermocline: an average of 21% at 300 m (Bograd et al., 2008).

Further background is needed to set the context for the research.

1.2 Indian Ocean OMZs Background

The Indian Ocean is unusual in a number of ways. The surface circulation has large-scale monsoonal shifts north of 5S. It is landlocked at the northern end, which excludes temperate oceanic influences. This configuration affects the spatial and seasonal distribution of primary production, and the flux of particulate organic matter (POM), which in turn affects the oxygen concentrations. It is in this context that two OMZs at intermediate depths have formed: a very intense, large one in the Arabian Sea, and a smaller, less intense one in the Bay of Bengal (Kamykowski and Zentara, 1990; Rogers, 2000). To set the physical and biological context for the our study, we discuss aspects of the Indian Ocean circulation: the geometry of the basin, the monsoonal effects at the surface and the interfaces with the other parts of the ocean. We take a look at some key aspects of the OMZs that have formed: the oxygen levels found, and the traits and behaviors of the biota in response to those levels. We summarizes some key findings of previous modeling studies related to oxygen in the Indian Ocean. And we provide background on the existing tools for the study, both the CESM ocean component and the BEC model.

1.2.1 Indian Ocean Circulation and Interfaces

Geometry of the seafloor of the Indian Ocean The topographical features of the seafloor include mid-ocean ridges, abyssal plains, and the Java deep-sea trench, extending to

7500 m deep. Because of large riverine sources of terrigenous sediment (the Indus River into the Arabian Sea, and the Ganges and Brahmaputra Rivers into the Bay of Bengal) there are vast continental rises and abyssal plains. The terrigenous sediments are several kilometers thick on the continental rises. The abyssal plain south of the Bay of Bengal is the flattest large area of the earth's surface (Tomczak and Godfrey, 2003). The plain results from a turbidity flow down the northern end of the Bay of Bengal, extending 3000 km into the deep sea.

The Indian Ocean is subdivided into a number of major basins by long sections of mid-ocean ridge. The abyssal depths are divided into smaller basins by local meridional ridges. Of particular interest for this study are the Ninety-East Ridge, aligned with the Bay of Bengal, and extending from about 30S to 10N; the Chagos-Laccadive Ridge, an extension of the India subcontinent; and the Mid-Indian Ridge in the southern part of the Indian Ocean. Also helping to isolate the Arabian Sea is the Mascarene Ridge at about 10S. There are several ridges at the southern end of the Indian Ocean that may inhibit or redirect abyssal flows from the Southern Ocean: the Southeast Indian Ridge, the Southwest Indian Ridge, and just south of Australia, Broken Ridge/Diamantina Fracture Zone. Note that the Madagascar Plateau extends southward from the Island to about 32S, making the Mozambique Channel more meridionally extensive than it would appear on the surface.

Monsoons The main surface circulation north of 15S is arranged differently at the height of each of two monsoons by winds that are in opposite directions during the monsoons. The surface circulation is well illustrated in Schott and McCreary (2001), which shows the major surface currents during the Northeast Monsoon contrasted with those during the Southwest Monsoon. Beal et al. (2003) notes that it is impossible to treat the circulation as representative of a long-term mean, because several major surface currents switch direction twice each year between monsoons. The flows in the western boundary, the Somali Current, and the Great Whirl (off the coast of Somalia in the Southwest Monsoon) are non-steady. The Great Whirl can shift in position by a few degrees within 10 days. The Somali Current fluctuates both rapidly in response to the winds, and more slowly due to monsoonal forcing. Monsoonal influence is substantial only in the mixed layer and western boundary currents.

During the Northeast Monsoon, December through February, the Northeast Trade Winds are reinforced by winter cooling of air over the Asian land surface, especially the Tibetan Plateau. The westward-flowing North Equatorial Current from 8N to the Equator is strongest in January through March, resulting in an anticyclonic gyre north of the equator. Wyrtki (1962) indicated that the effects do not reach deep into the water column, and very little upwelling occurs. However, more recent investigations have found that the cold and dry winds of the Northeast Monsoon, combined with Ekman pumping, cause subduction of high-salinity surface waters in the interior northern Arabian Sea (Morrison et al., 1999; Schott and McCreary, 2001). A widespread Arabian Sea salinity maximum develops just underneath the surface-mixed layer which is favorable for subduction, because downward Ekman pumping occurs in the region of buoyancy loss. Deeper down there are southward undercurrents, which carry subducted waters toward the upwelling regions of the next summer (Schott et al., 2002).

The Southwest Monsoon, June through August, is created by the warming Asian land surface drawing moist oceanic air over the land. North of the Equator, eastward surface currents strengthen the Equatorial Countercurrent to become the Southwest Monsoon Current (also known as the Summer Monsoon Current). This current continues from the south end of the Arabian Sea around the bottom of India, and into the Bay of Bengal, connecting the surface sources of the two basins. A strong westward-flowing South Equatorial Current around 5S becomes more pronounced (Burkill et al., 1993). Strong upwelling and deep mixing occurs off the Somali and Oman coasts, giving rise to large increases in primary production (Nair et al., 1989; Beal et al., 2003). The dynamic structures of the Somali Current and the Great

Whirl fill the Somali Basin. The Somali Current is estimated at 38 Sv at its maximum (Beal et al., 2003). The western boundary currents extend deeply, disturbing sediments to depths as great as 2500 m with high-velocity flows.

Because the upwelling occurs in the extended western boundary current, the nutrients upwelled are not fully utilized locally, but carried northward by the strong current. Both nutrients and planktonic biomass from the upwelling consequently enhance the biomass and secondary production in the central Arabian Sea. The zooplankton concentrations in the vicinity of the upwelling zone are not as high as comparable upwelling systems in the Pacific and the Atlantic (Tomczak and Godfrey, 2003).

The monsoon currents are not always found in the same location during a given season or during different years. For example, the Southeast Monsoon Current in the Bay of Bengal intensifies and shifts westwards as the Southwest Monsoon progresses (Shankar et al., 2002).

The South Equatorial Current, at about 15S, is the dividing line between the monsoon-driven Northern Indian Ocean and the sub-tropical anticyclonic gyre of the south. Southward from 15S, the behavior of the gyres is similar to counterparts in the South Atlantic and South Pacific.

There is little upwelling on the eastern boundary of the Indian Ocean because the supporting winds are weak during the Northeast Monsoon, and absent during the Southwest Monsoon. The small amount that does occur is along the coast of Java during the Southwest Monsoon. There is a weak upwelling off southwestern India (Wyrtki, 1962; Burkill et al., 1993). On the eastern boundary with Australia, the Leeuwin Current flows southward against the wind, and the undercurrent is northward, toward the Equator. With these circumstances, upwelling does not occur along the Western Australian shelf, which results in relatively low biological production in this region.

Interfaces with other seas Besides the Southern Ocean, there are three other seas with influence: the Persian Gulf, the Red Sea, and the Indonesian Throughflow (ITF). ITF waters enter the Indian Ocean mostly through Lombok Strait and Ombai Strait in the Indonesian Archipelago, and through the Timor Passage, just south of Java (Gordon et al., 2003). (In the CESM model, only the Timor Passage is open.) Characteristics of the ITF upper layers impact the heat and freshwaters fluxes of the South Equatorial Current in the Indian Ocean. Within the ITF, there are strong seasonal cycle impacts. There is a phase lag of between one and five months between the rainy season effects in the Indonesian seas, with a freshening of the surface layers, and the entrance of those waters into the Indian Ocean. This results in fresher surface and thermocline water in the southeast Indian Ocean from April through September. Along the ITF pathway, the ITF water profile changes due to strong tidal mixing that even modifies the thermocline layer as it enters the Indian Ocean (Atmadipoera et al., 2009).

In the Persian Gulf and Red Sea, evaporation exceeds precipitation, and warm, dense water enters the Indian Ocean, forming North Indian Ocean Intermediate Water (Tomczak and Godfrey, 2003). Both the Persian Gulf and the Red Sea have shallow sills connecting them with the Indian Ocean, inhibiting the transfer into the well-stratified upper ocean environment. There is a large density change between the source and product water, with entrainment or mixing with water that is less dense as it sinks to a neutral density. The source waters tend to flow down the continental slope at a steep angle, quickly entraining the overlying water and reaching neutral buoyancy about 30 km from the shelf-break (Bower et al., 2000). Equilibrium is reached at a depth of about 600 m for the Red Sea outflow, and about 250 m for the Persian Gulf outflow. There is an interchange, with water flowing in both directions through narrow openings. The Red Sea receives less dense water in a top layer, and the outflow is mostly through a denser bottom layer (Bower et al., 2000). Although the Red Sea has a strong seasonal cycle, due to mixing with the Gulf of Aden water, the resulting water is of about the same density in all seasons (Swift and Bower, 2003). (Note that in the CESM model, the Red Sea does not connect with the Indian Ocean.)

The Persian Gulf outflow toward the Arabian Sea is in the deep, southern side of the channel, with the inflow on the upper north side (Bower et al., 2000). The Persian Gulf is a source of oxygen-rich water, on a pycnocline that in the Indian Ocean is severely oxygen depleted. The Persian Gulf is shallow, with an average depth of about 35 m, with maximum depths of 110 to 160 m in channels leading through the Strait of Hormuz (Swift and Bower, 2003).

The annual mean transport is small, estimated as less than 0.4 Sv each for the Persian Gulf and Red Sea by Bower et al. (2000); Schott et al. (2002) estimate the outflow rate from the Persian Gulf is about 0.1 Sv, and the outflow from the Red Sea 0.3 Sv. Although Beal et al. (2003) indicates that the Arabian Sea has ventilation to depths of 1000 m north of 8N from Red Sea over-the-sill flows, chlorofluorocarbon (CFC) measurements taken near the density of the Red Sea water do not indicate any significant contribution from the Red Sea to the circulation within the Arabian Sea or the Bay of Bengal (Fine et al., 2008). However, on the basis of observed temperature and salinity characteristics, Bower et al. (2000) estimates that the Red Sea outflows are diluted by a factor of 2.5 and the Persian Gulf outflows by a factor of 4, as they travel from sill depth to neutral buoyancy.

South of 10S, between depths of 500 to 1000 m, there is a northward flow of Antarctic Intermediate Water (AAIW), blocked from further northward travel by the equatorial current system (Tomczak and Godfrey, 2003). Abyssal flow is associated with western boundary currents. Below 3500 m, cold Antarctic Bottom Water (AABW) prevails at 0.3°C. The main locations of entry into the Indian Ocean are below 3800 m through the Madagascar Basin, and through gaps in the Southwest Indian Ridge. The abyssal water forms a deep western boundary current, and travels along the western boundary in the Somali Basin, eventually entering the Arabian Basin, where it is gradually mixed in with deep water above it (Swallow and Pollard, 1988). In the eastern Indian Ocean, AABW enters into the South Australian

Basin, then moves westward, then northward, forming a western boundary current along the Ninety-East Ridge.

At 1500 to 3800 m, the Indian Deep Water is formed from North Atlantic Deep Water, carried in via the Antarctic Circumpolar Current. It spreads north in the western boundary current to the Arabian Sea and the Bay of Bengal. A combination of ridges to the south close off the Arabian Sea; bottom water enters from the west, through the Owen Fracture Zone, rather than directly from the south (Tomczak and Godfrey, 2003).

Fine et al. (2008) examined CFC data in the Indian Ocean. The CFC concentrations decreased going from south to north, with the lowest concentrations and oldest CFC ages, exceeding 40 years, being found in the Bay of Bengal intermediate waters. For thermocline water the average CFC age was 0 to 40 years, with intermediate water between 10 and 40 years. The most significant CFC source was the Southern Ocean, in particular AAIW. Bottom waters with CFC ages over 30 years are transported northwards into the subtropical southern Indian Ocean by three western boundary currents. At the time of the measurements (1996), the CFCs in the bottom water had reached 30S in the Perth Basin near Australia, and 20S in the Mascarene Basin, near Madagascar.

1.2.2 OMZs of the Indian Ocean

Oxygen-minimum layers are formed when there is both high productivity and poor water circulation (Rogers, 2000). Wyrtki (1962) first suggested that the biological degradation of organic matter sinking from the surface consumed oxygen, causing an oxygen-minimum at the depth with the slowest horizontal water circulation. Furthermore, Wyrtki (1962) hypothesized that oxygen concentrations increased below this depth because of decreasing biological oxygen demand. This theory has been modified by placing different importance on the relative contributions of productivity, circulation, and oxygen solubility of source water, but it remains substantially unchanged (Sarmiento and Herbert, 1988; Kamykowski and Zentara, 1990). In the OMZs, reduced oxygen concentrations generally occur between the near surface, and extend to a depth of 1500 m and occasionally deeper (Kamykowski and Zentara, 1990).

The first global study on OMZ geometry and denitrification was Kamykowski and Zentara (1990). Maps of hypoxic zones were produced, defined by a limit of < 8 mmol m^{-3}; and maps of denitrification, based on a nitrate deficit of > 10 mmol m^{-3}. In the Indian Ocean, OMZs were defined in the Arabian Sea and the Bay of Bengal.

Figure 1.1 shows the oxygen concentration at depths of 200 and 600 m; these are depths at which the OMZs are present. The data is replotted from the WOA13 gridded observational data. An intense OMZ can be seen in the Arabian Sea, and a less intense one in the Bay of Bengal.

There are some commonly used terms to describe key levels of oxygen in the ocean, and the transitions between relatively saturated and low oxygen conditions. "Suboxic" is defined as the O_2 concentration where a transition from oxygen to nitrate respiration occurs, with thresholds between 0.7 mmol m^{-3} (Yakushev and Neretin, 1997) and 20 mmol m^{-3} (Helly and Levin, 2004). (In this study, 5 mmol m^{-3} is used, as defined in Keeling et al. (2010)). "Anoxic" is defined as an O_2 concentration below the detection limit, or $O_2 < 0.1$ mmol m^{-3} (Oguz et al., 2000); it is characterized by the transition from nitrate-respiration to sulphate-reduction. Generally, with anoxic conditions, there is production of hydrogen sulfide (Dugdale, 1977) and methane (Cicerone and Oremland, 1988) episodically or where the OMZ is in contact with the sediments. "Hypoxia" refers to O_2 concentrations under which macro-organisms cannot live, and varies greatly by species: 8 mmol m^{-3} (Kamykowski and Zentara, 1990) up to 60 mmol m^{-3} (Gray et al., 2002), with some large fishes needing fully oxygen saturated waters (Davis, 1975).

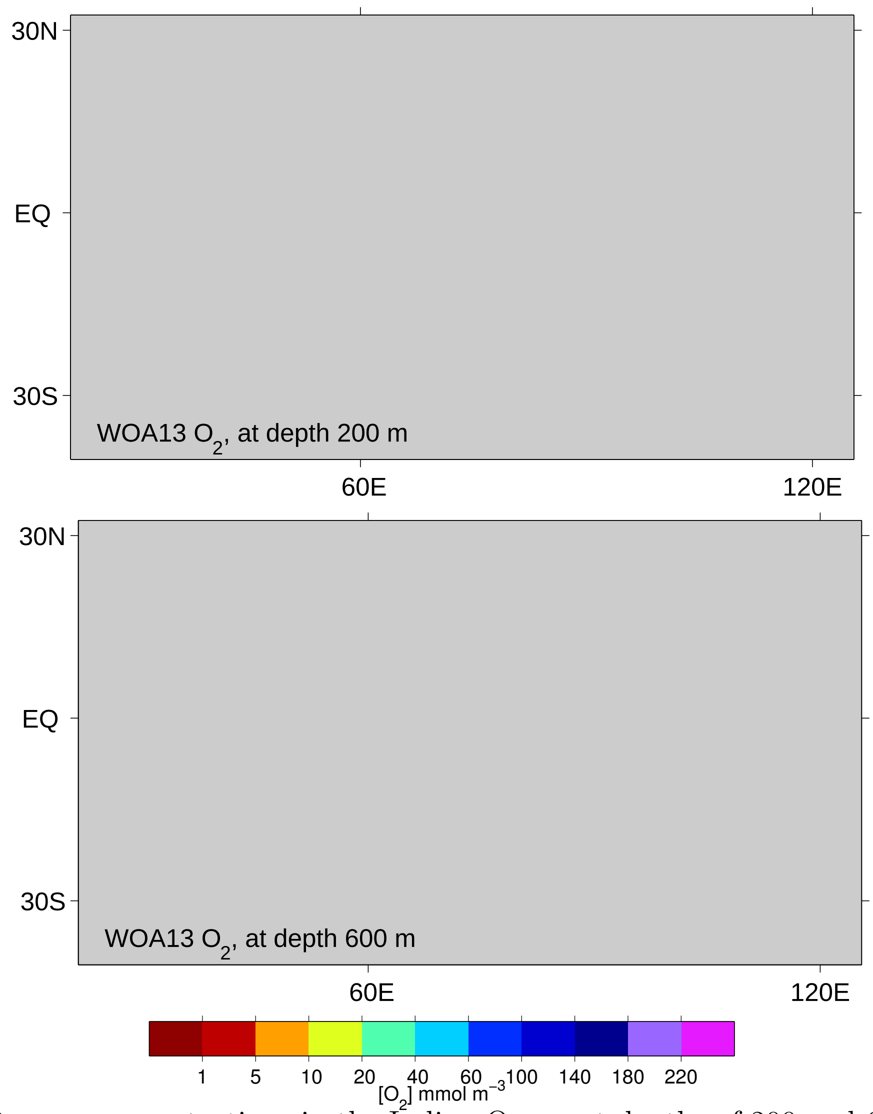

Figure 1.1: Oxygen concentrations in the Indian Ocean at depths of 200 and 600 m. Plotted from WOA13 gridded observational data.

Paulmier et al. (2006) notes that the existence of 3 different layers that need to be taken into account in an OMZ: the "oxycline", the upper O_2 gradient, where the O_2 concentration is rapidly decreasing; the "core", where the O_2 concentration is < 20 mmol m^{-3}; and the lower O_2 gradient, where the O_2 concentration is increasing with depth. The oxycline is the OMZ engine, where the most intense remineralization takes place, and has coupling with denitrification and nitrification when the O_2 concentration is < 20 mmol m^{-3} (Brandes et al., 2007). The O_2 core, with O_2 concentration of < 20 mmol m^{-3} is the maximum O_2 concentration for which denitrification has been observed (Keeling et al., 2010). An OMZ is said to be "more intense" when it has a lower O_2 concentration within its core (Paulmier and Ruiz-Pino, 2009).

Recent Argo float data gives us an idea of the variability of the oxycline. Prakash et al. (2012) analyzed Argo float O_2 data in the central Arabian Sea over a period of 3 years, and found strong inter-annual and intra-seasonal variability in the depth of the oxycline. The depth varied between 60 and 120 m, shoaling during the early Northeast Monsoon, with localized high wind events causing occasional further shoaling. In the surface layer, the O_2 concentration is saturated at > 180 mmol m^{-3}, but along the oxycline the O_2 concentration decreases rapidly to < 10 mmol m^{-3}.

The strong monsoonal seasonality is a major factor in production in the northern Indian Ocean. The monsoon forcing brings large-scale fertilization to the Arabian Sea through upwelling during the Southwest Monsoon and convective mixing during the Northeast Monsoon (Schott and McCreary, 2001).

The major observed phytoplankton bloom dynamics are located in the coastal upwelling regions and central Arabian Sea during the Southwest Monsoon, and during the Northeast Monsoon in the northern Arabian Sea as the mixed layer shallows (Anderson et al., 2007). Levels of bacterial abundance have been observed to be higher during the inter-monsoon periods (Ducklow et al., 2001; Ramaiah et al., 2005), suggesting lags between production of dissolved organic matter (DOM) and its consumption by bacteria (Anderson et al., 2007).

The local flux of particulate organic matter (POM) to the seabed is controlled by primary production in the photic zone above it, the depth of the water column, and in the Bay of Bengal the freshwater supply (Ittekkot et al., 2003). Along continental slopes with high primary productivity and a shallow water column, the flux of POM to the seabed is high on an annual average. Over the Oman Margin of the Arabian Sea, POM flux is strongly seasonal with peaks during the Southwest and Northeast Monsoons (Nair et al., 1989). High monsoonal primary production results from nutrient injection into the euphotic zone (Burkill et al., 1993). POM fluxes are greater during the Southwest Monsoon than during the Northeast Monsoon (Honjo et al., 1999). With no upwelling, the Spring inter-monsoon period is the most oligotrophic season. Within the sediments in contact with the OMZ, aggregates of phytoplankton detritus are thickest (up to 2 cm) in the Fall, at the end of the Southwest Monsoon. The deep OMZ layer allows large amounts of detrital material to sink without being recycled at mid-depth (Gage et al., 2000).

Cowie et al. (2009), in measuring the seasonal variation along the Pakistan margin, found little seasonal variation, except in the top 200 m. The oxycline began at 250 m inter-monsoonally, but rose to above 100 m in the late Southwest Monsoon period. The slope of the oxycline in the two periods was the same. Tapering back to higher O_2 concentrations began at 1200 to 1300 m.

Breuer et al. (2009) found that the bottom-water O_2 concentrations had little to no variation at depths spanning 300 m to 1850 m during expeditions to the Pakistan margin bracketing the Spring inter-monsoon season and the late Southwest Monsoon seasons. At 140 m, however, a large fluctuation between the inter-monsoon (with $[O_2] = 44$ mmol m^{-3}) and the post-monsoon (with $[O_2] = 1$ mmol m^{-3}) occurred, due to monsoonally-forced shoaling of the upper OMZ boundary. There was only a small penetration into the sediments at any measurement time or location, suggesting that the organic matter was largely remineralized during the monsoon period .

The source of most mesopelagic O_2 to the OMZs is thought to be from the south, but because the equatorial dynamics act as a barrier, the advection is concentrated along the western boundary, and during the Southwest Monsoon (Schott and McCreary, 2001). The combined effect creates southeast-northwest gradients in O_2 concentration (Bange et al., 2005). This is visible in Figure 1.1.

The Bay of Bengal was the subject of a set of Process Studies (BOBPS) following JGOFS, spanning 2001 to 2006, with cruises in every monsoonal season, measuring spatial and seasonal variations in physical, chemical, and biological properties, with many of the processes that result in the existing levels of oxygen investigated. The study found that the relatively low productivity was due to the strong stratification caused by the large amounts of fresh water received from the rivers (Ittekkot et al., 2003; PrasannaKumar et al., 2002). The associated suspended sediments result in a shallow euphotic zone in the northern Bay (Gomes et al., 2000). Sub-surface cold-core eddies support biological production by upward transport of nutrients across the strong stratification(Gomes et al., 2000). The existence of large bacterial abundances explains why the mesozooplankton biomass is decoupled with primary production(Franz et al., 2012). It may also help to explain the comparable POM flux with less primary production than that which takes place in the Arabian Sea(Madhupratap et al., 2003).

The Bay of Bengal, in addition to the variability of the monsoonal winds, has a large, highly seasonally varying source of freshwater (5 times as much as the Arabian Sea (Madhupratap et al., 2003)) and sediments (7 times as much as the Arabian Sea(Madhupratap et al., 2003)) from the rivers flowing in at the north end of the basin (Ittekkot et al., 2003). The freshwater reduces the salinity of the surface over much of the Bay to an annual average of < 34 psu, which reduces the interchange between the atmosphere, the surface, and the deep because of the increased vertical stratification (PrasannaKumar et al., 2002; Madhupratap et al., 2003).

During the Spring intermonsoon, the Bay has a surface mixed layer about 10 to 20 m thick, and below, a layer 50 to 70 m deep with steep salinity gradients. The strong stratification keeps the nutrients below 75 m. There is some upwelling along the western boundary, resulting in phytoplankton blooms. During the Southwest Monsoon, the peak in the flow from the rivers occurs, overwhelming the concurrent upwelling along the western boundary. The surface mixed layer deepens to 50 m, without significant mixing of the layers. Upwelling and river runoff increase the nutrient content of the surface waters all over the Bay. While there was a large increase in biomass, productivity was not that high; this is assumed to be due to light limitation because of intense cloud cover (PrasannaKumar et al., 2002).

During the Northeast Monsoon, primary productivity increases in the northern end of the Bay, from improved light conditions, and nutrient inputs from the river runoff. Surface temperatures decrease, but do not result in convective mixing due to the strong stratification. Productivity was about the same as during the Southwest Monsoon. Note that productivity in the Bay is less than half that of the Arabian Sea. This is largely attributed to the strong stratification (Madhupratap et al., 2003).

Although primary productivity was about the same in the Northeast and Southwest Monsoons, there is higher particle fluxes during the Southwest Monsoon in the northern Bay. This is thought to be due to the high inputs of terrigeneous material from the rivers. The lithogenic particles are incorporated with the biogenic material, which accelerates the sinking rates (Ittekkot et al., 2003).

Sarma et al. (2013) found that intensification of the OMZ was associated with an increase in vertical stratification and biological production during the Southwest Monsoon of 2010 along the northeast coast of India. This suggested that river-derived nutrients enhanced sinking POM, which lead to the intense OMZ in intermediate depths. A sharp decrease in O_2 concentration was found below the halocline at 30 to 50 m, and was close to the limit of detection at depths of 100 to 150 m. The upper boundary of the suboxic zone was between 70 and 115 m; the lower boundary was between 200 and 460 m. This intensity of OMZ had not been reported before in the coastal Bay of Bengal.

1.2.3 Fauna in the vicinity of the OMZs

The Arabian Sea OMZ has significantly lower species richness than has been found in other OMZs at similar O_2 concentration levels (Levin et al., 1997). The strong gradient in oxygen and organic matter concentrations at the upper and lower interfaces of the OMZs lead to a zonation of species distribution and is responsible for the peaks in abundance and diversity at the upper and lower boundaries (Rogers, 2000). A statistically significant biomass maximum has been observed at the transition to higher O_2 concentrations at the bottom of the OMZ, around 700 m (Levin et al., 2000).

Species diversity has been shown to generally decrease and dominance of a few species to increase within the cores of OMZs (e.g., Wishner et al. (1990); Gooday et al. (2000); Levin (2002)). Levin and Gage (1998), however, found that low oxygen in the Arabian Sea decreases the diversity of species, but that the higher the level of organic material, the greater the evenness in the abundance among the species that are present. Low oxygen eliminates some species from the OMZ domain, but the evenness of the species present is controlled by food availability. Benthic environments adjacent to OMZs have low species richness, and dominance of a few species is high (Levin et al., 1997).

The oxycline presents a significant boundary for the biota not adapted to low levels of oxygen. Acoustic measurements of an OMZ along the Peruvian coast revealed a consistent O_2 concentration limit for the biota on the oxycline. Repeated measurements of acoustic backscatter showed a clustering of bio-activity at an O_2 threshold of 36 mmol m^{-3}, regardless of time of day or night, and at any depth at which that O_2 level existed, between 10 and 60 m depth. This demonstrates that there is a fairly sharp boundary respected by the larger biota, such as anchovies. It also illustrates the importance of the vertical range of the OMZ. Organisms intolerant to low oxygen form densely above the oxycline, while the tolerant species have access to an extended refuge area (Bertrand et al., 2010).

Within the OMZ, adaptation to low O_2 concentrations is seen in altered morphology. The extent to which a species penetrates an OMZ is a measure of its adaptation to low concentrations of oxygen, as well as its ability to out-compete other species in such a stressed environment (Rogers, 2000). For example, cossurid polychaetes that live in low O_2 concentration regions have an enlarged respiratory surface area and more branched branchiae (Lamont and Gage, 2000). The most common species at 400 m depth have large numbers of long branchiae or tentacles (Levin et al., 1997). Foraminiferal taxa found in the OMZ are smaller in size, and have more elongated tests than those outside the OMZ (Gooday et al., 2000). Some organisms, such as polychaetes, have the ability to switch to anaerobic metabolic pathways (Rogers, 2000). On the other hand, the high DIC concentration in an OMZ results in a low pH, of about 7.5 (Paulmier and Ruiz-Pino, 2009), compared to an average ocean surface pH of 8.1 (Jacobson, 2005). The combination of low pH and low oxygen is not suitable for calcified taxa (Levin et al., 2000).

Because bacterial degradation and consumption of organic material are retarded within OMZs, there is an abundance of food for growth and reproduction for the species that can inhabit the OMZ (Rogers, 2000; Levin and Gage, 1998; Gooday et al., 2000). The very high quantities of organic matter available within an OMZ may have allowed species to evolve energetically expensive adaptations to cope with life in a low-oxygen environment (Rogers, 2000).

1.2.4 Model Studies Relevant to the Indian Ocean OMZs

Scientists do not understand on a quantitative basis all the factors that result in the OMZs in the Arabian Sea and the Bay of Bengal (Anderson et al., 2007). It is a challenging problem. It is impossible to treat the circulation as representative of a long-term mean, because several major surface currents switch direction twice each year between monsoons (Beal et al., 2003). The Somali Current fluctuates both rapidly in response to the winds, and more slowly due to monsoonal forcing. During the intense monsoon seasons, the dominant Ekman transport changes sign. There are heaving isopycnals thought to be from Rossby waves (Beal et al., 2003). The balance between the seasonally high production and an oxygen supply estimated to be 3-5 times greater than the biological sink, but resulting in a weak seasonality, is challenging to explain (Resplandy et al., 2012). The eastward shift from the area of high production in the western Arabian Sea that results in the OMZ core in the central Arabian Sea needs understanding (McCreary et al., 2013). The mechanisms that produce a weaker OMZ in the Bay of Bengal, compared with the very strong one in the Arabian Sea, have to be incorporated. Indeed, the Bopp et al. (2013) study of multiple models' predictions for the next 100 years cast doubt on the present models' ability to project changes in O_2 concentrations at the regional level, and particularly for low O_2 waters. Here we summarize some relevant model findings.

Deutsch (2011) Some of mechanisms analyzed in the Deutsch (2011) study of the causes of changes in O_2 concentrations in the Pacific also apply to the Indian Ocean. To examine the causes of lowered O_2 over the last 50 years, simulations of the oxygen cycle in an ocean general circulation model (OGCM) were analyzed. The proximate cause in the volume increase of suboxic water was found to be the rate of organic matter respiration in the surrounding low-oxygen waters. Physical transport of O_2 into the suboxic zones was found to be much less variable on decadal time scales than the respiration rate. However, changes in the respiration rate are in the long run caused by physical changes in the circulation and temperature of the water. The effect of warming on the solubility of O_2 in the surface ocean may cause expansion of low-oxygen water in the interior, but the sensitivity of the O_2 concentration below the surface to variations in the depth of the thermocline provides a mechanism for counteracting this expansion. If continued warming leads to a deeper thermocline in the tropics, this will diminish the O_2 demand in low oxygen thermocline water, and thus a contraction of suboxic conditions.

Stramma et al. (2012) A comparison of observations of O_2 concentrations over a 50 year historical period with modeled results was made by Stramma et al. (2012). The oxygen data was from HydroBase-2, augmented with recently collected data sets in the eastern Pacific. The model used was the University of Victoria (UVic) Earth System Climate Model, with 1.8° x 3.6° horizontal resolution and 19 depth levels. The marine ecosystem model with two phytoplankton classes, diazatrophs and others, and nutrients NO_3 and PO_4. The standard model configuration showed an increase in O_2 concentration in the 300 to 700 m depth range in the tropical oceans, compared to a decreasing trend in the observations. Neither increasing nor decreasing diapycnal mixing in the model reversed the tropical oceans' positive trend. Using a C:N ratio that increased with atmospheric CO_2 levels did not significantly change the result; however, this time span may have encompassed too small a range of CO_2 values to make a difference. Using CORE monthly winds which vary over a multi-year period instead of NCAR/NCEP climatological winds changed the results, but did not enable matching of the spacial patterns of the O_2 concentration decreases in the tropics and increases in the subtropics seen in the data. The global pattern of the change in oxygen concentrations could not be matched, in spite of varying the suspected controlling factors in the model circulation.

Resplandy et al. (2011) The study of Resplandy et al. (2011) was motivated by the findings of Kawamiya (2001) which showed that the lateral transport of nutrients into the central Arabian Sea was intensified when switching from a 1° to an eddy-permitting 1/3° resolution, and that the lateral transport was more important for nutrient supply than Ekman pumping. To study nutrient budgets in the Arabian Sea, Resplandy et al. (2011) used a 1/12° eddy-resolving biophysical model with 46 depth levels with increasing depth levels starting at 6 m for the surface layer, based on the Nucleus for European Modelling of the Ocean (NEMO) OGCM. The model covers the Northern Indian Ocean with an open boundary at 5S, which was constrained to monthly physical conditions from a previous global 1/4° simulation. The straits to the Red Sea, the Persian Gulf, and the ITF northeast of Sumatra are closed, with temperature and salinity damped with observational data. The biogeochemical model was based on the Pelagic Interaction Scheme for Carbon and Ecosystem Studies (PISCES), with two phytoplankton size classes (diatoms and nanophytoplankton), and two zooplankton size classes. The tracers phosphate and iron were removed because they are not major limiting nutrients in the Arabian Sea; this results in the diatom-class being limited by nitrogen and silicate, and the small-class being limited by nitrogen. The study found important mesoscale processes that result in increased nutrient supply to the upper layers during the Southwest and Northeast Monsoons, supporting high rates of productivity in the surface above the central Arabian Sea OMZ. During the Southwest Monsoon the main process supplying nutrients is mesoscale filaments transporting them from the coastal upwelling regions to the central Arabian Sea. Lateral advection accounts for 50 to 70% of the supply. Further, during the early Southwest Monsoon period, 60 to 90% of the nutrients were supplied to the upwelling regions by eddy-induced vertical advection. During the Northeast Monsoon, they found that vertical velocities associated with mesoscale structures increased the supply to the upper layers by 40 to 50%.

Resplandy et al. (2012) The same model and constraints that were used in Resplandy et al. (2011) were used by Resplandy et al. (2012) to study the current conditions and mechanisms supporting the Arabian Sea OMZ. They found that while the decrease in O_2 is most intense below the region of highest production in the western Arabian Sea, this is counterbalanced by the the O_2 supplied by the western boundary current. The seasonality changes make the dynamic transport of O_2 3 to 5 times greater than the biological sink, resulting in a weak seasonality in the OMZ. The main seasonal change in the OMZ is a vertical displacement, resulting from the monsoonal reversal of Ekman pumping across the basin. On annual time-scales they found that the biological sink is counterbalanced by the oxygen supplied via eddies and filaments.

McCreary et al. (2013) To determine the effects of various parameterizations on the OMZs of the Indian Ocean McCreary et al. (2013) used a biophysical model, with 6.5 water mass layers, and $1/2°$ horizontal resolution. Water sources included the Persian Gulf, the Red Sea, and the ITF, but rivers were represented by a freshening of the salinity only. The primary source for oxygenated water into the OMZ in the model was found to be from the south, along isopycnals. They found that subsurface remineralization is balanced primarily by the spreading of well oxygenated water from the south. The eastward shift in the Arabian Sea OMZ location is caused mostly by northward advection along the Somali and Omani coasts, carrying upwelled nutrients and small detritus, which is also subject to the eastward advection. It is also affected by vertical eddy mixing and inflow from the Persian Gulf. One reason the Bay of Bengal OMZ is not as intense as that in the Arabian Sea is that it lacks a similar western boundary source of detritus. The wind forcing is weaker in the Bay, and there is not a strong western-boundary upwelling.

McCreary et al. (2013) found it necessary to maintain two size classes of detritus with different remineralization and sinking rates, with the smaller class sinking very slowly or not at all, in order to maintain an efficient microbial-remineralization loop that retains fixed nitrogen in the upper ocean. The large detritus exports some nitrogen to the deep ocean, and decreases O_2 in subsurface layers. A small sinking rate was necessary for the Arabian Sea OMZ to achieve suboxic levels while not in the Bay of Bengal. McCreary et al. (2013) notes that a 3-D biophysical model using a Martin curve for remineralization of detritus eliminates the impact of other than 1-D processes on detrital distributions, and will therefore make it unable to simulate the eastward shift of the Arabian Sea OMZ.

Although the primary productivity has an extremely high seasonal variability, the size of the OMZs does not vary much with the season. The most likely explanation is that the oxygen variation caused by the seasonally varying detrital flux is weak. The amount of detritus that can be remineralized in one season is much less than what is available. This is in agreement with Resplandy et al. (2012).

Bopp et al. (2013) An analysis of the CMIP5 model results focusing on the ocean was made by Bopp et al. (2013). Ten earth system models project similar global oxygen trends for each of the Intergovernmental Panel on Climate Change's (IPCC's) representative concentration pathways (RCPs). For the "business-as-usual" RCP8.5, the change from 1990 to 2090 in the global ocean O_2 concentration is -3.4%; for the high mitigation scenario, -1.8%. The largest projected changes in O_2 concentrations are in intermediate and mode waters. The projected changes in O_2 concentration are not robust across models (that is, not even of the same sign for 80% of the models), particularly in the tropics, the areas of the OMZs. The Indian Ocean was projected as having slightly higher O_2 concentrations in the 200 to 600 m depth range, except in the northern Arabian Sea, where a loss is expected. This projection is coupled with a potentially significant decrease in net primary production along the Arabian Peninsula and Somali coast.

Present day oxygen concentrations at 200 to 600 m were compared among the models, as well as a 3-D oxygen field. Comparison with WOA09 observational data showed reasonable agreement for the 200 to 600 m waters, but was substantially off across models in the 3-D spatial variation. In the Indian Ocean OMZs, for the 200 to 600 m present day, the models tended to be too high compared with observations, missing the intensity of those OMZs. Model estimates of the global volume of O_2 with a concentration of < 5 mmol m^{-3} varied from 0.4 x 10^{15} to 50 x 10^{15} m^3, compared to observations of 2.4 x 10^{15} m^3. The CESM1-BGC model estimate was 16.4 x 10^{15} m^3.

1.3 The CMIP5 CESM1-BGC model

To examine the balance between the oxygen sources to the OMZs, and the biological sinks, the BEC production and remineralization output variables were used to drive the Indian Ocean regional oxygen model. CESM1-BGC designates an atmosphere-ocean fully coupled model including a carbon cycle. The BEC model executes in conjunction with the ocean component of CESM, and provides the biogeochemical aspect. It includes multiple phytoplankton functional groups (diatoms, diazotrophs, and smaller phytoplankton), zooplankton, and key nutrients and environmental variables by cycling key elements (C, N, P, Fe, Si, and O). It includes a full set of carbonate chemistry dynamics to support organic carbon chemistry and CO_2 and O_2 air-sea flux. Primary production is dependent on light, nutrients, and temperature in a multiplicative fashion.

The BEC production paradigm (Moore et al., 2013) provides for 3 classes of production pathways: 1) labile DOM, which is instantly remineralized to inorganic form where it is produced and is subjected to direct remineralization from grazers; 2) semi-labile DOM, which includes any organic material (OM) that does not sink, but travels with the circulation; and 3) POM, which sinks and is instantly remineralized in a 1-D water column, with a Martin-curve like approach, but with varying length scales. The sinking POM in the BEC is treated as having been produced, and as sinking from each layer where it is produced within the photic zone.

The BEC model outputs used in this study were from a 20th-century ocean-atmosphere coupled run designed to meet the requirements of phase 5 of the Coupled Model Intercomparison Project (CMIP5). Moore et al. (2013) documents the BEC version used for this simulation. To spin up the BEC tracers, the CESM ocean model was cycled for several thousand years before starting the prognostic simulation covering the period 1850 to 2005 (Moore et al., 2013). The 1990's averaged monthly values were extracted for this analysis.

Figure 1.2 shows the annually-averaged oxygen concentrations at depths of 200 and 400 m for the Indian Ocean as produced by the BEC CMIP5 run. These can be compared with the observational values shown in Figure 1.1 for the same depths. At a depth of 200 m, the extremely intense OMZ in the Bay of Bengal, extending south of the Equator is striking. The oxygen concentration reaches < 1 mmol m^{-3} on the eastern side of the basin below the Equator. The Arabian Sea shows higher oxygen concentrations than the observations. At a depth of 600 m, there are intense OMZs covering most of the Arabian Sea and the Bay of Bengal. The core of the OMZs ($[O_2] < 20$ mmol m^{-3}) extends well below the equator.

The BEC categorizes the sinking POM as that which has a mineral ballast, such as calcium carbonate, and that which does not; this affects the length scales of the remineralization vs. depth curve. Moore et al. (2013) critiques the remineralization curve used for POM that does not have a mineral ballast as resulting in excessive remineralization at around 500 m, and too small a flux deeper in the water column. This could contribute to the excessive consumption of oxygen in the mid-depths. It does not, however explain the shift in the locations of the OMZs.

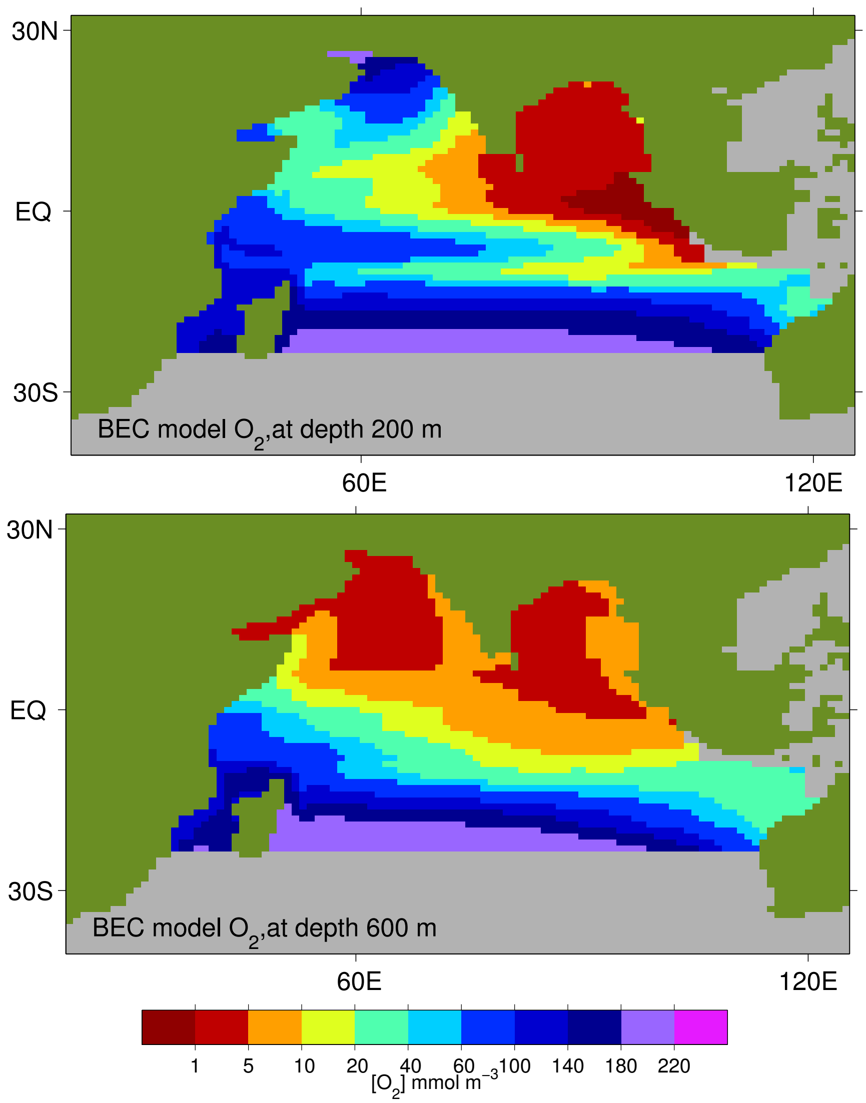

Figure 1.2: The $[O_2]$ in the layers at 200 m and 600 m, as produced by the BEC CMIP5 run.

1.4 The offline CESM model

Chapter 2 documents the development of the offline tracer transport operator, representing tracer advection and diffusion in the global ocean, based on the CESM ocean component. The prognostic CESM ocean model is referred to as the" parent model" of the offline version. The configuration has a computational mesh of nominally 1° in the horizontal, with 60 grid levels in the vertical direction with resolution ranging from 10 m in the top 10 layers of the model to 250 m near the bottom. The thickness of the top-most layer is allowed to vary to include regional and temporal variations in sea surface height (Smith et al., 2010). A normal climatological year forcing was used; the extremes of the El Niño Southern Oscillation (ENSO) or the Indian Ocean Dipole (IOD) are not present.

Recently incorporated changes in the CESM ocean component (Danabasoglu et al., 2012) include a sill overflow parameterization (Briegleb et al., 2010; Danabasoglu et al., 2010), providing non-local transport by unresolved density currents over a few key sills where deep waters are formed in the North Atlantic and the Southern Ocean. Also recently incorporated are a near-surface eddy flux parameterization (Danabasoglu et al., 2008), a prescription for lateral tracer diffusivities that vary in the vertical (Danabasoglu and Marshall, 2007), a sub-mesoscale mixed layer eddy parameterization (Fox-Kemper et al., 2011), a parameterization for abyssal tidal mixing (Jayne, 2009), and a new method for determining background vertical diffusivities (Jochum, 2009). The transport of tracers in the model is achieved by a combination of explicitly resolved currents and by parameterized sub-gridscale transport processes, which include spatially-varying isopycnal and diapycnal diffusion, eddy-induced advective currents, and non-local transport over sills where deep waters are formed.

There were some differences in the circulation spin-up between the CESM parent model, and that used for the CMIP5 BEC simulation. The CESM parent ocean model had been spun-up from rest using the Common Ocean-ice Reference Experiments (CORE) climatological seasonally cycling forcing for 150 years before the one-year run from which the circulation fields were taken. We think the circulation differences are small to first order.

The offline tracer-transport model and the preconditioner are based on monthly and annually averaged tracer-transport matrices, which are constructed using output from the CESM ocean model simulation. Details of the construction of the offline model from the parent are given in Chapter 2.

1.5 Research

We need to use every tool at our disposal to assess the fidelity of the models, to diagnose the causes of biases, and to understand the mechanisms that produce them. While we have no way to test against observations of the future, we can evaluate the models against current observational data.

There are very few tools for analysis of the deep ocean circulation. It is particularly problematic because of the long time-frames involved in the global ocean circulation in the deep, which is on the order of several thousand years. One of the best assessment methods is to use natural ^{14}C as a tracer, since there is a reasonable amount of data available, the half-life is 5730 years, and the $^{14}C/^{12}C$ ratio in the atmosphere has been reasonably constant over the Holocene.

The ocean physics is non-linear. The forces at play are affected by the changing density with temperature, the interaction with salinity, and the possible hysteresis effects from long time-scale processes. As a result, the solution for the advection and diffusion is not computed directly in prognostic OGCMs, but by time-stepping, evaluating the conditions and flow fields in small time-steps. Time-stepping also allows examination of the time-dependent dynamics. The tracer transport depends on the advection and diffusion, and as such the standard approach is to time-step the tracer until some level of quasi-equilibrium or cyclic-equilibrium is reached. The problem with any tracer in the deep ocean is that the long deep ocean time scales result in excessively long spin-up times for the tracer, following the spin-up of the physical circulation. The long clock-time for tracer spin-up has lead to deep ocean tracers such as natural ^{14}C being infrequently used on models of the IPCC class. And, as the ocean models become more highly spatially resolved, the clock-time gets even longer for two reasons: the time-step has to be shortened to accommodate the smaller grid-cell size, and there are more grid-cells to process.

There is a method to dramatically decrease the tracer spin-up time, making the assessment of the deep ocean circulation feasible. A fast offline implicit solver for simulating natural ^{14}C has been developed based on the CESM ocean component. The development of the offline implicit solver, and its application to ^{14}C is the subject of Chapter 2 of the dissertation. For the parent model, with a nominal horizontal resolution of 1°x 1°and 60 depth levels, the reported ^{14}C spin-up model-time to reach OCMIP-2 equilibrium criteria exceeded 4000 years (Orr, 2002). Using a Newton-Krylov algorithm and an effective preconditioner, the equilibrium results were obtained in 23 years.

The ^{14}C model results compared with observations, while excellent in the North Atlantic, showed significant bias in the deep circulation, in particular being too sluggish in the Pacific Ocean, and to a lesser extent in the Indian Ocean. The ^{14}C age in the deep Pacific in the model was twice what was shown in the observations. The ^{14}C model results provided enlightenment on the O_2 results being seen from running simulations with the BEC. The amount of remineralization was too high, resulting in net oxygen depletion. Remineralization is the conversion of organic matter back into non-organic forms by bacteria, with oxygen taken up in the process. The water taking longer to circulate allows more time for remineralization, and thus for a given deep water location, results in lower oxygen values.

The offline model platform and the solution techniques enabled the further investigation of behavior of the ocean mode in Chapter 3. Ideal ventilation age, the time since the water parcel last at the surface, was calculated, using the steady-state transport operator. Ideal age differs from ^{14}C, and many other physical tracers, in that there is no air-sea flux, eliminating that source of variation from age, and the aging is linear with time, independent of the current age. The ideal age confirmed the picture of the ocean circulation given by natural ^{14}C.

Both ^{14}C and ideal age at any given deep water location depend on where the water was last ventilated. Further insight was gained by determining how the waters that were last at the surface in a given region of the ocean were distributed in the interior ocean. Ventilation fraction analysis provides insight into the water movement and the tracers the water is bringing with it. The ventilation fraction analysis showed that the North Atlantic was the major supplier of ventilated water to not only the Atlantic, but also the Pacific and Indian Oceans. It also showed that in the Southern Ocean, there was little formation of bottom water from its own surface.

To see the effect of combining the water mass fraction and the water age information, the age for each fraction ventilated from the most significant sources, the North Atlantic and the Southern Ocean, was determined. This confirmed that the excessive aging was mostly occurring in the Pacific, and was not specific to any ventilation-source waters. Additionally, the Southern Ocean surface ventilation fraction aged excessively going to the bottom of the water column. This, together with the small fraction of Southern Ocean ventilated water resident at the bottom, leads to the inference that there is a lack of Antarctic Bottom Water being formed in the model.

Outside of the North Atlantic, the deep circulation provides an extensively biased circulation environment in which to model the oceanic biogeochemistry. Many aspects of the biogeochemistry are dependent on the tracer transport provided in the circulation. The symptoms seen in the oxygen results of running the BEC in conjunction with the CESM ocean component become more understandable given the bias in the circulation. One of the most conspicuous symptoms is the low oxygen values in the Pacific and Indian Oceans.

Isolating a region of the ocean using the technique given in Chapter 4 provides a method to diagnose whether the circulation and biogeochemical biases were local to the region or came from outside of it. If the external biases are removed from the region, then it may be possible to begin to understand the remaining local biases.

The Indian Ocean region was isolated with a newly developed technique that retains the effectiveness of the advection and diffusion fields on the boundary. ^{14}C was used as a tracer to determine the global versus regional circulation biases, without a biological component; most of the bias was eliminated. Oxygen concentrations were calculated using BEC oxygen production and consumption variables from the CMIP5 simulation. There were three cases resulting: the global CMIP5 simulation; the offline regional model simulation with oxygen values from the CMIP5 run on the oceanic boundaries; and the offline regional model with oxygen observational models on the boundaries. The ocean circulation spin-up and the forcings were sufficiently different in the CMIP5 simulation than in the parent for the offline model, that the resulting oxygen concentrations differed in each case. The closest match to oxygen observational values was in the regional model with observations on the boundary; however, the remaining bias in the location of the OMZs and lack of intensity calls out for further research.

As Albert Einstein said:

> "If we knew what we were doing, it would not be called research, would it?"

Chapter 2

An Offline Implicit Solver for Simulating Prebomb Radiocarbon

2.1 Abstract

It takes several thousand years for the deep-ocean concentration of natural radiocarbon to come to equilibrium with surface fluxes, making it computationally too expensive to routinely simulate it with moderate- to high-resolution ocean models. We present an implicit solver for computing prebomb $\Delta^{14}C$ that requires the equivalent of only a few tens of model years to reach equilibrium. The solver uses a Newton-Krylov algorithm with a preconditioner based on a coarse-grained annually-averaged tracer-transport operator. Coarse-graining provides a general approach for developing preconditioners for models of increasing resolution. We implemented and tested the solver for the ocean component of the Community Earth System Model (CESM) with a nominal horizontal resolution of $1° \times 1°$ and with 60 vertical levels. Simulated $\Delta^{14}C$ values are in good agreement with

observations at the surface and in the North Atlantic, but the deep North Pacific simulated values show a substantial bias, with prebomb radiocarbon $\Delta^{14}C$ values translating to ages that are twice the observationally based estimate. This bias is substantially larger than published simulations obtained with coarser resolution models, suggesting that increasing model resolution does not automatically improve the fidelity of the deep ocean ventilation processes. We therefore recommend that natural $\Delta^{14}C$ be used as a deep-ocean ventilation metric for critically evaluating deep ocean circulation.

2.2 Introduction

Assessing the fidelity of the ocean circulation in climate models is an important model development step. Models which are used to study climate trends and the evolution of the ocean's CO_2 uptake in a warming world need to be adequately tested before their results are used to influence science and national policy. Because the ocean interacts with the rest of the Earth system over a wide range of spatial and temporal scales there is no unique metric by which to judge the quality of the simulated circulation, but at long timescales the role of the deep ocean becomes increasingly important because of its capacity to store vast amounts of heat and carbon. To assess the rate at which the deep ocean communicates with the surface ocean and the atmosphere, ocean modelers have long recognized the utility of simulating natural radiocarbon (see for example the references listed in Tables 1, 2 and 3). The availability of globally-gridded natural radiocarbon observations, (GLODAP, Key et al., 2004), has made radiocarbon simulations especially useful for identifying biases in the ventilation of the deep ocean.

For example, Doney et al. (2004) evaluated and contrasted radiocarbon simulations done using 13 different models as part of the Ocean Carbon Model

Intercomparison Project Phase 2 (OCMIP-2) and found that errors in the simulated radiocarbon could be attributed to biases in the circulation, and that a significant part of the differences among the models could be tied to differences in sub-gridscale parameterizations. Duffy et al. (1997) and England and Rahmstorf (1999) used $\Delta^{14}C$ simulations to evaluate the effect of the Gent-McWilliams (GM) parameterization on the ventilation of the deep ocean, and found that it tended to limit the depth of convection at high latitudes. Further confirming this result, Gruber et al. (2001) found using $\Delta^{14}C$ tracer simulations, that the GM parameterization tended to give a sluggish deep circulation in their model. They showed that a 6-fold increase in the vertical diffusivity south of 50°S was needed to reduce excessive stratification and thereby improve the ventilation of the deep Pacific. Gnanadesikan et al. (2004) used $\Delta^{14}C$ simulations to evaluate the sensitivity of variations in the vertical and horizontal diffusivities in the Modular Ocean Model version 3 (MOM3). They found that both lateral and vertical mixing processes can affect the resulting $\Delta^{14}C$ distribution, but also that changes in the surface forcing can have a major impact. Butzin et al. (2005) found a strong influence of Antarctic sea ice formation on the circulation, based on $\Delta^{14}C$ simulations.

Despite its utility, radiocarbon simulations are not routinely done by climate model developers. Simulating natural radiocarbon is a considerable computational challenge because of the long timescales with which deep ocean radiocarbon equilibrates with the atmosphere – some models that participated in the OCMIP-2 study reported tracer equilibration times for radiocarbon of more than 4000 years (Orr, 2002). Furthermore, the computational challenge increases dramatically with increasing resolution because of Courant-Fredrichs-Lewy (CFL) stability criterion restrictions on the model time-step size. As far as we know, none of the ocean components in the current suite of IPCC-class climate models with a resolution of $1^\circ \times 1^\circ$ or higher have simulated natural radiocarbon to help calibrate the deep-ocean ventilation rate in their models.

Here we present a fast offline implicit solver for simulating natural radiocarbon in the ocean component of the Community Earth System Model (CESM). Our solver uses a Newton Krylov method and preconditioning strategy that are similar to the ones first suggested by Li and Primeau (2008) for biogeochemical tracers, but adapted for the increased memory requirements associated with the higher resolution of the CESM ocean model component, i.e. the Parallel Ocean Program version 2 (POP2), with a nominal $1^\circ \times 1^\circ$ horizontal resolution and 60 vertical levels (Smith et al., 2010). The cyclo-stationary Newton-Raphson solver and the preconditioner for the iterative Krylov-subspace linear-system solver are described in Section 2.7. The offline tracer-transport model and the preconditioner are based on monthly and annually averaged tracer-transport matrices, which are constructed (see Section 2.5), using output from a POP2 simulation, which we refer to as the parent model (Section 2.4). Using the new implicit solver we are able to compute the natural prebomb-Δ^{14}C equilibrium distribution by running the offline model through only 23 annual periods (Section 2.8.1). The formulation of the natural radiocarbon model is presented in Section 2.3 and the time integration scheme used by the offline model to simulate a seasonal cycle is presented in Section 2.6. Section 2.8.2 discusses the impact of neglecting the seasonal variations in ocean circulation on the simulated Δ^{14}C distribution.

We compare our Δ^{14}C simulations to the GLODAP observationally based estimates in Section 2.8.3, providing insight into the behavior and biases of the parent model. We also compare our results to previous radiocarbon modeling studies in Section 2.9 before presenting our conclusions in Section 4.8.

2.3 Governing Equations for $\Delta^{14}C$

Following Toggweiler et al. (1989a) we formulate our prebomb radiocarbon model in terms of the ratio $R = {}^{14}C/{}^{12}C$ expressed in arbitrary units in which the prebomb atmosphere is set to $R_{atm} = 1$,

$$\frac{\partial R}{\partial t} + \nabla \cdot (\mathbf{u}R - \mathbf{K} \cdot \nabla R) = S_{14}(R), \tag{2.1}$$

where $\mathbf{u}$ is the fluid velocity vector, $\mathbf{K}$ is the eddy-diffusivity tensor, and

$$S_{14}(R) = -\lambda R + \begin{cases} \mu(R_{atm} - R) \text{ if } z > -\Delta z_1, \\ \qquad 0 \text{ otherwise,} \end{cases} \tag{2.2}$$

is the radiocarbon source-sink function including both radioactive decay with rate constant $\lambda = (8266.6 \text{ years})^{-1}$ and air-sea fluxes parameterized as a source in the top layer of the model. In the air-sea flux parameterization $\mu = (2 \text{ years})^{-1}$ and $\Delta z_1 = 10$ m. This simplified model for the air-sea exchange of radiocarbon corresponds to the one used in Experiment A of the study by Toggweiler et al. (1989b). It neglects any spatial inhomogeneities in the air-sea flux of radiocarbon due to variations in the air-sea flux of CO_2. See Section 2.8.3 for further discussion on the adequacy of this simplified parameterization.

After having been discretized, the governing equations can be expressed as a system of ordinary differential equations in matrix form as follows:

$$\frac{dR}{dt} = \mathbf{M}R + \boldsymbol{\mu}R_{atm}, \tag{2.3}$$

in which $\mathbf{M}$ is a time dependent matrix defined as

$$\mathbf{M}(t) \equiv [\mathbf{T}(t) - \lambda\mathbf{I} - \boldsymbol{\mu}], \tag{2.4}$$

where $\mathbf{T}(t)$ is the advection-diffusion tracer transport operator expressed in matrix form and $\boldsymbol{\mu}$ is a diagonal matrix whose elements are equal to μ for grid-cells in the surface layer of the model and 0 otherwise. Note that the air-sea exchange term has been split into the term $\boldsymbol{\mu}R$, which is incorporated into the $\mathbf{M}$ term, and the constant term $\boldsymbol{\mu}R_{atm}$.

The arbitrary units of R can be converted to the standard Δ^{14}C notation as follows:

$$\Delta^{14}\mathrm{C} = (R - 1) \times 1000, \tag{2.5}$$

and R can also be converted to a radiocarbon age as follows:

$$\text{C14-age} = -\frac{\ln R}{\lambda}. \tag{2.6}$$

With a half-life of 5730 years and a relatively constant $^{14}\mathrm{C}/^{12}\mathrm{C}$ ratio during the Holocene, natural radiocarbon expressed as Δ^{14}C is a useful tracer for quantifying the ventilation of the deep ocean.

2.4 Parent Ocean Model: CESM POP2

The "parent" ocean model from which we constructed the seasonally varying tracer-transport operator is based on a prognostic simulation of the ocean component, POP2, of the Community Earth System Model (CESM) (Smith et al., 2010). The POP2 configuration we used has a dipolar grid with the North Pole displaced into Greenland, with the transition from the Mercator grid starting at the Equator (Smith et al., 2010). The computational mesh has $N_x = 320$ and $N_y = 384$ grid points in the nominally eastward and northward directions and $N_z = 60$ grid points in the vertical direction, for a total of 4,241,988 wet grid points. The vertical resolution ranges from 10 m for the top 10 layers of the model and increases to 250 m near the bottom. The thickness of the top-most layer is allowed to vary to include regional and temporal variations in sea surface height.

The dynamical model was "spun-up" from rest for 150 years using the CORE climatological forcing (Griffies et al., 2009; Large and Yeager, 2009), in which the same seasonal cycle is repeated every model year. The relatively short dynamical spin-up, of only 150 years, was chosen as a compromise between the availability of computational resources and the time needed for the transients in the momentum equations to decay. Although the model is still drifting after 150 years, the relative change in the magnitude of the major currents has decreased substantially and is typically less than 0.1% per year at the end of the spin-up.

After the spin-up, the dynamical ocean model was run for an additional year during which we saved all quantities (see Sec.2.5) needed to construct the model's advection-diffusion transport operator in matrix form with a monthly time resolution. This procedure allows us to capture the seasonal cycle, which accounts for the largest part of the transport variability in the ocean. We are thus assuming that interannual variability has a second order effect on the transport of tracers in the ocean, but the error associated with this assumption remains to be quantified. Although we used only one year of the OGCM circulation to capture the transport operator, it is feasible to use an average over several years; this would average out some of the interannual variability. We hope to explore this possibility in the future.

The transport of radiocarbon and other tracers in the model is achieved by a combination of explicitly resolved currents and by a suite of parameterized subgridscale transport processes, which include spatially-varying isopycnal and diapycnal diffusion, eddy-induced advective currents, and non-local transport by unresolved density currents over a few key sills where deep waters are formed. Recently incorporated changes in POP2 (Danabasoglu et al., 2012) include a sill overflow parameterization (Briegleb et al., 2010; Danabasoglu et al., 2010), a near-surface eddy flux parameterization (Danabasoglu et al., 2008), a prescription for lateral tracer diffusivities that vary in the vertical (Danabasoglu and Marshall, 2007), a sub-mesoscale mixed layer eddy parameterization (Fox-Kemper et al., 2011), incorporation of a parameterization for abyssal tidal mixing (Jayne, 2009), and a new method for determining background vertical diffusivities (Jochum, 2009).

The model uses the Gent and McWilliams (GM) (Gent and McWilliams, 1990) isopycnal transport parameterization in its skew-flux form with a diffusion tensor that is rotated to allow for different along- and across-isopycnal diffusivity coefficients. The diffusivity has a vertical dependence that varies with the stratification, which can lead to large values in the upper ocean, but much smaller values in the deep (Danabasoglu and Marshall, 2007). The effects of diabatic mesoscale fluxes within the surface are taken into account based on the near-boundary eddy flux parameterization of Ferrari et al. (2008) as implemented in Danabasoglu et al. (2008). High isopycnal diffusivity values, here as large as 3000 m^2 s^{-1}, in the upper ocean represent the effects of the vertical divergence of eddy stress (Danabasoglu and Marshall, 2007). The values are diminished to 300 m^2 s^{-1} by a depth of 2000 m. Isopycnal diffusivity coefficients are tapered for isopycnal slopes greater than 0.3 in the interior ocean. The thickness and isopycnal diffusivity coefficients vary together vertically (Danabasoglu et al., 2012).

Vertical diffusivities are determined dynamically using the K-profile parameterization (KPP) (Jochum, 2009; Danabasoglu et al., 2006; Large et al., 1994). With KPP, the transport of tracers by unresolved convective events is represented by increasing the vertical diffusivity coefficient to 1 m^2 s^{-1} where the water column

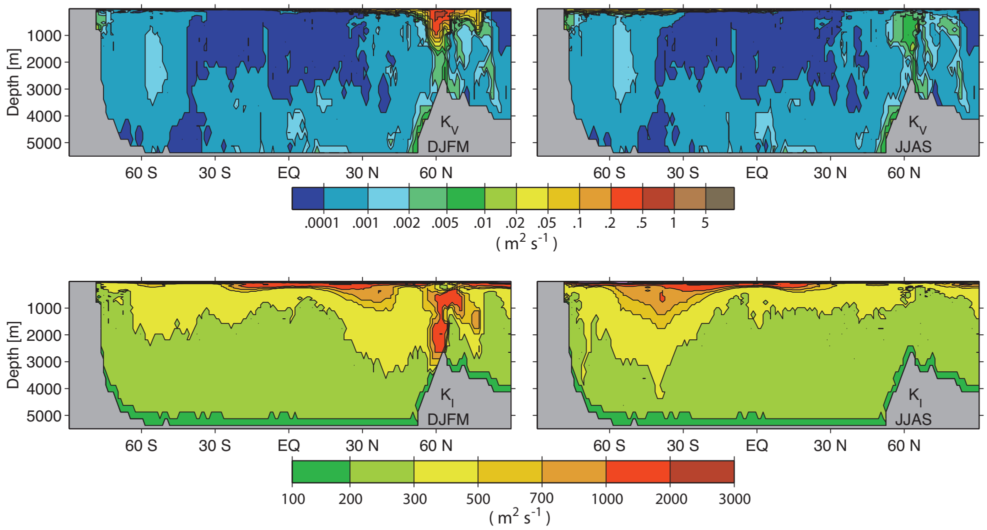

Figure 2.1: Top panels: Vertical diffusion coefficient, K_V, averaged zonally and for the period December through March (DJFM) and June through September (JJAS). Bottom panels: Isopycnal diffusion coefficient, K_I, similarly averaged. The contour scaling is approximately logarithmic and different for K_V and K_I.

becomes statically unstable. The KPP parameterization also includes a background vertical diffusivity due to internal waves that varies with latitude. It is symmetric about the Equator with a minimum value of 0.01×10^{-4} m^2 s^{-1} at the Equator, rises sharply to its mode value of 0.17×10^{-4} m^2 s^{-1}, but with a sharp peak to its maximum value of 0.30×10^{-4} m^2 s^{-1} near 30° of latitude. This background vertical diffusivity does not vary with depth, but the parameterization does include enhanced vertical diffusivities over rough topography with a maximum value of 100×10^{-4} m^2 s^{-1} to mimic the effect of abyssal tidal mixing.

Figure 2.1 shows the resulting vertical diffusivity parameter, K_V, for the December through March (DJFM) season and the June through September (JJAS) season. The seasonal changes in K_V are strongest in the North Atlantic where there is winter-time deep convection. The Southern Ocean shows much less change with the seasons.

Figure 2.1 also shows the zonally averaged isopycnal diffusivity coefficient, K_I, for the DJFM and JJAS seasons. Generally, the values are lowest along the bottom near land masses and are largest in the seasonal thermocline. There is a substantial amount of seasonality in the value of the K_I coefficient. In the North Atlantic, the value of K_I rises to over 1000 m^2 s^{-1} in winter with enhanced values extending down to $\sim$4000 m. Southern Ocean K_I values are largest during austral winter, but are generally lower than their counterpart in the north.

Also included in the model is a sill overflow parameterization that attempts to capture the unresolved transport of tracers by narrow density currents along the bottom over four key sills: in the Denmark Strait and the Faroe Bank Channel in the North Atlantic, and in the Ross Sea and Weddell Sea in the Southern Ocean (Briegleb et al., 2010; Danabasoglu et al., 2010). The parameterization produces "non-local" transport from a "source" region upstream of the sill and from an "entrainment" region partway down the slope to a "product" region in the abyssal basins downstream of the sill. The amount of water flowing from the source to the entrainment and product regions, and from the entrainment to the product region, is determined dynamically depending on the density of waters in the source, entrainment, and product regions. For our particular simulation the surface forcing resulted in water-column density profiles that produced sill overflow only in the North Atlantic sills. The conditions in the model were such that there was no sill overflow in the Southern Ocean.

To give a sense of the advective transport responsible for ventilating the deep ocean, Figure 2.2 shows the annual, DJFM, and JJAS averages for the meridional overturning circulation (MOC), for the global ocean and separately for the Atlantic basin. The Atlantic basin characterized here includes the entire North Atlantic region: the Labrador Sea, the Greenland-Iceland-Norwegian (GIN) Sea, and the Arctic in addition to the Atlantic itself. The Atlantic MOC shows a northern sinking branch that penetrates down to approximately 2750 m and carries up to $\sim$20 Sv. The global MOC shows a strong seasonal variability at

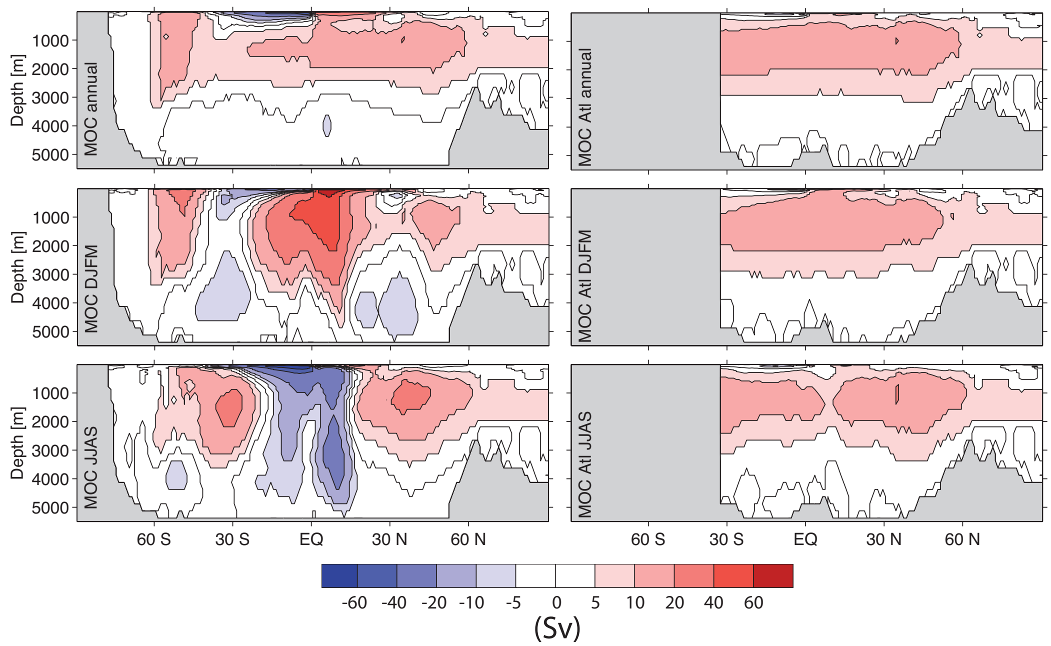

Figure 2.2: Annual, DJFM, and JJAS averages for the global (left) and for the Atlantic (right) meridional overturning circulation (MOC), in Sverdrup (10^6 m^3 s^{-1}). Red colors indicate a clockwise overturning.

low-latitudes with a peak-to-peak amplitude of ∼100 Sv that is not evident in the Atlantic MOC, indicating that the this variability is confined to the Indo-Pacific basin. This variability, likely due to the changes in the surface wind associated with the Indian Monsoon, leads to a strong tropical MOC cell that changes directions with the seasons and vanishes in the annual average.

2.5 Tracer-Transport Matrix

To capture the seasonal variability of the explicitly resolved advective currents and parameterized eddy-diffusive processes we constructed monthly-averaged tracer-transport matrices, which were formed by separating the transport matrix into three parts,

$$\mathbf{T} = -\mathbf{A} + \mathbf{D} + \mathbf{H}, \tag{2.7}$$

where **A** includes the effect of advection and the tracer-transport effects of the sill overflow parameterization, **D** includes the effect of vertical diffusion, and **H** includes the effect of horizontal diffusion. The sign convention is the same as in the POP manual (Smith et al., 2010). The separation was done primarily to facilitate the reconstruction of the operator using impulse response functions, but it also makes it possible to run the offline model with the same computationally efficient time-stepping scheme as in the parent model, which is based on an implicit scheme for **D** and different explicit time-stepping schemes for **H** and **A** (see Section 2.6). The **D** matrix was hand coded using the same second-order centered-difference scheme used in the parent model, as was done in developing the offline tracer-transport matrix of Primeau (2005). The vertical diffusivity coefficients were obtained by time-averaging the instantaneous vertical diffusivity values determined dynamically during a one-year run of the parent model.

During the same run of the parent model we also computed a set of impulse response functions (IRFs) which we used to reconstruct **A** and **H** following an approach similar to that described in Khatiwala et al. (2004). Because our parent model used a linear advection scheme without any flux limiters we did not need to use vertically smoothed impulses as recommended in Khatiwala et al. (2004). Furthermore, because the advection scheme in the version of POP2 that we used is based on a third-order upwind spatial discretization with an explicit time-stepping scheme, the response due to **A** of a passive tracer impulse in grid box (i', j', k') is guaranteed to extend no further than to two adjacent grid boxes in each direction after a single time-step. (In contrast, the action of **D**, which is time-stepped using an implicit scheme in the parent model, spreads the response to all 60 levels in the vertical in a single time-step.) The limited spread of the IRF makes it possible to compute the response to impulses separated by four grid cells in any direction simultaneously using a single tracer without any interference among the responses. Thus a set of 125 separate tracers indexed according to (i_o, j_o, k_o) with i_o, j_o and k_o cycling independently from 1 through 5, is sufficient to compute all the IRFs needed to reconstruct $\mathbf{A}$. To compute the IRFs we average the time-tendency due to an impulse initial condition which we reinitialize at the beginning of each time step to

$$\begin{gathered} C(i,j,k|i_0,j_0,k_0) = Mask(i,j,k)\delta_{i_0,i(\mathrm{mod}\ 5)}\delta_{j_0,j(\mathrm{mod}\ 5)}\delta_{k_0,k(\mathrm{mod}\ 5)}, \\ \text{for } i = 1\cdots N_x,\ j = 1\cdots N_y,\ k = 1\cdots N_z, \end{gathered} \tag{2.8}$$

in which δ_{ij} is the Kronecker delta function and $Mask(i,j,k)$ is a mask equal to one everywhere except for the "source" and "entrainment" region of the sill-overflow parameterization. *Mask* is used to zero-out C for impulses in the source and entrainment regions where the sill-overflow parameterization has been implemented. This was necessary to eliminate the interference in the response produced by the non-local transport into the product areas. (Two separate set of tracers were used to construct the IRFs for each grid box in the source and entrainment regions of the four sills. These additional IRFs were used to reconstruct the sill-overflow effect of $\mathbf{A}$.) In practice, memory constraints and the particular implementation of the IRF module required us to repeat the one-year run seven times to collect all the information needed to construct the twelve monthly transport matrices.

The resulting average tendencies, $\overline{C'}(i,j,k|i_o,j_0,k_o)$, for each of the 125 tracer impulses could then be separated into the individual IRFs, using the mask function,

$$I(i,j,k|i',j',k') \equiv \begin{cases} 1 \text{ if } (|i-i'| \leq 2 \text{ or } |i-i'| \geq N_x - 2), |j-j'| \leq 2, \text{ and } |k-k'| \leq 2, \\ 0 \text{ otherwise,} \end{cases} \tag{2.9}$$

so that

$$IRF(i,j,k|i',k',j') = \sum_{\{i_o,j_o,k_o\}=1}^{5} I(i,j,k|i',j',k')\overline{C'}(i,j,k|i_o,j_o,k_o). \tag{2.10}$$

The IRFs were then reorganized into the elements of $\mathbf{A}$ with the column index determined from (i',j',k') and the row index determined from (i,j,k). A similar process with a separate set of IRFs was used to reconstruct $\mathbf{H}$.

2.5.1 Enforcing Local Mass-Conservation

By assuming that the year-to-year changes in circulation are negligible to first order we can use the same tracer-transport matrices computed for one particular year to efficiently compute the spin-up of passive tracers without having to solve the momentum and continuity equations. One difficulty with this assumption is that the sea-surface height displacements do not average to zero in any given year. In the dynamical model strong dynamical feedbacks prevent the development of persistent trends in the sea-surface height, but in our offline transport model with a fixed circulation captured from one particular year the local divergence of the flow field that causes the sea-surface height to move up or down does not cancel if we recycle the same circulation year after year. This divergence, although small, accumulates to produce unphysical results for an implicit solver, which produces the solution that would be obtained if the tracer model was run for an infinitely long time.

To eliminate this problem we have modified the horizontal advective flow field in the surface layer of the offline model to ensure that the annual-mean vertical velocity vanishes at the sea surface. (Only gridboxes in the surface layer change volume due to variations in the sea surface height. Consequently velocity corrections are required only for the horizontal velocity in the top layer of the model.)

We obtained the correction to the velocity field in terms of a velocity potential, $(\tilde{u}, \tilde{v}) = \nabla\Phi$, with the potential determined by solving the two-dimensional Poisson equation

$$\nabla^2\Phi = -\overline{\frac{\partial \eta}{\partial t}}, \tag{2.11}$$

where $\eta(t)$ is the sea surface displacement and the overline indicates an annual average. Eq.(2.11) was solved subject to no-flow boundary conditions in the domain defined by the basin geometry of the top layer of the model. The resulting velocity corrections were generally small compared with the monthly surface current speeds – the rms change in current speed is $\sim$3%.

2.5.2 Annual Average Circulation

The annually-averaged transport operator, $\overline{\mathbf{T}}$, is computed by averaging of the transport operators constructed from the monthly-averaged circulation fields for each of the components, **A**, **H**, and **D**, which are added together, as shown in equation 2.7 to give the annually-averaged steady-state transport operator, $\overline{\mathbf{T}}$. The resulting annually-averaged transport operator is then used in equations (2.4) and (2.3). The steady-state solution of the resulting equation is obtained by setting the time-derivative to zero and directly inverting the time-independent **M** using the MUMPS multifrontal sparse-matrix solver (Amestoy et al., 2001). The ^{14}C results obtained using the annually-averaged circulation are compared with the seasonally-varying cyclo-stationary circulation in Section 2.8.2.

2.6 Offline Time-dependent Solver

To time-step the offline tracer-transport model we use 12 piece-wise constant monthly-averaged tracer-transport matrices. Within a given month the equation is stepped forward in time using an implicit first-order Euler-backward scheme for the vertical diffusion, and explicit schemes for the advection (3rd-order Adams-Bashforth), horizontal diffusion and source (first-order Euler forward):

$$\begin{aligned} \left[\mathbf{I} + \boldsymbol{\xi}_{n+1} - \Delta t\mathbf{D}\right]\phi_{n+1} &= \left[\mathbf{I} + \boldsymbol{\xi}_n\right]\phi_n + \Delta t\left[\mathbf{H}\phi_n + s(\phi_n, \boldsymbol{\xi}_n)\right] \\ &\quad - \frac{\Delta t}{12}\mathbf{A}\left[23\phi_n - 16\phi_{n-1} + 5\phi_{n-2}\right], \\ \xi_{n+1} &= \xi_n - \Delta t\mathbf{A}\boldsymbol{\iota} \end{aligned} \tag{2.12}$$

where $\boldsymbol{\iota}$ is a vector of ones and $\boldsymbol{\xi}_n$ is a diagonal matrix formed from the elements of ξ_n, which are the relative change in the surface cell thicknesses. The matrix-vector product $\mathbf{A}\boldsymbol{\iota}$ is the advective volume-flux convergence, and is non-zero only for the surface grid-cells. It does however average to zero over a full year because of the velocity corrections described in Section 2.5.1, ensuring that ξ is periodic with a period of one year. ξ_0 is initialized to $\eta_0/\Delta z_1$, where η_0 is the sea-surface height displacement saved from the parent model at the beginning of the one year run used to save the fields that are used to construct the transport operator. ϕ_n and ϕ_{n+1} are the tracer concentrations at time-step n and $n+1$. s is the source-sink function, which can depend on ϕ_n and $\boldsymbol{\xi}_n$. At the beginning of each month, the time-stepping scheme for the advective term is initialized using an Euler-forward step followed by a 2nd-order Adams-Bashforth step before switching to the 3rd-order Adams-Bashforth scheme.

2.7 Periodic Equilibrium Newton-Krylov Solver

To find cyclo-stationary equilibrium of the seasonally varying circulation model we apply Newton's method to $\mathbf{G}(\mathbf{x}(t)) = 0$, where

$$
\begin{aligned}
\mathbf{G}(\mathbf{x}(t)) &\equiv \int_t^{t+T} \mathbf{M}(t')\mathbf{x}(t') + \mathbf{s}(t')\, dt' \\
&= \mathbf{x}(t+T) - \mathbf{x}(t),
\end{aligned}
\tag{2.13}
$$

where $T = 1$ year. Given an initial iterate $\mathbf{x}_0$ we obtain the improved iterate $\mathbf{x}_1 = \mathbf{x}_0 + d\mathbf{x}_0$ by solving the following linear system

$$
\mathbf{J}d\mathbf{x}_0 = -G(\mathbf{x}_0), \tag{2.14}
$$

where $\mathbf{J} \equiv \partial G(\mathbf{x})/\partial \mathbf{x}$ is the Jacobian matrix. Unfortunately, $\mathbf{J}$ is a dense matrix because the integral in (2.13), evaluated with a time-step size of ∼3 hours, allows a tracer perturbation isolated in one grid box at time t to be propagate to every other grid box at time $t + T$. As a result, it is impossible to evaluate or even store the full Jacobian matrix in memory let alone invert it. To solve (2.14) we must therefore use a Krylov subspace method. For this we use a preconditioned generalized minimal residual method (with restarts) (GMRES) as implemented in the Matlab Newton-Krylov solver `nsoli.m` described in Kelley (2003).

2.7.1 Preconditioner

To accelerate the convergence of the Krylov-subspace solver we follow Li and Primeau (2008) in using a preconditioner of the form

$$
\mathbf{P} = \mathbf{Q}^{-1} - \mathbf{I}, \tag{2.15}
$$

where $\mathbf{Q}$ is a sparse matrix formulated in terms of the annual-average of the $\mathbf{M}$ matrix, defined in (2.4),

$$\mathbf{Q} \equiv T\,\overline{\mathbf{M}}. \tag{2.16}$$

As shown by Khatiwala (2008), the form of this preconditioner can be motivated as the inverse of a sparse approximation of the full Jacobian matrix

$$\begin{aligned}
\mathbf{J} &\equiv \frac{\partial G(\mathbf{x}(t))}{\partial \mathbf{x}(t)}, \\
&= \frac{\partial}{\partial \mathbf{x}(t)} \left[\int_t^{t+T} \mathbf{M}(t')\mathbf{x}(t') + \mathbf{s}(t)\, dt' \right], \\
&\approx \frac{\partial}{\partial \mathbf{x}(t)} \left[T\,\overline{\mathbf{M}}\,\mathbf{x}(t+T) \right], \\
&\approx \frac{\partial}{\partial \mathbf{x}(t)} \left[T\,\overline{\mathbf{M}} \left(\left(\mathbf{I} + T\,\overline{\mathbf{M}}\right)^{-1} \mathbf{x}(t) \right) \right], \\
&\approx T\,\overline{\mathbf{M}} \left(\mathbf{I} + T\,\overline{\mathbf{M}}\right)^{-1}, \\
\Rightarrow \mathbf{J}^{-1} &\approx \left(T\,\overline{\mathbf{M}}\right)^{-1} - \mathbf{I}.
\end{aligned} \tag{2.17}$$

In the Newton-Krylov applications of Li and Primeau (2008) and Khatiwala (2008) the model resolutions were sufficiently coarse to make it possible to directly compute the LU factorization of $\mathbf{Q}$. For the present model the factorization of $\mathbf{Q}$ requires nearly 256 gigabytes of memory, making it impractical to use the LU factorization of the full matrix. Motivated by the desire to apply the solver to problems involving multiple coupled tracers and by the expectation that future versions of the model will have even higher resolution we have developed a simple coarse-graining procedure for computing an approximate inverse of $\mathbf{Q}$ that requires much less memory.

The coarse-graining procedure consists of averaging successive 2×2 horizontal blocks of grid-cells and then interpolating the resulting coarse-grained field back

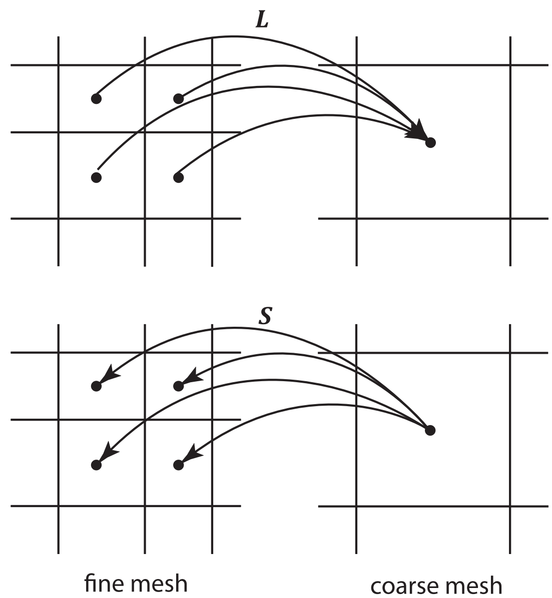

Figure 2.3: The Lump (L) and Spray (S) operators are used to implement the coarse-graining technique. The L transfers the tracer concentration on the fine grid to the coarse grid using a volume-weighted average of the fine-mesh gridboxes inside a coarse-mesh gridbox. The S operator transfers the tracer concentration on the coarse grid to the fine grid by copying the concentration in the coarse-mesh gridbox to each of the fine-mesh gridboxes inside the the coarse-mesh gridbox.

onto the full resolution grid by simply copying the tracer concentration in the coarse 2×2 block into each of the four sub-gridboxes. This process of "lumping" tracer information onto a coarser grid and of "spraying" a lumped solution back to the full grid is illustrated in Figure 2.3. It is achieved by constructing a pair of matrix operators, $\mathbf{L}$ and $\mathbf{S}$ defined as follows:

$$\begin{aligned} \mathbf{S}' &\equiv \mathbf{I}_z \otimes (\mathbf{A}_x \otimes \mathbf{A}_y)\,, \\ \mathbf{L} &\equiv \mathbf{diag}(\mathbf{S}'\mathbf{w})^{-1}\,\mathbf{S}'\,\mathbf{diag}(\mathbf{w}), \end{aligned} \tag{2.18}$$

where $\mathbf{w}$ denotes a column vector whose elements are the gridbox volumes, prime denotes matrix transpose, $\otimes$ denotes the Kronecker product, $\mathbf{A}_x \equiv \mathbf{I}_{\frac{N_x}{2}} \otimes \begin{bmatrix} 1 & 1 \end{bmatrix}$ and $\mathbf{A}_y \equiv \mathbf{I}_{\frac{N_y}{2}} \otimes \begin{bmatrix} 1 & 1 \end{bmatrix}$. We refer to the $N/4 \times N$ restriction matrix $\mathbf{L}$ as the lump operator because it lumps four neighboring grid-cell concentrations using a volume weighted average to produce a coarse grained concentration field. The $N \times N/4$ interpolation matrix $\mathbf{S}$ corresponds to the spray operator because it copies the concentration in the coarse grained grid box into each of the 4 sub-gridboxes of the full resolution model. After masking out the land points, the lump and spray operators are applied to the $N \times N$ operator $\mathbf{Q}$ to reduce it to a $\sim N/4 \times N/4$ matrix

$$\mathbf{Q}_c = \mathbf{LQS}, \tag{2.19}$$

without appreciably changing its sparseness. The resulting preconditioner is then

$$\mathbf{P} = \mathbf{S}\mathbf{Q}_c^{-1}\mathbf{L} - \mathbf{I}. \tag{2.20}$$

Note that the $\mathbf{L}$ and $\mathbf{S}$ matrices that pre- and post- multiply $\mathbf{Q}$ in (2.19) do not cancel with those that post- and pre-multiply $\mathbf{Q}_c^{-1}$ in (2.20) because they are not square and therefore not invertible.

In summary, each Krylov iteration consists of time-stepping the offline-tracer transport model forward in time for one year, computing the drift in the tracer concentration between the beginning and the end of the one-year run, and then "multiplying" the resulting residual drift by P. In practice we do not explicitly form the matrix P or the inverse matrix $\mathbf{Q}_c^{-1}$. Instead we apply the preconditioner by lumping the resulting residual drift onto the coarser grid, applying the inverse of $\mathbf{Q}_c$ by doing the backsolve with the precomputed lower and upper (LU) triangular factors, and spraying the result back onto the fine grid before subtracting the residual drift from the result. For tracers such as radiocarbon whose source terms depend only linearly on concentration, the *LU* factorization needs to be done only once.

2.8 Results

We applied the solver to the natural radiocarbon equations described in Section (2.3). We first describe the solver's convergence rate and the effect of seasonal variations in the transport operator on the annually averaged equilibrium Δ^{14}C distribution. Then we present the resulting Δ^{14}C distributions, which we compare to observations.

2.8.1 Convergence Rate

Figure 2.4 shows the convergence to the equilibrium solution expressed as the root-mean-square (rms) drift in the Δ^{14}C for three cases: (1) The explicit time-stepping approach to equilibrium starting from an initial state obtained by interpolating the GLODAP gridded product onto the model grid. This case corresponds to the convergence rate that would have been obtained if radiocarbon had been simulated using the full parent model. (2) The approach to equilibrium using the implicit Newton-Krylov solver initialized using the interpolated GLODAP state and (3) the Newton-Krylov solver initialized using the steady-state solution based on the annually-averaged circulation. The latter approach would be particularly useful for applying the method to a tracer for which there are insufficient observations to use as an initial estimate.

Using time-stepping a root-mean-squared (rms) residual drift of 4×10^{-2} ‰/year was obtained after 100 model years of simulation. Using the Newton-Krylov solver initialized from GLODAP, the rms drift dropped to 4×10^{-4} ‰/year after

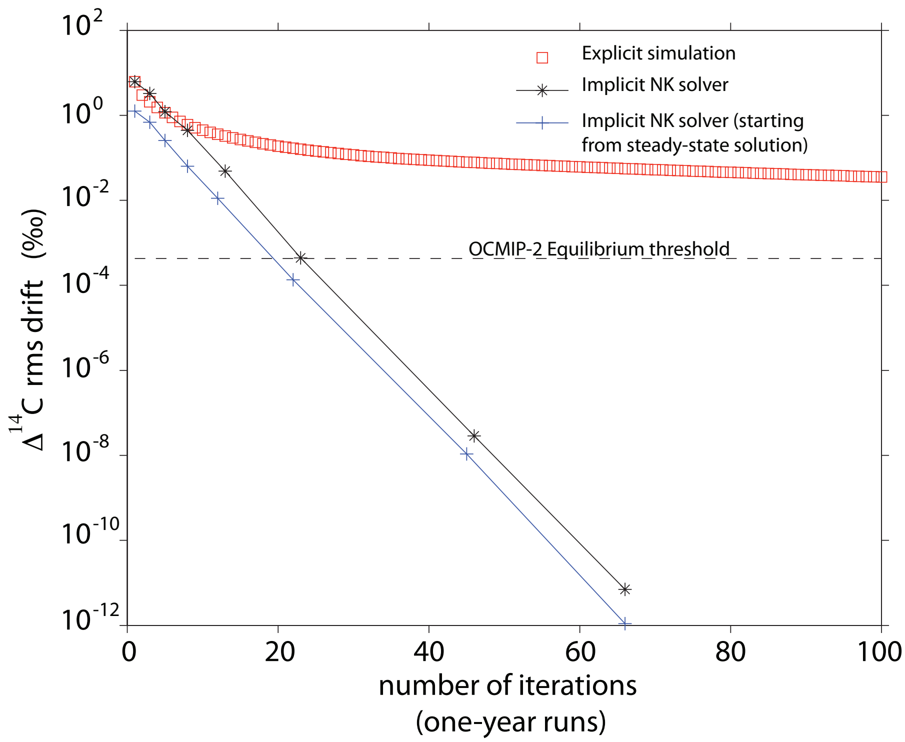

Figure 2.4: Convergence rate for Δ^{14}C approach to equilibrium for the cases of: (1) a usual time-dependent simulation initialized from the GLODAP observations interpolated onto the model grid (red-squares); (2) using the Newton-Krylov solver with the same initial iterate as used for the time-dependent case (black asterisks); and (3) using the Newton-Krylov solver with an initial iterate obtained by directly solving the steady-state of the model based on the annually averaged transport-operator (blue pluses). After 5 Newton iterations (equivalent to 22 model years in case 3, and 23 model years in case 2) the OCMIP-2 equilibrium criteria has already been met.

5 Newton iterations (corresponding to 23 years of simulation), at which point the OCMIP-2 equilibrium requirements for Δ^{14}C were met, i.e. more than 98% of the ocean volume had a Δ^{14}C drift of less than 10^{-3} ‰/year. After 7 Newton iterations (and a total of 66 years of simulation), the rms Δ^{14}C drift was 7×10^{-12} ‰/year, and the Newton-Krylov solver stopped because it had reached our prescribed error tolerance of 10^{-9} ‰/year. For the case where the Newton-Krylov solver was initialized using the steady-state solution, the OCMIP-2 equilibrium threshold was reached after 22 years of simulations. After 7 Newton iterations (and a total of 66 years of simulation), the rms Δ^{14}C drift was 1×10^{-12} ‰/year. As expected, because of the linearity of Eq. (2.3), the rate of convergence was independent of the initial iterate used.

In terms of cpu time, the computational overhead associated with the Newton-Krylov solver (`nsoli.m`) was negligible compared to the cost of evaluating Eq. (2.13) i.e. of the cost of time-stepping the model forward in time for one year. In all our test cases we kept the GMRES restart parameter fixed at a value of 100, implying that the Newton-Krylov solver may store up to 100 three-dimensional tracer fields. This memory requirement, while substantial, is considerably less than the memory requirements needed to factor (∼130GB) and store (∼77GB) the LU factors of Q_c used for the preconditioner. It is conceivable that further improvements in the efficiency of the solver could be achieved by increasing the restart parameter, but we did not explore this possibility.

We also investigated other cases. If we initialize the explicit time-stepping method using the solution for the steady-state circulation model, the rms residual drift after 100 years is 1.2×10^{-2} ‰/year. The rate of convergence is similar to that shown for the case in which the model was initialized with the GLODAP state. Using the Newton-Krylov solver without a preconditioner, the rate of convergence is no better than that obtained from the time-stepping method.

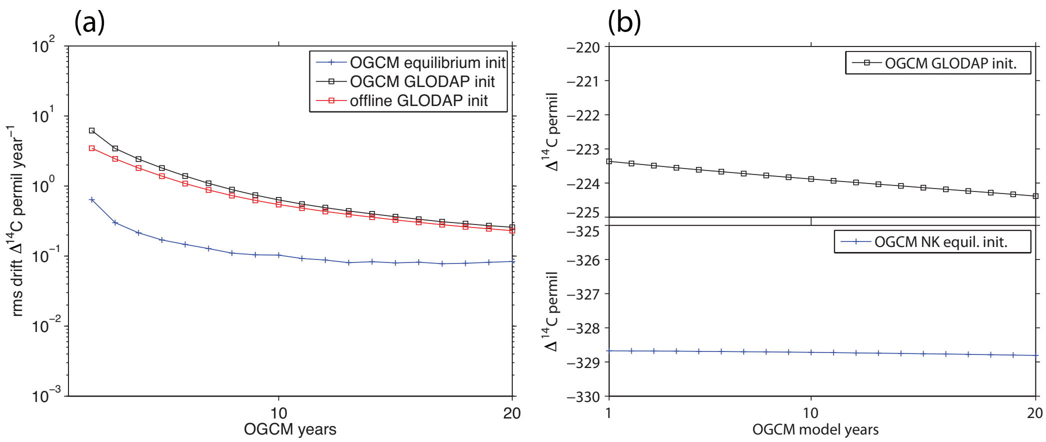

Figure 2.5: (a) Globally averaged rms drift for Δ^{14}C in a 20-year run of (i) the parent OGCM initialized using the offline equilibrium solution obtained with the NK solver (blue +), (ii) of the parent OGCM initialized using the GLODAP prebomb radiocarbon interpolated on the model grid (black squares), and (iii) of the offline model also initialized with GLODAP (red squares). (b) The Δ^{14}C in the deep North Pacific below 1000 m and north of 10°N as a function of time for the OGCM runs initialized with GLODAP (upper panel) and with the offline equilibrium solution (lower panel). Note that the y-axis for the upper and lower panels have the same scale but are offset by -105‰.

The rms of the residual after 100 years was 6.4×10^{-3} ‰/year, and there was no further progress during the subsequent 300 Krylov iterations, illustrating the critical importance of an effective preconditioner.

To demonstrate that the Newton-Krylov (NK) solution obtained using the offline model is an approximate equilibrium of the parent OGCM, we conducted two 20-year radiocarbon simulation in the parent model to compare the drift for the case where the model is initialized with the NK solution to the case where the model is initialized using the GLODAP pre-bomb radiocarbon. For these runs the dynamical state of the OGCM continued to evolve from the state at the end of the 150 year spin-up run. We used the same simplified representation for the air-sea exchange of ^{14}C that we used in the offline model. Figure 2.5(a) shows the globally averaged rms Δ^{14}C drift as a function of time for the two different initial conditions. For comparison we have reproduced on this plot the first 20-years of the rms Δ^{14}C drift for the offline model initialized using the GLODAP data (see Fig. 2.4). The offline model and the parent OGCM show similar trends in the rms drift when initialized with GLODAP but there is nevertheless a significant difference that is most likely due to the approximation of the seasonal cycle in the offline model with a piecewise-constant transport operator with monthly resolution. The OGCM initialized with the offline model's equilibrium state has a substantial drift at the beginning of the run but decreases rapidly to less than 0.09‰ at the end of the run. This drift is smaller than the GLODAP-initialized run by a factor of ~10 at the beginning of the run and by a factor of ~4 at the end of the 20 year run. The fact that the NK-equilibrium is only an approximate equilibrium to the parent model is most likely due to the poorly resolved seasonal cycle in the offline model. It should be possible to reduce this error by approximating the seasonal cycle in the offline model using two or more transport matrices per month. Another possibility would be to perform the one-year runs in the Newton-Krylov solver with the parent model instead of with the monthly transport matrices. In such a solver the transport matrix would be used only for the preconditioning step.

In the deep ocean where the seasonal cycle is less important, we expect the offline model to better capture the parent model's circulation. Figure 2.5(b) shows the averaged Δ^{14}C value for the deep North Pacific (below 1000 m and north of 10°N) where the tracer equilibration times are longest. The upper panel shows the GLODAP-initialized run and the lower panel shows the NK-initialized run. The scale for the y-axis is the same for both panels except for an offset of -105‰. The run initialized with the offline model's equilibrium solution shows no discernable trend ($\lesssim$ 0.007‰/year) whereas the run initialized with GLODAP shows a downward trend of approximately 0.05‰/year. Extrapolating this trend gives an estimate of ~2000 years for the model initialized using GLODAP to reach -329‰, the approximate equilibrium found by the offline NK solver. This estimate is likely to be an underestimate by a factor of two or more because the approach to tracer equilibrium is expected to follow an exponentially decaying function rather than a linear trend.

2.8.2 Importance of circulation seasonality on $\Delta^{14}C$

Figure 2.6 shows the differences in the $\Delta^{14}C$ solutions obtained with and without the seasonality in the transport operator. The results are shown as a percent change of the average of the seasonally-varying solution relative to the solution based on the annually-averaged transport operator. Positive percent changes indicate more depleted $\Delta^{14}C$ values, i.e. older waters. With a few exceptions, discussed below, most of the differences are less than 10%. Overall, the bias from ignoring the seasonal variations in the circulation results in $\Delta^{14}C$ values that are 1.5% less depleted. All basin zonal averages show increases in radiocarbon age (i.e. more depleted $\Delta^{14}C$ relative to the solution based on the annually-averaged transport) in the upper part of the ocean between 100 and 1000m. The differences are proportionally largest in areas of strongest seasonal variability in the circulation. The difference between the solutions based on the cyclo-stationary and annually-averaged transport is especially notable in the northern part of the Indian Ocean where the overturning circulation changes sign on seasonal timescales (see Figure 2.2).

In the Indian Ocean the difference between the cyclo-stationary solution and the steady-state solution penetrates all the way to the bottom of the basin with the cyclo-stationary solution having $\Delta^{14}C$ values that are more than 30% more depleted in the depth range between 500 and 1000 m. The surface of the Indian Ocean, on the other hand, shows either no difference, or less depleted $\Delta^{14}C$

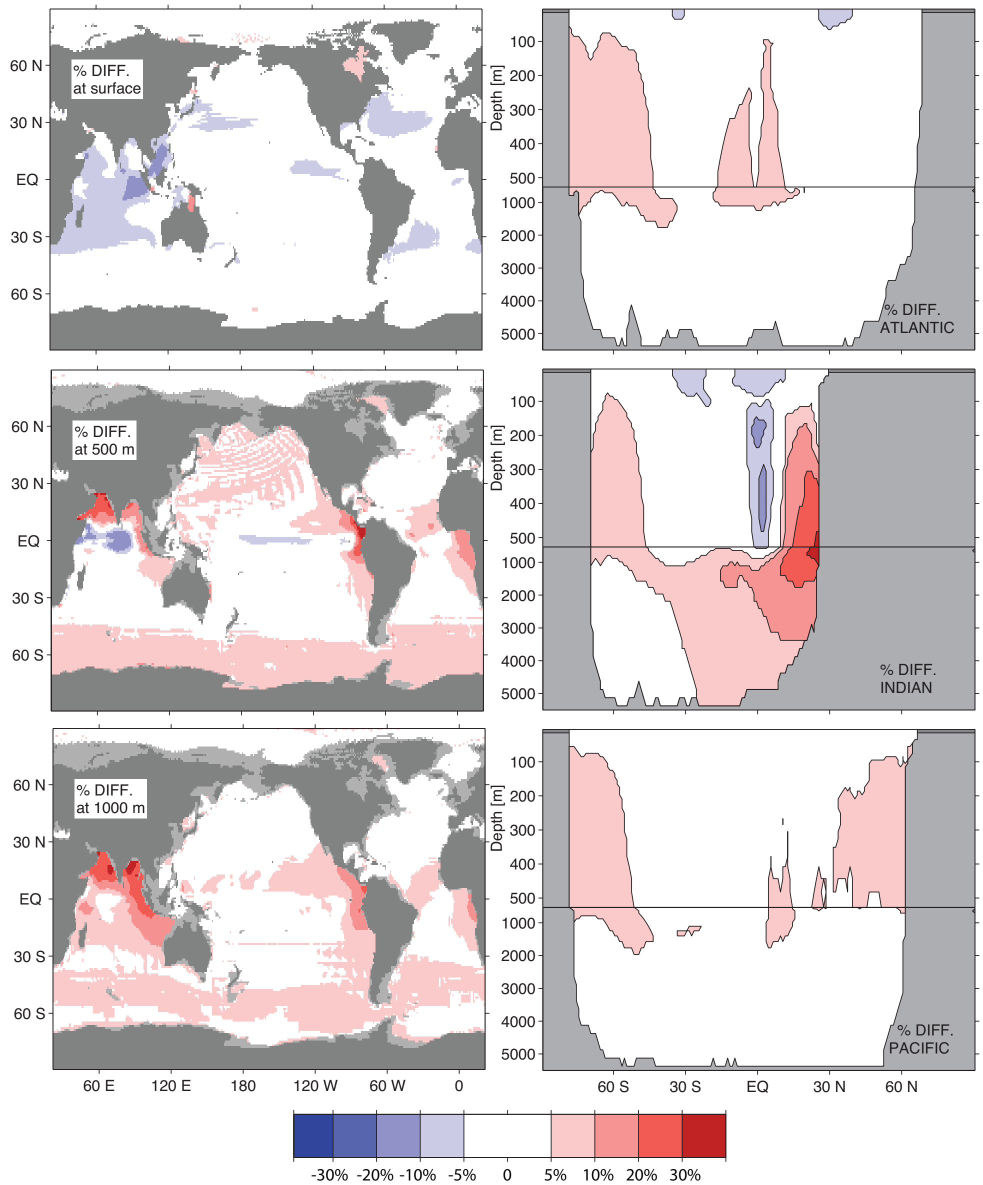

Figure 2.6: $\Delta^{14}C$ percent change between the annually-averaged cyclo-stationary solution and the steady-state solution obtained from the annually-averaged transport operator. Positive percent values indicate that the cyclo-stationary solution has a more depleted $\Delta^{14}C$ value, i.e. that the water is older for the cyclo-stationary solution.

values in the cyclo-stationary case. The Arabian Sea, the Bay of Bengal, and the Eastern Equatorial Pacific all have more depleted $\Delta^{14}C$ values in the cyclo-stationary solution in the depth range between 500m to 1000m. Ignoring the seasonal cycle of the circulation leads to a spurious less-depleted $\Delta^{14}C$ in these strongly seasonally-varying zones.

Also more depleted in the cyclo-stationary solution are the shadow-zones of the Eastern Pacific and Atlantic basins. Both maps at 500m and the 1000m show regions that are up to 20% more depleted along the coast of Africa and the Americas in the solution based on the seasonally varying circulation. These more depleted regions are also visible in the zonal-averaged views in the depth range between 100m and 1000m in the Atlantic, and in the depth range between 400m and 1500m in the Pacific.

In the depth range between 100m and 1000m the Southern Ocean of the cyclo-stationary solution has $\Delta^{14}C$ values that are 5-10% more depleted than the solution based on the steady time-averaged circulation. In the same depth range the North Pacific is also less well-ventilated in the cyclo-stationary solution compared to the solution based on the steady circulation with $\Delta^{14}C$ values that are more depleted by at least 5%.

2.8.3 Comparison of the Modeled $\Delta^{14}C$ to GLODAP

The $\Delta^{14}C$ value of surface waters depends on the balance between air-sea gas exchange which brings in CO_2 that is enriched in radiocarbon and the upwelling of older waters that are depleted in radiocarbon. Figure 2.7 compares the zonally averaged $\Delta^{14}C$ value of surface waters in the model with the prebomb radiocarbon estimate from GLODAP. Only the grid cells for which GLODAP data is available were used for the comparison. The light-gray band around the GLO-

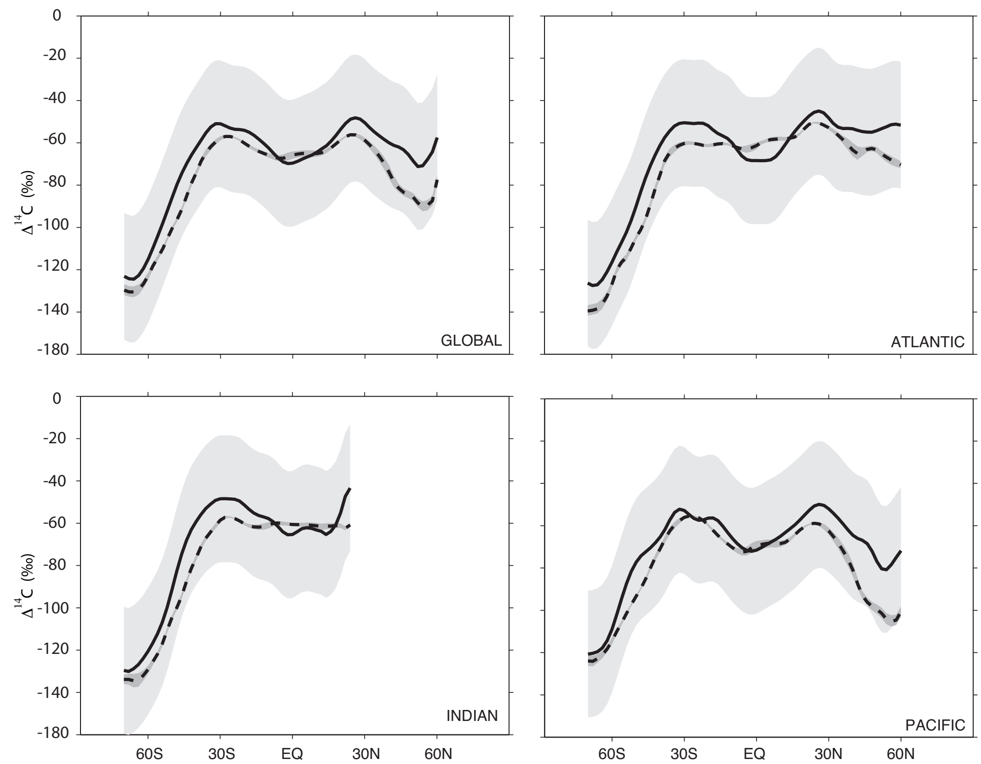

Figure 2.7: Δ^{14}C in the surface layer versus latitude. The black solid line is the GLODAP data; the dashed line is the annualy-averaged cyclo-stationary solution. The light gray bands are ±30‰ from the GLODAP data. The dark gray band around the dashed line represents the range in the seasonal cycle values. The panels show the average by latitude for the global ocean and for each major basin.

DAP values corresponds to an upper bound error estimate of ±30‰ (Gebbie and Huybers, 2012). A comprehensive error analysis of the GLODAP natural radiocarbon is not available, but sources of uncertainty for the GLODAP values are laboratory-based counting errors (Sabine et al., 2005); the separation of $\Delta^{14}C$ values into natural and bomb-produced components (Rubin and Key, 2002), which includes regression errors of measured dissolved inorganic carbon (DIC) radiocarbon on potential alkalinity and on coral radiocarbon (Rubin and Key, 2002); and mapping errors (Key et al., 2004). The dark-gray band around the POP2 simulated values corresponds to the seasonal variation in the simulated $\Delta^{14}C$ value. Interestingly, the error made in ignoring the seasonal variability in the circulation (see Fig. 2.6) is much larger than the amplitude of the seasonal cycle in the solution that properly accounts for the seasonally varying circulation.

In the Southern Ocean, south of 30°S, the simulated $\Delta^{14}C$ is slightly more depleted than the observational estimate. The dip in the equatorial region in the GLODAP data is underestimated in the Atlantic and Indian basins, but not in the Pacific basin. In both the North Atlantic and the North Pacific, the simulated values are more depleted than the GLODAP values. Despite these differences, the simulated surface $\Delta^{14}C$ values are mostly within the limit of uncertainty in the observations. In the North Pacific the model $\Delta^{14}C$ is close to the uncertainty upper bound which indicates the the model surface value is potentially in disagreement with the observations.

Our simulations used a very simple formulation for the air-sea exchange of radiocarbon. Further refinement of the air-sea gas exchange parameterization to include the effect of spatially varying air-sea CO_2 fluxes is expected to be important for the purpose of simulating the transient pulse of bomb radiocarbon (Krakauer et al., 2006), but for the purpose of simulating the prebomb radiocarbon component the simple parameterization appears adequate – the model's

$\Delta^{14}C$ values at the surface matched the observational estimates within their uncertainties in all the basins except perhaps in the North Pacific. The possible discrepancy in the North Pacific is likely due to the upwelling of deep waters in the model that are depleted by more than 80‰ compared to the observations and probably not the result of inadequacies of the simple air-sea gas-exchange parameterization.

Figure 2.8 compares the simulated $\Delta^{14}C$ values to the GLODAP estimates in the interior of the ocean. In agreement with the observations, the modeled $\Delta^{14}C$ values are less depleted (younger) in the Atlantic, showing the substantial influence of ventilation from the Labrador Sea and the GIN Sea. In these North Atlantic waters the match between the model and GLODAP is excellent. However, the aging of waters as one moves southward in the model towards the Southern Ocean and northward into the Pacific and Indian Oceans is much greater in the model than in the GLODAP observations. In the North Pacific the difference between the model and GLODAP is most extreme, with the POP2 model $\Delta^{14}C$ values reaching below -320‰ over a large portion of the water column, whereas the most-depleted GLODAP values are close to -240‰. This difference between the model and the observations is significantly greater than the 30‰ limit on the uncertainty in the GLODAP estimate.

Figure 2.9 shows the model ventilation deficiencies using vertical $\Delta^{14}C$ profiles separated by latitude band for each of the major ocean basins. Looking from the North Atlantic to the Southern Ocean (right to left in the figure), there is good agreement for water in the north end of the basin, where there is strong convection. There is a small more-depleted bias moving southward. This bias is strongest on the Eastern side of the basin as seen in Figure 2.8. The sections of the Southern Ocean all have similar biases with the model $\Delta^{14}C$ value becoming progressively overly-depleted with increasing depth. In the Indian Ocean the

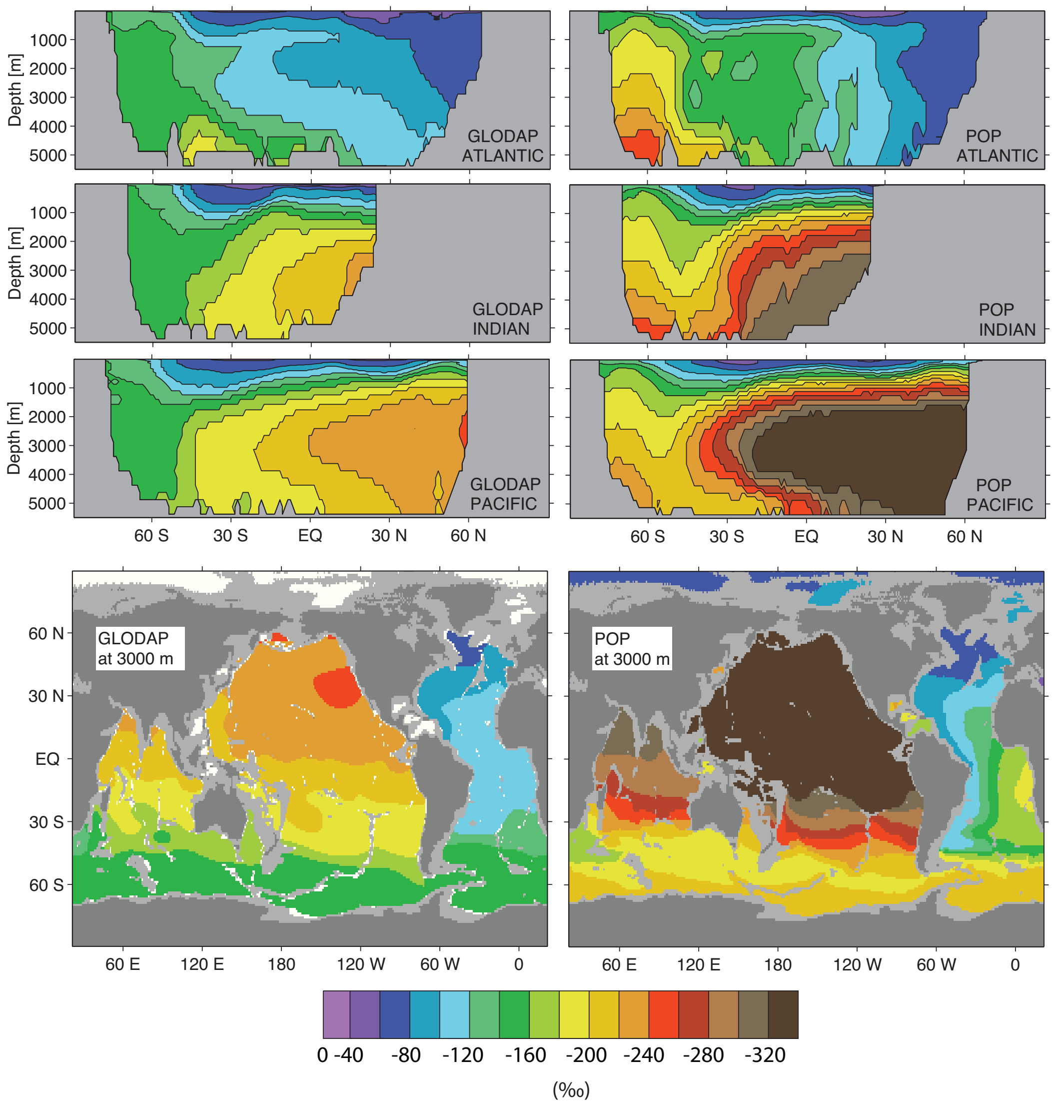

Figure 2.8: Equilibrium $\Delta^{14}C$ (‰), simulated using the seasonally-cycling transport operators, compared with GLODAP gridded observational data. The GLODAP data is in the right-hand column; the simulated values in the left-hand column. The zonal average views are the Atlantic, Indian, and Pacific ocean basins. The layer views are at depths of 3000 m.

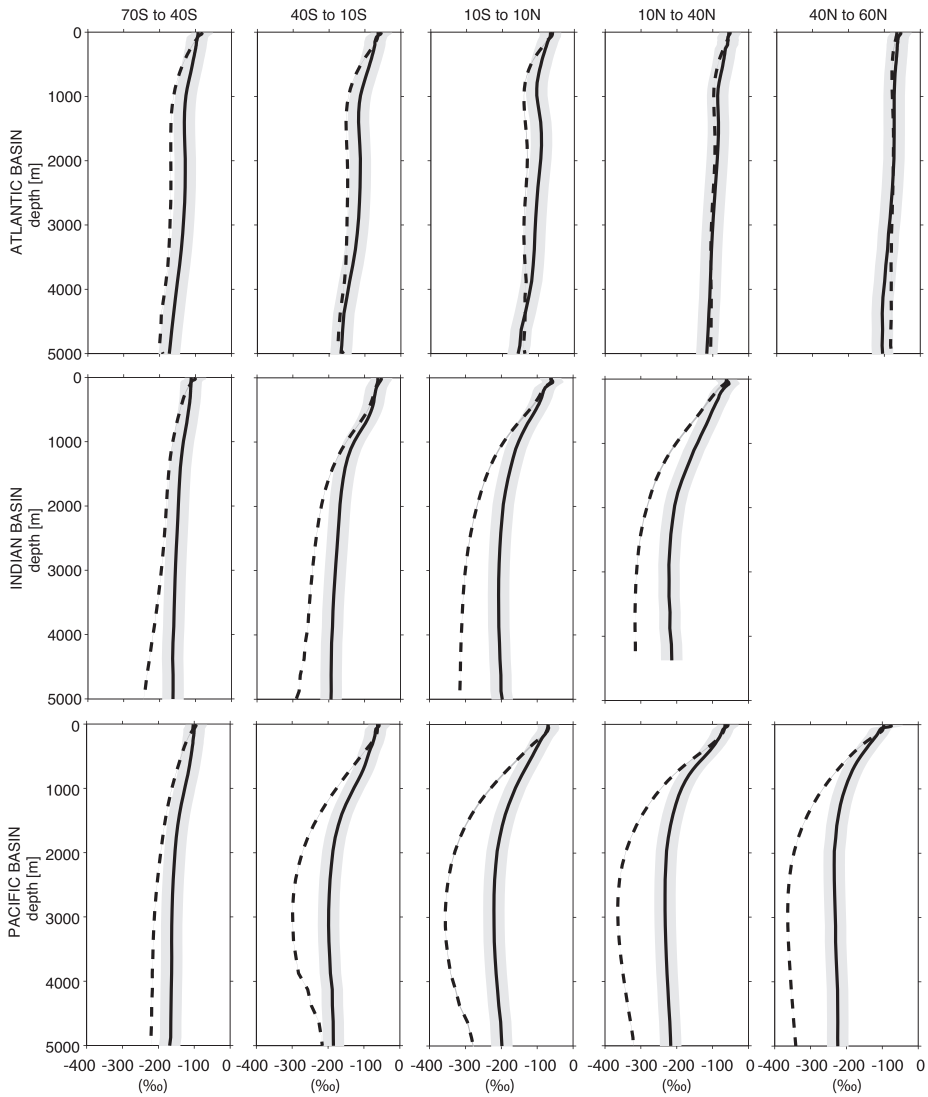

Figure 2.9: Depth profiles of Δ^{14}C in (‰) by latitude bands, in the Atlantic, Indian, and Pacific. The solid black line is GLODAP data; the dashed line is the simulated value. The light gray band is ± 30‰ from the GLODAP value. The dark gray band around the dashed line gives the seasonal variation in the value: this is nearly invisible on this scale.

bias increases moving northward (left to right), with the largest biases at depth. Moving northward in the Pacific Ocean, the bias increases continuously, but unlike the case of the Indian Ocean, the maximum bias (an extremely depleted Δ^{14}C value of -370‰) is centered above the bottom at a depth near 3000 m. The model's C14-age difference between the North Pacific at 3000 m and the surface of the Southern Ocean where the bulk of the North Pacific waters at 3000 m have last been in contact with the surface is $\sim$ 2600 years, which makes it more than two times bigger than the corresponding GLODAP value of only $\sim$ 1250 years. The bulge at 3000 m suggests that while the northward flow along the bottom is sluggish, southward flow in the mid-depth region of 3000 m further exacerbates the difference.

2.9 Discussion

We found that the model's North Atlantic Δ^{14}C values matches well with the GLODAP data throughout the whole water column. The sill-overflow parameterization for the Denmark Strait and the Faroe Bank Channel, which were actively producing overflows in our simulation, appear to be successful at ventilating the deep North Atlantic. We speculate that the fact that the sill-overflow parameterization did not produce any overflows in either the Ross Sea or Weddell Sea is partly responsible for the Δ^{14}C biases observed in the simulation – a more vigorous rate of bottom water formation in the Southern Ocean would help improve the ventilation of the Indian, Pacific and South Atlantic basins. It is not so clear what combination of changes to the surface forcing or to the sub-gridscale mixing parameterizations would be needed in order to produce a density profile that is favorable to initiating overflows in the Southern Ocean. Another likely cause for the weak contribution from the Southern Ocean to the model's deep

Reference	Model	Horizontal Resolution lat $\times$ lon	Vertical Levels	GM ?	Most-depleted Pacific $\Delta^{14}C$ (‰)
Maier-Reimer and Hasselmann (1987)	Hamburg	$5° \times 5°$	10	N	-240
Toggweiler et al. (1989b)	GFDL Bryan-Cox	$4.5° \times 3.75°$	12	N	-250
Bacastow and Maier-Reimer (1990)	Hamburg HAM OCC 1	$5° \times 5°$	10	N	-240
Heinze and Maier-Reimer (1991)	Hamburg HAM OCC 2	$3.5° \times 3.5°$	11	N	-190
Maier-Reimer (1993)	Hamburg HAM OCC 3	$3.5° \times 3.5°$	15	N	-220
England (1995)	GFDL Bryan-Cox	$4.5° \times 3.75°$	12	N	-170
Duffy et al. (1997)	LLNL MOM 1.1	$3° \times 3°$	15	Y	-250
England and Rahmstorf (1999)	GFDL MOM	$4.5° \times 3.75°$	21	Y	-260

Table 2.1: Ocean model studies before OCMIP-2 where$\Delta^{14}C$ was used to validate or study the model. "GM?" states whether or not the Gent-McWilliams parameterization was used.

Reference	Model	Horizontal Resolution lat × lon	Vertical Levels	GM ?	Most-depleted Pacific $\Delta^{14}C$ (‰)
Maier-Reimer (1993)	MPIM Hamburg	$5° \times 5°$	22	N	-220
Yamanaka and Tajika (1996)	IGCR	$4° \times 4°$	17	N	-250
Large et al. (1997)	NCAR (MOM1.1)	$1.8 - 0.8° \times 3.6°$	25	Y	-230 (Orr)
Madec et al. (1998)	IPSL OPA8† offline	$1.5° \times 2°$	30	Y	-190 (Orr)
Goosse and Fichefet (1999)	UL ASTR offline OCCM	$3° \times 3°$	20	N	-200 (Orr)
Matear and Hirst (1999)	CSIRO	$3.2° \times 5.6°$	21	Y	-270 (Orr)
Gordon et al. (2000)	SOC HadCM3L	$2.5° \times 3.75°$	20	Y	-190 (Orr)
Guilderson et al. (2000)	LLNL GFDL MOM	$2° \times 4°$	23	Y	-210
Follows et al. (2002)	MIT	$2.8° \times 2.8°$	15	Y	-200 (Orr)
Gnanadesikan et al. (2004)	PRINCE	$3.75° \times 4.5°$	24	Y	-220 : -340

Table 2.2: Ocean general circulation model studies participating in OCMIP-2 where$\Delta^{14}C$ results were submitted for the comparison. The references give descriptions of the models. If the reference does not contain the $\Delta^{14}C$ results, then the result for the most-depleted Pacific $\Delta^{14}C$ value was obtained from the Orr (2002) summary of the results. If more than one value is given as the most-depleted Pacific $\delta^{14}C$ value, the study produced the range of results given. Model with a terrain-following coordinate system is marked by †.

Reference	Model	Horizontal Resolution lat $\times$ lon	Vertical Levels	GM ?	Most-depleted Pacific $\Delta^{14}C$ (‰)
Matear (2001)	MOM2	$4.25° \times 3.75°$	12	N	-240
Roussenov et al. (2004)	MICOM2.7†	$1.4° \times 1.4°$	7	N	-250
Butzin et al. (2005)	Hamburg	$3.5° \times 3.5°$	22	N	-220
Muller et al. (2006)	Bern3D	$10° \times 10°$	32	Y	-230
Galbraith et al. (2011)	GFDL MOM4p1	$0.6 - 3.4° \times 3.6°$	28	Y	-200
Graven et al. (2012)	POP2	1-2° $\times$ 3.6°	25	Y	-300

Table 2.3: Ocean model studies post- OCMIP-2 where $\Delta^{14}C$ was used to validate or study the model. Isopycnal models are marked with a †.

water masses is likely due to the difficulty of representing in a one-degree resolution model the sea-ice interactions needed for deep water formation along the Antarctic continent.

It is interesting in this regard to compare the excessively depleted Δ^{14}C values obtained with our model, -370‰, to the most-depleted Δ^{14}C values obtained in previous modeling studies. Tables 2.1, 2.2, and 2.3 list previous studies that presented Δ^{14}C simulations done with ocean general circulation models. The tables also list the resolution of the models and whether or not the model used the GM parameterization. Several of the studies listed in the table ran multiple radiocarbon simulations with different forcing or different sub-gridscale parameterizations. Where more than one Δ^{14}C value is given, it indicates the range of values that were found in the study; otherwise the authors' pick of the "best" simulation result is shown.

Table 2.1 lists studies that were made before the OCMIP-2 era. Most of the models are early versions of models that are in use today. All of them have horizontal resolutions that are coarser than $3^\circ \times 3^\circ$ and have between 10 and 21 levels in the vertical. Their most-depleted North Pacific Δ^{14}C values range from -170‰ to -260‰. Contrary to our model results, the studies that did not match the observed estimate tended to produce deep North Pacific Δ^{14}C minimums that were insufficiently depleted. The two models with the most depleted North Pacific Δ^{14}C values, (Duffy et al., 1997; England and Rahmstorf, 1999), were produced with models that used the GM parameterization, which is also included in our version of POP2. Sensitivity experiments performed in these two studies showed that the GM isopycnal-layer thickness diffusion tended to limit the depth of deep convection in the model and as a result tended to slow the renewal rates of the deep Pacific Ocean waters.

Table 2.2 lists studies that were submitted to the OCMIP-2. See Doney et al. (2004), Orr (2002), Dutay et al. (2004), and Matsumoto et al. (2004) for studies focused on comparing the results from the OCMIP-2 models. The horizontal resolution for these models ranged from 5° to 2° in the zonal direction and from 0.8° to 5° in the meridional direction. The vertical resolution ranged from 15 to 30 levels. Excluding the PRINCE model, the most-depleted North Pacific $\Delta^{14}C$ ranged from -190‰ to −250‰. The NCAR MOM1.1 model, a fore-runner of the POP model, had a maximum-depleted value of −230‰, one of the best matches with observations.

The PRINCE model $\Delta^{14}C$ value of −340‰ was an outlier; however, the same modeling group also submitted an alternate version of the model with an improved eddy-diffusion parameterization that had a most-depleted North Pacific $\Delta^{14}C$ value of −220‰, which is in reasonable agreement with the observational estimate. This alternate version of the model described in Gnanadesikan et al. (2004), showed that a proper calibration of the model's eddy-diffusive parameterizations could produce acceptable $\Delta^{14}C$ distributions without negatively impacting the simulation of other tracers such as temperature, salinity, oxygen, phosphate and CFC-11.

Table 2.3 lists more recent studies performed after the OCMIP-2 era. These models have a broad range of resolution ranging from 10° × 10° to 1.4° × 1.4° in the horizontal, and with vertical resolutions ranging from 7 to 32 levels. All but one of these studies produced minimum North Pacific $\Delta^{14}C$ values that are in agreement with the GLODAP estimate. Interestingly, the one model that produced a minimum $\Delta^{14}C$ value that is outside the observational error estimate, (Graven et al., 2012) used the same POP2 model as our study, but configured with a substantially coarser vertical and horizontal grid.

Taken together, these studies show that coarse resolution models were generally able to simulate prebomb $\Delta^{14}C$ distributions that agreed reasonably well with the observationally based estimate. We believe that higher resolution models should be able to do as well or better, provided that modelers have the ability to perform enough radiocarbon simulations to properly calibrate sub-gridscale parameterizations. Doing so should lead to improvements in the representation of deep-ocean ventilation processes in their models.

2.10 Conclusions

We have presented an offline implicit solver for obtaining the equilibrium prebomb radiocarbon distribution in an ocean circulation model of moderately-high resolution. The solver uses a Newton-Krylov method with a preconditioner based on a direct LU factorization of a coarse-grained annually-averaged transport matrix. We expect that the coarse-graining method we presented here will provide a general strategy for developing effective preconditioners that will make it possible to apply computationally-efficient Newton-Krylov solvers to models of increasing resolution.

While tuning the physical parameters of an ocean model will require on-line spin-up of the dynamics of the parent model, the implicit solver should be useful for providing ventilation diagnostics of the deep ocean that can be computed without the need for long runs of the parent dynamical model. We have shown that this solver makes it practical to use $\Delta^{14}C$ as a diagnostic for evaluating the deep-ocean ventilation of ocean models currently being developed for coupled ocean-atmosphere climate models.

For our application of the solver to the CESM POP2 model we found that the simulated $\Delta^{14}C$ values agree well with the GLODAP estimate at the sea surface and in the North Atlantic, but that there are significant biases in the deep North Pacific with Δ^{14}C values that are overly depleted by up to $\sim$110‰. This bias is larger than that obtained in all previously published radiocarbon simulations even though the resolution of this model is better than that used in any previously published prebomb radiocarbon simulation.

While we believe that increasing the resolution of ocean models is necessary for improving the circulation of ocean models, our results show that improvements in fidelity with increasing resolution are not automatic. Substantial efforts must be dedicated to calibrating sub-gridscale eddy-diffusive parameterization and to improving surface forcing fields. Natural radiocarbon provides a useful metric with which to evaluate the ventilation of the deep ocean in models and our implicit solver makes it computationally feasible to apply this metric.

Chapter 3

Characterizing the ventilation rate in the ocean component of CESM using an offline tracer transport model

3.1 Abstract

The water mass ventilation characteristics of the ocean component of the Community Earth System Model (CESM), the Parallel Ocean Program, version 2 (POP2), are diagnosed using a steady-state offline version of the ocean model. Characteristics examined are: (i) ideal ventilation age, also known as the mean last-passage time from the sea surface; (ii) the fractions of water from the surface of source ocean regions that are resident in various regions; (iii) the fraction of ventilated water per latitude and per surface source region resident in the various regions; and (iv) the ventilation age of the fractions from the various source

regions. The analysis shows that POP2 captures much of the action observed in the real ocean on a global basis. However, in the deep Pacific and Indian oceans, the ventilation ages of water masses show that the circulation is sluggish compared to observational constraints. In the POP2 model, 51% of the global ocean water is ventilated from the North Atlantic, and 39% from the Southern Ocean.

3.2 Introduction

The exchange of water masses between the surface mixed layer and the interior ocean is an important process for the climate system. The transport of water masses exposed to the atmosphere into the ocean interior carries with it natural and anthropogenic carbon dioxide while the re-exposure of older deep water masses to the atmosphere releases respired carbon back to the atmosphere. At the same time, the exchange of water between the surface and deep ocean supplies the interior with oxygen. The rate of transport from the surface to the interior is therefore a key factor controlling the sustainability of life in the ocean, and the exchange of gases with the atmosphere.

Although ocean circulation models are based on sound physical principles, many of their features require parameterization, which can be quite complex. With the ocean being a connected fluid in constant motion, the effects of the parameterizations are difficult to analyze. The starting configuration for a model run may be a good estimate of a pre-industrial steady-state condition, but there is a lack of data with which to constrain the starting conditions, making it is extremely difficult to achieve a model that reflects current conditions in physical and biological tracers.

Running a prognostic model in steady-state with climatological winds to a full equilibrium state involves time-stepping through several thousand model years. Some models in the OCMIP-2 study reported tracer equilibration times of more than 4000 years. (Orr, 2002). For the nominal $1^\circ \times 1^\circ$ horizontal resolution and 60 vertical levels of the Parallel Ocean Program, version 2 (POP2) (Smith et al., 2010), diagnostics such as the ventilation age of water masses or the resident fraction of water ventilated from different regions are expensive to compute with the full dynamical model. We have developed an efficient computational framework based on a steady-state approximation, which we use here to compute the ventilation characteristics of POP2, the ocean component the Community Earth System Model (CESM).

The analysis of when the interior water was last at the surface, ventilation age, and where the interior water was last at the surface can provide some insights into the behavior of the model. In Chapter 2, natural radiocarbon was used as a diagnostic tracer, using the same offline model. The analysis showed that the model ^{14}C age in the North Atlantic was an excellent fit with the observational data, but that Pacific Ocean waters were excessively old. We are looking for more insight into this behavior, and to explore other aspects of the circulation.

We constructed the advection-diffusion transport operator, expressed as a sparse matrix, using a combination of impulse-response functions and explicit coding of the vertical diffusion. The resulting transport matrix is based on the dynamical model which was spun-up from rest for 150 years using the Coordinated Ocean-Ice Reference Experiment (CORE) climatological forcing (Griffies et al., 2009; Large and Yeager, 2009), in which the same seasonal cycle is repeated every model year. Annually averaged values were used for this analysis. Details of the development of the transport operator are given in Chapter 2. The transport matrix, augmented with appropriate boundary conditions for air-sea fluxes, can then be used to compute the equilibrium tracer solutions by direct matrix inversion. This allows the steady-state solution to be determined in a computationally efficient manner.

The transport matrix is used here to analyze the ventilation rate and tracer-transport characteristics of the steady-state circulation of the POP2 model. There are some surprises in the results which follow. Section 3.3 gives a comparison of the ventilation age, with the observationally constrained inverse model calculations of DeVries and Primeau (2011). Section 3.4 examines the ventilation sources for the various ocean regions, and the steady-state distribution of the source waters. Finally, Section 3.5 provides examples of the ventilation age of the ventilation source fractions. The thread through these sections provides a set of methods to provide insight into the characteristics of the circulation.

3.3 Ventilation Age

Ventilation age is defined as the mean length of time since a water parcel was last at the surface, where water masses can exchange gases with the atmosphere. It is also referred to as "Ideal Age" or "Time of Last Passage"(Thiele and Sarmiento, 1990; England, 1995; Primeau, 2005; Primeau and Holzer, 2006; Bryan et al., 2006; Khatiwala, 2007, e.g). It is an idealized tracer, in which all of the interior waters age at the rate of 1 year per year, while water resurfacing has its age reset to zero.

One reason that ventilation age is used in ocean modeling is that it eliminates the variation from the air-sea exchange that is part of most tracers, including ^{14}C. The ventilation age is a measure of only the circulation in the ocean. Waugh et al. (2003) points out that various chemical tracers used to diagnose transit times in the ocean can give different ages, which adds ambiguity to the the results. The differences may result from both boundary conditions and the mixing. The tracer properties affect the "age" calculated, such as the radioactive decay rate for ^{14}C. Thus the term "Ideal Age" because the aging rate is linear with one year per year, regardless of the age. As pointed out by Hall and Haine (2002) different tracers can provide different information about the ventilation characteristics. Various tracer ages that are observable are derived from different weightings over the transport time. "Ideal Age" has the value of being simple to understand, and independent of other ocean tracers. Although the water ventilated in one surface grid-cell has a distribution of ages at which it reaches an interior ocean grid-cell, it is the integrated resulting mean age that is of interest here.

To calculate the age, we start from the standard transport rate equation:

$$\frac{\partial \Gamma}{\partial t} + \mathbf{T}\,\Gamma + S = 0, \tag{3.1}$$

where $\mathbf{T}$ is the tracer transport operator. It is a large sparse square matrix, with the dimensions of the number of ocean grid-cells in the parent model, and populated with the advection-diffusion fields of the circulation. Γ is a vector of the tracer ventilation age in each ocean grid-cell; the variable for which a solution is to be determined. S is the source-sink term, which in this case, has two parts: the aging rate R everywhere of 1 year/year; plus a term for the rebirth at the surface. We use a restoring-to-zero term for the surface layer only, $1/\tau$, where τ was chosen based on the Toggweiler et al. (1989b) time for the mixed layer to be re-exposed at the surface, in this case, 2 years for the 10 m thick surface layer, Δz_1.

$$S_{age} = R - \begin{cases} \Gamma/\tau \text{ if } z < \Delta z_1, \\ \quad 0 \text{ otherwise} \end{cases} \tag{3.2}$$

In the equilibrium solution, the age does not change with time, making $\frac{\partial \Gamma}{\partial t} = 0$, with the resulting equation:

$$\left(\mathbf{T} - \begin{Bmatrix} 1/\tau \text{ if } z < \Delta z_1, \\ 0 \text{ otherwise} \end{Bmatrix}\right)\Gamma = -R \tag{3.3}$$

Figure 3.1 provides the Ventilation Age zonal averages in the Atlantic, Indian, and Pacific ocean basins for the equilibrium solution of the POP2 model. These show generally similar contours to those of the ^{14}C analysis in Chapter 2. While there is no direct way to validate these results with observations, the equilibrium solution for POP2 can be compared with the equilibrium results of the DeVries and Primeau (2011) Inverse Model, where the circulation parameterization has been developed using observational tracers.

In the Atlantic Ocean, both the CESM and Inverse models show the effects of ventilation occurring in the North Atlantic, with the Ventilation Age increasing toward the deep Southern Ocean. The POP2 model shows an age of less than 200 years continuously from 90N to about 40N, indicating a tremendous amount of well-ventilated water in the North Atlantic. The Inverse model shows gradually increasing age in the water with increasing depth in the North Atlantic. For the POP2 model, the maximum Ventilation Age at 60S at the bottom is over 1600 years; for the Inverse model it is about 400 years. However, the Global Ocean Data Analysis Project (GLODAP) ^{14}C data shows aging to around 1200 years at the bottom of the North Atlantic.

In the Indian Ocean, there is general agreement near the surface. With increasing depth, POP2 shows increasingly older, less recently ventilated water, with a maximum in the deep northern end of the basin of 2200 - 2400 years. The

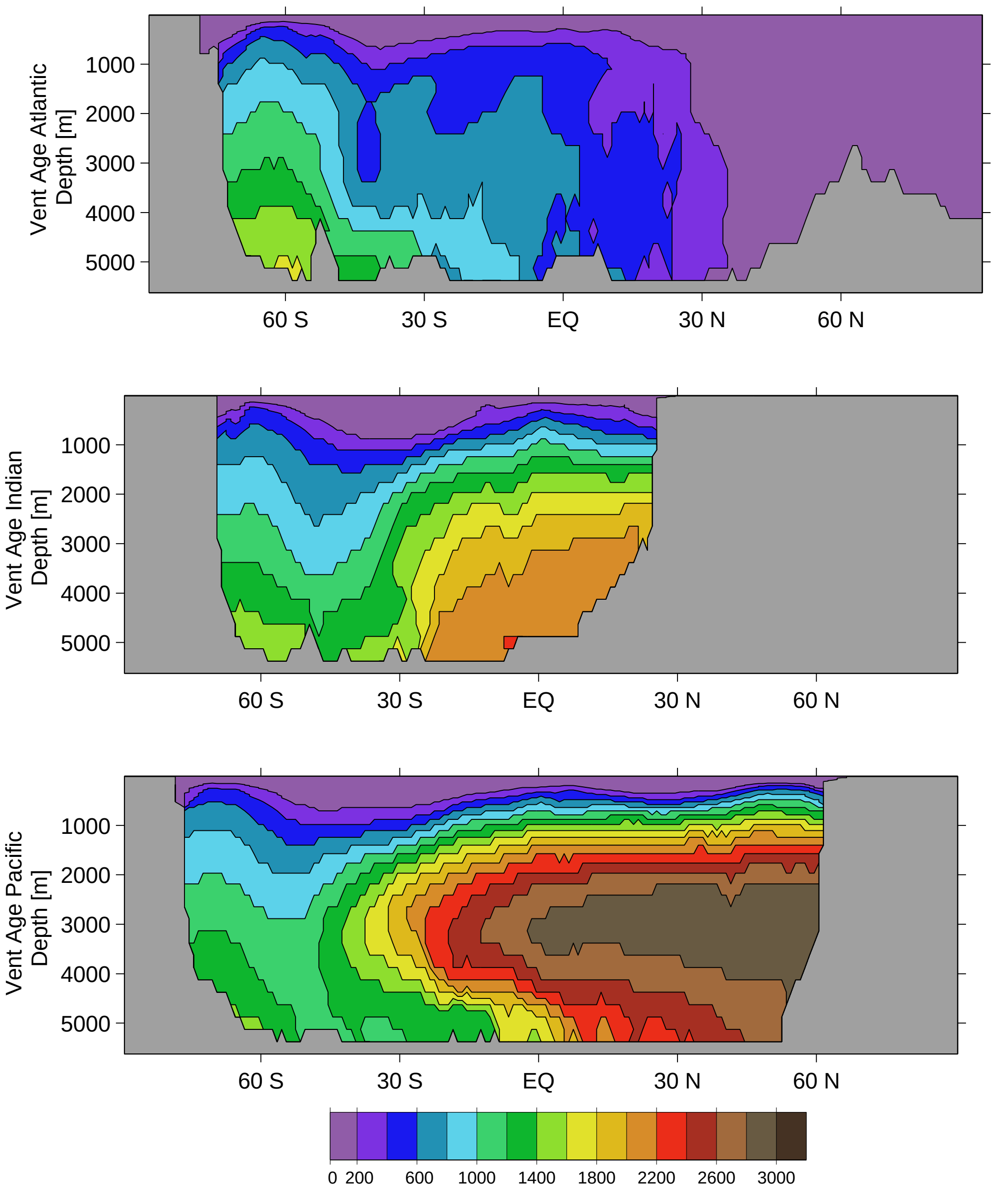

Figure 3.1: Ventilation Age zonal average in the Atlantic, Indian, and Pacific basins.

Inverse model has a maximum of 1200 - 1300 years. The shapes of the contours are similar, which implies that the general circulation patterns are similar. A caution on interpretation, however: in Chapter 2 we found that the Indian Ocean deep water is one of the few places where applying a seasonal cycle compared to the annual average circulation gave a significant difference in ^{14}C age. Using a seasonal cycle resulted in significantly older ages at depths of 500 to 1000 m at the northern end of the basin, and somewhat younger at around 10N in the depth range of 100 to 500 m.

In the Pacific Ocean, while both models show similarly shaped contours, the Ventilation Ages moving toward the North Pacific are remarkably different. The maximum zonal average for POP2 is over 3000 years, compared to just over 1400 years for the Inverse model. Both models show the North Pacific maximum occurring at around 3000 m, while the GLODAP ^{14}C age stays near its maximum of 2200 - 2400 years all the way to the bottom in the area above 30N. The questions that come to mind are: are there differences in the density profile that cause this, or are there unaccounted for effects in the circulation pattern at this end of the basin. This area is particularly interesting because this is the vicinity of the oldest ventilation age water, and also according to DeVries and Primeau (2011) the area of the longest First Passage Time (the mean time for a water parcel at a location in the interior of the ocean to reach the surface for ventilation).

The study of Bryan et al. (2006), which used Ideal Age, pointed out that it is the younger ages that are significant for carbon and nutrient cycles. It is the younger-age locations, either near the surface, or where deep convection takes place, that will see the first response to climate change. Figure 3.2 shows the zonal average for the top 1000 m redrawn with a finer scaling for examination. The Bryan et al. (2006) study, based on CCSM3, showed similar characteristics for the averages

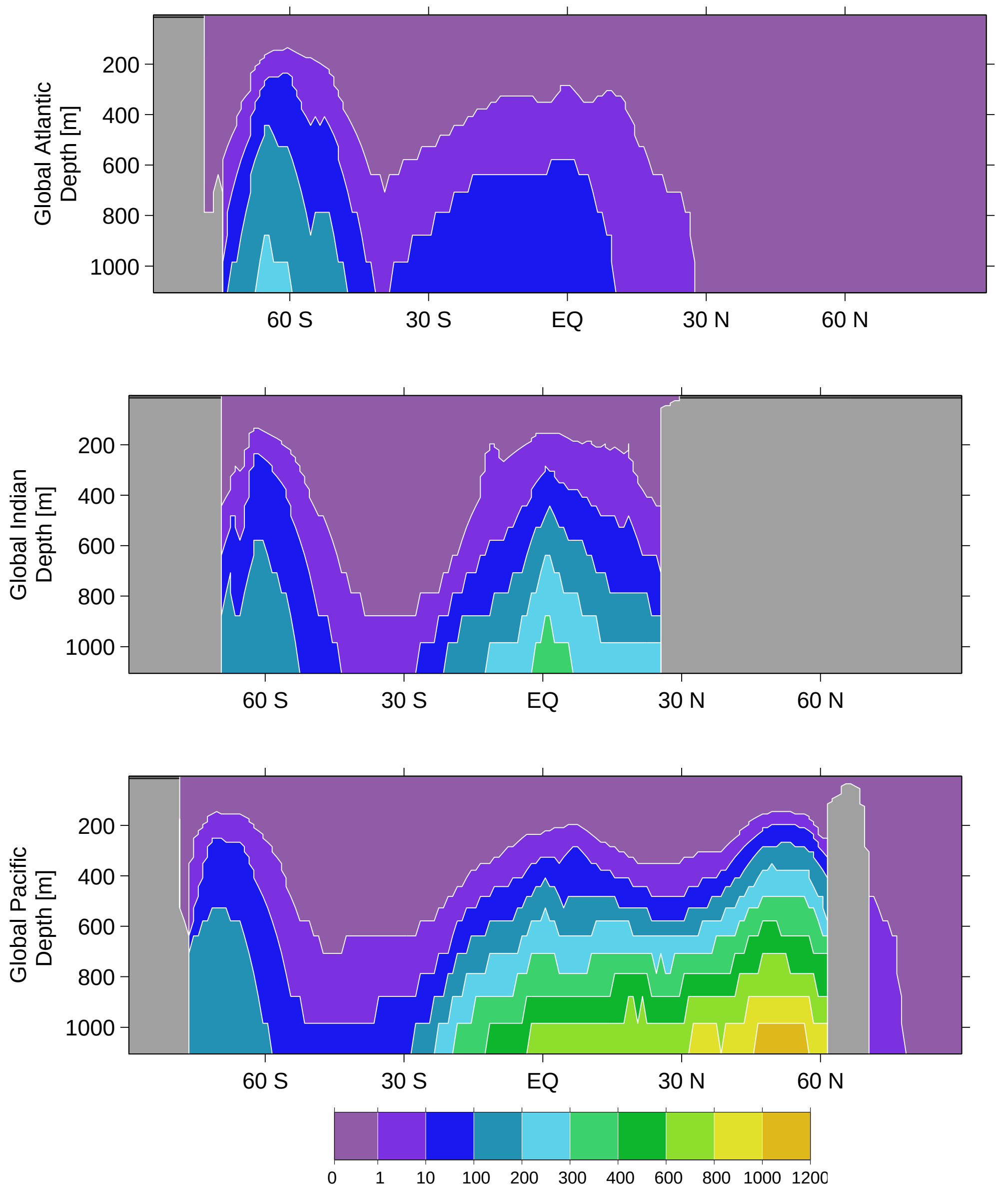

Figure 3.2: Ventilation Age zonal average for the top 1000m, for the Atlantic, Pacific, and Indian Oceans. Each basin has been extended into the Southern Ocean. The contour lines are expanded, so that the contours for 1 year and 10 years are also shown.

from years 1980 to 2000 for the area above 1000m for the Atlantic. In Bryan et al. (2006) Figure 7, the area of deep convection around 60N is conspicuous. For the Indian Ocean, the shapes are similar except that the Bryan et al. (2006) study does not show the peak in age around the equator. For the Pacific Ocean, the contours are similar above 200 m, but the POP2 model ages much more rapidly in the whole basin north of the Southern Ocean.

Comparison of the top 100 m of the Atlantic with the Inverse model of DeVries and Primeau (2011) shows a similar pattern, except that the Southern Ocean is older in the POP2 model below 400 m. Comparing the Indian Ocean top 1000 m, the shapes are the same, but the POP2 model ages faster with depth, to beyond 200 years. This is particularly noticeable around the equator. For the Pacific, the DeVries and Primeau (2011) Inverse model approaches 1000 years by a depth of 1000 m, while the POP2 model reaches that age before 600 m. All three cross-sections show a difference in the ages in the Southern Ocean, with a strip of youthful water around 60S in the DeVries and Primeau (2011) Inverse model that is not seen in the POP2 model.

The extremely high Ventilation Age for POP2 in the North Pacific could be due to sluggish circulation in the Pacific in the POP2 model, insufficient proportion of Southern Ocean water incorporated into the Pacific Ocean, or insufficient water formation in the Southern Ocean. Further analysis provides clues.

3.4 Ventilation Fractions

Both comparison of POP2 ^{14}C age with observational ^{14}C age, and comparison of POP2 ventilation age with that of the Inverse Model, show a substantially older age in the deep North Pacific for POP2. The cause of the older age may be possible to analyze by combining the information from the age diagnostics with the fractions of ventilated water from various ocean regions that is resident in the Pacific. The age depends partly on the relative proportions of the North Atlantic and Southern Ocean ventilated waters that are incorporated into the Pacific, in addition to the circulation rates within the Pacific Ocean. As pointed out by Haine and Hall (2002), it is both the age and the distribution of the water from its ventilation source that gives us insight into the characteristics of the circulation. Here we examine the fractions analyzed in the POP2 model: first, with respect to the latitude at which ventilation occurs; and second, with respect to where the water ventilated in a particular region of the ocean ends up residing in the interior of the global ocean.

To calculate the ventilation fractions stemming from each region, we start with the standard transport rate equation, Equation 3.1, but this time we want to solve for f_r, the fraction of the water last ventilated at the surface of the selected ventilation region, instead of Γ. The source term, S, is $1'$s in the source region and $0'$s everywhere else:

$$S_{frac} = \begin{cases} 1 \text{ if } (z < \Delta z_1, \& \in \text{ventilation region}), \\ 0 \text{ otherwise} \end{cases} \tag{3.4}$$

The resulting equilibrium solution for the ventilation fraction is:

$$\mathbf{T} f_r = -S_{frac} \tag{3.5}$$

Only the right-hand-side of Equation 3.5 changes for a different ventilation region. This means that the transport operator, $\mathbf{T}$, only needs to be inverted one time to allow solving for the source fractions from multiple regions.

The regional definitions of the POP2 model were used as a basis for this analysis, but with some of the smaller regions defined in the POP2 model combined into

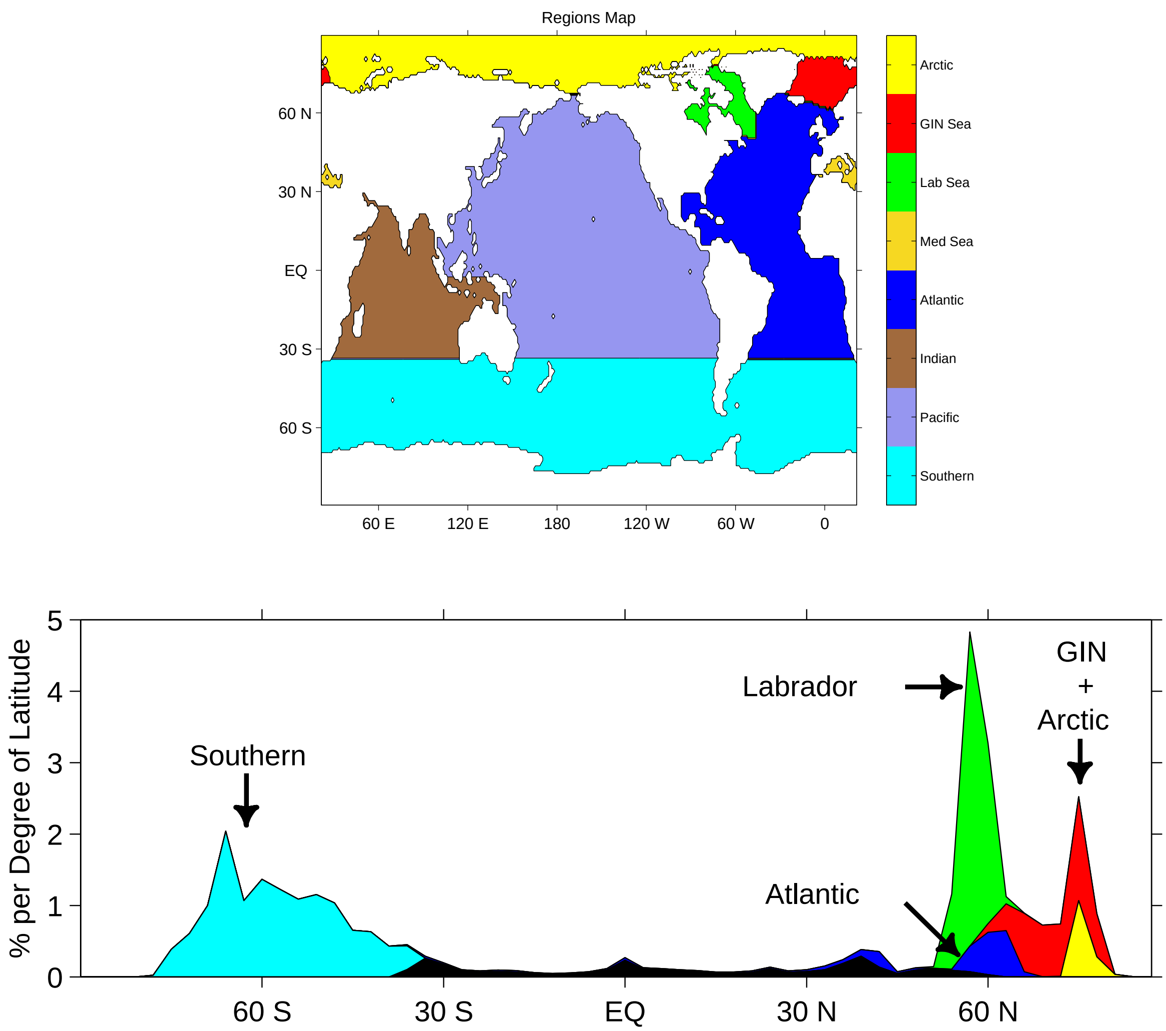

Figure 3.3: The top panel shows the ocean regions, derived from POP2 model definitions. The bottom panel illustrates the percent of the ventilation source waters per degree of latitude. The peaks of major source regions are annotated.

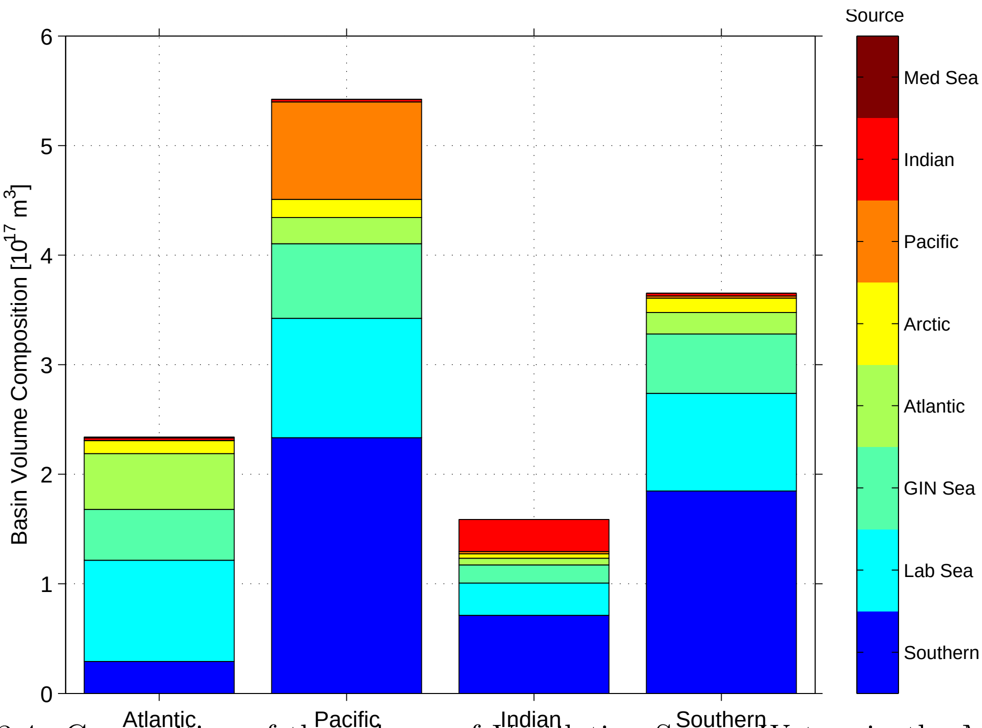

Figure 3.4: Composition of the volume of Ventilation Source Waters in the Major Ocean Basins. Each bar shows the composition of the ventilation source water for the indicated basin.

larger ones. Thus the Persian Gulf is incorporated into the Indian Ocean, and the Hudson Bay is incorporated into the Labrador Sea. Marginal seas that in the POP2 model are not connected to the global ocean have been eliminated. The resulting ocean region definitions are illustrated in the top panel of Figure 3.3.

The bottom panel in Figure 3.3 shows the percent of the ventilation source waters per degree of latitude. That is, the latitude at which the water anywhere in the interior of the global ocean last made contact with the atmosphere. The major source regions are annotated on the figure. The Labrador Sea stands out compared to either the Greenland-Iceland-Norwegian (GIN) Sea or the Southern Ocean.

For each of the major basins, the total percent of ventilation-source water from each region are presented in Figure 3.4. The "North Atlantic" as used here is defined as the sum of the Labrador Sea, the GIN sea, the Arctic, and the Atlantic

FROM SOURCE BASI TO	Pacific	Indian	Mediterranian	Arctic	Atlantic	GIN	Labrador	Southern
Southern	45.0	13.7	0.0	0.0	5.6	0.0	0.0	35.6
Labrador	33.8	9.1	0.0	0.0	28.7	0.0	0.8	27.6
GIN	35.4	8.6	0.0	2.0	24.1	1.4	0.2	28.2
Atlantic	23.8	6.1	0.0	0.0	50.6	0.0	0.2	19.3
Arctic	29.5	7.2	0.0	16.2	21.0	2.4	0.2	23.5
Mediterranian	2.6	1.0	76.2	0.0	17.7	0.0	0.0	2.4
Indian	6.1	80.3	0.0	0.0	6.6	0.0	0.0	6.9
Pacific	95.5	2.2	0.0	0.0	0.2	0.0	0.0	2.1

Table 3.1: For each ocean region, the percent of ventilation source waters that ends up in various basins. For example, 45% of the water which ventilated in the Southern Ocean ended up in the Pacific Ocean.

regions. In the Pacific Ocean, 43% is from Southern Ocean ventilated water, and 40% from the North Atlantic. In the Indian Ocean, 45% is from the Southern Ocean, and 35% from the North Atlantic. The Southern Ocean itself has only 51% of its waters ventilated there, with 48% from the North Atlantic.

Table 3.1 summarizes for the source waters that ventilate in a given region, the resultant percent of the ventilated water that ends up in each region's interior. The Pacific and Indian Oceans can be characterized as "ventilation receiver" oceans, with over 80% of the waters that ventilate in those oceans staying there, but receiving substantial ventilation fractions from the Southern, Labrador, Atlantic, and GIN. The Labrador Sea, on the other hand, disperses almost all of its ventilated water to the other oceans, with 45% ending up residing in the Southern Ocean.

The POP2 model has 51% of global ocean water ventilated from the North Atlantic, and 39% ventilated in the Southern Ocean. A similar analysis of the Inverse model of DeVries and Primeau (2011) shows more than 75% of water ventilated from the Southern Hemisphere. This difference may explain the difference in the radiocarbon ages and ventilation ages. Recall that the ages in the North Pacific, especially, were much older in the POP2 model than the Inverse model or the GLODAP data. That is, the ages seen in the North Pacific in the POP2 model may result from a lower proportion of the water in the Pacific coming from water which ventilated in the Southern Ocean. A higher proportion from the North Atlantic would make the age older since it had further to travel.

Gebbie and Huybers (2010) explored the steady-state model result of surface-ventilating waters to its interior distribution. Their approach was to use a pathways model, based on the inter-connectivities of the ocean grid boxes, and not explicitly on the rates at which the water is carried. Their method used observational data on 6 conserved (or semi-conserved) tracers to determine the parameters of their model. Their results were that 56% of the global ocean was ventilated in the Antarctic and Subantarctic. Only 25% of the water in the deep North Pacific was ventilated in the North Atlantic.

Reid (2005) traced the North Atlantic Deep Water (NADW) into the Antarctic Circumpolar Current (ACC) using isopycnals. Silica and oxygen were used as tracers. He observed that the NADW characteristics were so strong that it could be traced completely around the ACC and even back into the Atlantic in addition to the Pacific and Indian Oceans.

Johnson (2008) studied the contribution of NADW and Antarctic Bottom Water (AABW) to the ocean basins and the global ocean, using quasi-conservative seawater properties. He found that AABW contributes roughly twice the volume of NADW in the three major ocean basins. Sensitivity analysis, especially with regard to the exact choice of source water mass, gave the estimate that the ratio was at least 1 but no more than 3. Although these study results cannot be compared directly with the current study, they do give clues about the differences seen. The AABW definition was based on the seawater properties, first of water from the Weddell Sea Bottom Water, which has the most extreme characteristics; and second, as part of the sensitivity study, using water with the properties of Adelie Land Bottom Water, which are less extreme. The properties of the water that was found already on the bottom were then traced back; this excluded Antarctic Intermediate Waters. According to the POP2 model, the water at the bottom of the Antarctic basin (at around 60S) is composed of 0.3 to 0.4 Labrador Sea water, 0.2 to 0.3 GIN Sea and only 0.2 to 0.3 Southern Ocean ventilated water. So, the fact that the Weddell Sea sill overflow was unproductive in the POP2 model results may have strongly influenced the amount of Antarctic Bottom Water that was formed.

Let us examine in more detail how the major source regions contribute to these basin totals and is distributed.

3.4.1 Southern Ocean

Figure 3.5 shows the steady-state average fraction of water that had its ventilation-source in the Southern Ocean. This is a zonal average. The extensions of the Southern Ocean into the Atlantic, Indian, and Pacific Oceans are shown. The intrusion of the Southern Ocean source waters into the Atlantic peaks between 1000 and 2000 m, with a very low fraction, less than 0.1, at depths below 3000 m. This matches what is expected for Antarctic Intermediate Waters (AAIW). On the other hand, in the the Indian and Pacific Oceans, the Southern Ocean ventilated water intrudes further north, such that it is present with fractions exceeding 0.5 all the way to the north end of those oceans. The largest fractions are at 2000 to 4000 m in the Pacific, but extend below 4000 m in the Indian Ocean.

There is also a decrease in the fraction of Southern Ocean ventilated water with depth in the Southern Ocean itself, to less than 0.20. Antarctic Bottom Water intrusion into the Atlantic is not apparent. It is to be noted that although the sill overflow parameterization was turned on during the model run, there was no sill overflow production in the Southern Ocean for either the Ross Sea or the

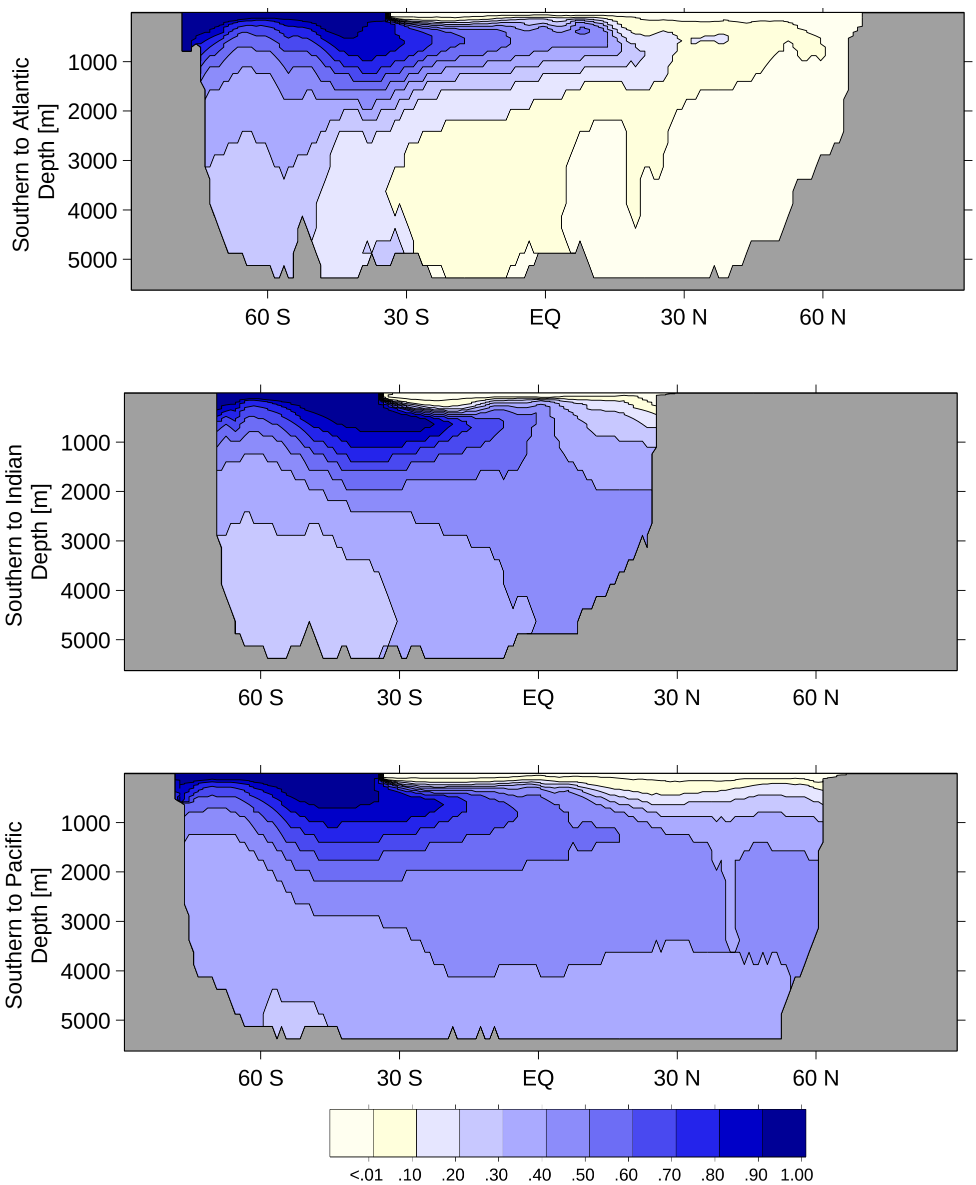

Figure 3.5: Southern Ocean Ventilation Fraction Zonal Averages in Various Basins. The zonal averages in the Southern Ocean were computed by extending the boundaries of the Atlantic, Indian, and Pacific Oceans into the Southern Ocean. The blip in the Pacific Ocean at 40 N is caused by the Sea of Japan, which is self-ventilating, being included in the zonal average.

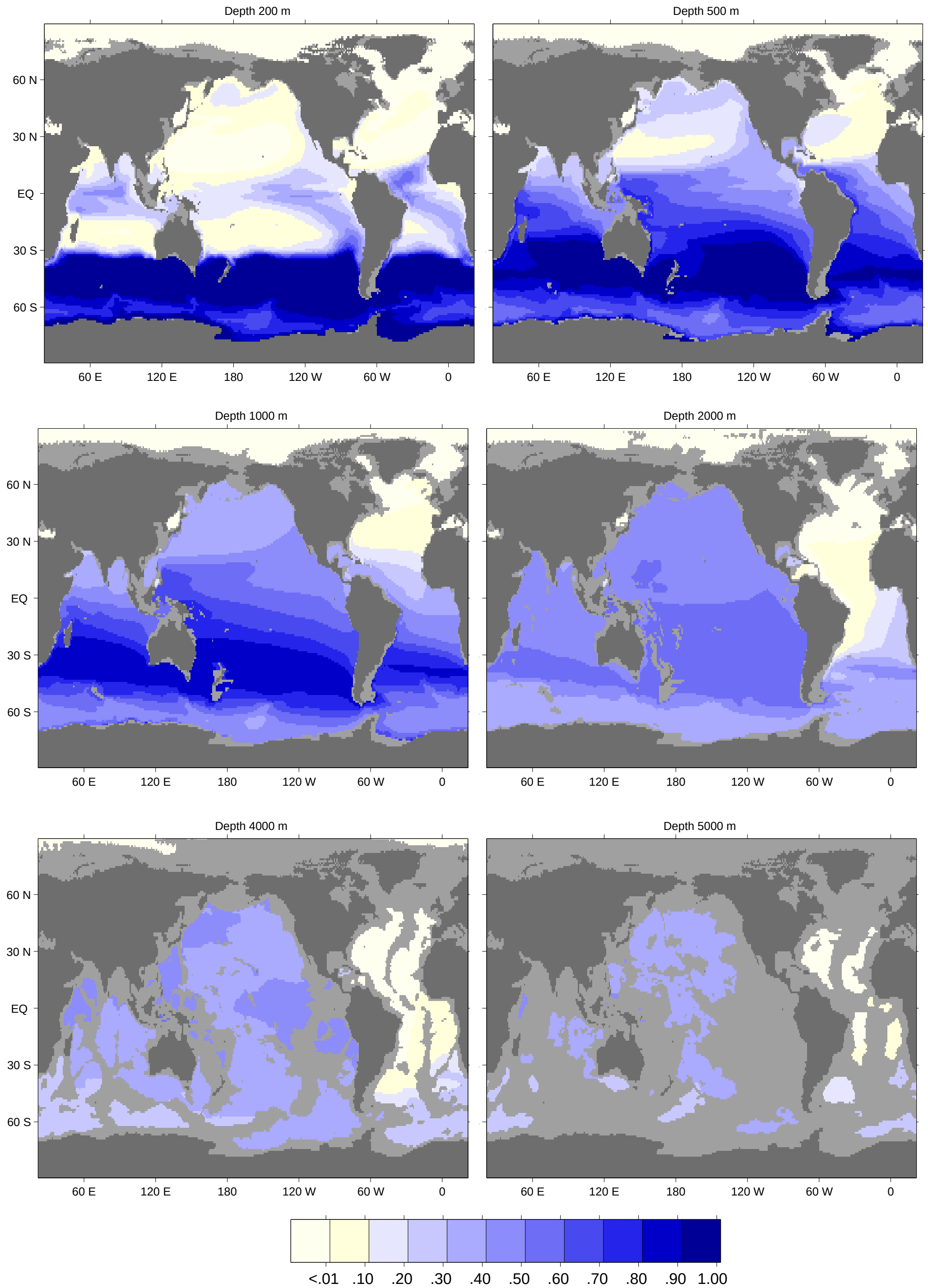

Figure 3.6: Southern Ocean Ventilation Fraction at various depths.

Weddell Sea. By contrast, the sill overflow production is readily visible in the North Atlantic.

Figure 3.6 shows a horizontal view of the Southern Ocean ventilation fraction at various depths. In all three basins, the Southern Ocean waters extend northward along the western boundaries of the basins at 1000 m. The Southern Ocean fraction is greater than 0.5 all the way to the equator in the Western Pacific. This is quite visible even at depths as shallow as 500 m. At 4000 m, there are a few pools of 0.3 to 0.4 fraction in both the Pacific and Indian basins, but the Atlantic fraction is nil. The largest intrusion into the Atlantic is at 500 m.

So, if the fraction of Southern Ocean ventilated water at depths of 4000 m and below in the Pacific and Indian Oceans is less than 0.4, where does the rest of that water come from?

3.4.2 Labrador Sea.

The Labrador Sea water travels. Figure 3.7 contains zonal average cross-sections of the fraction of water that had its ventilation-source in the Labrador Sea for the Atlantic, Indian, and Pacific basins. The extension of the Labrador Sea into the Atlantic, and beyond into the Southern Ocean is shown in the top panel. But the destination of the Labrador Sea waters does not stop there. Consider that it mixes in the lower part of the Southern Ocean, and then continues onward in the depths of the Indian and Pacific Oceans, where the fraction contributed is between 0.3 and 0.4 in the bottom layers, as shown in the lower two two panels of Figure 3.7. At intermediate depths there is still a substantial fraction, 0.1 to 0.3. Fully a third of the waters ventilated in the Labrador Sea end up in the Pacific Ocean, and over a quarter in the Southern Ocean (refer to Table3.1).

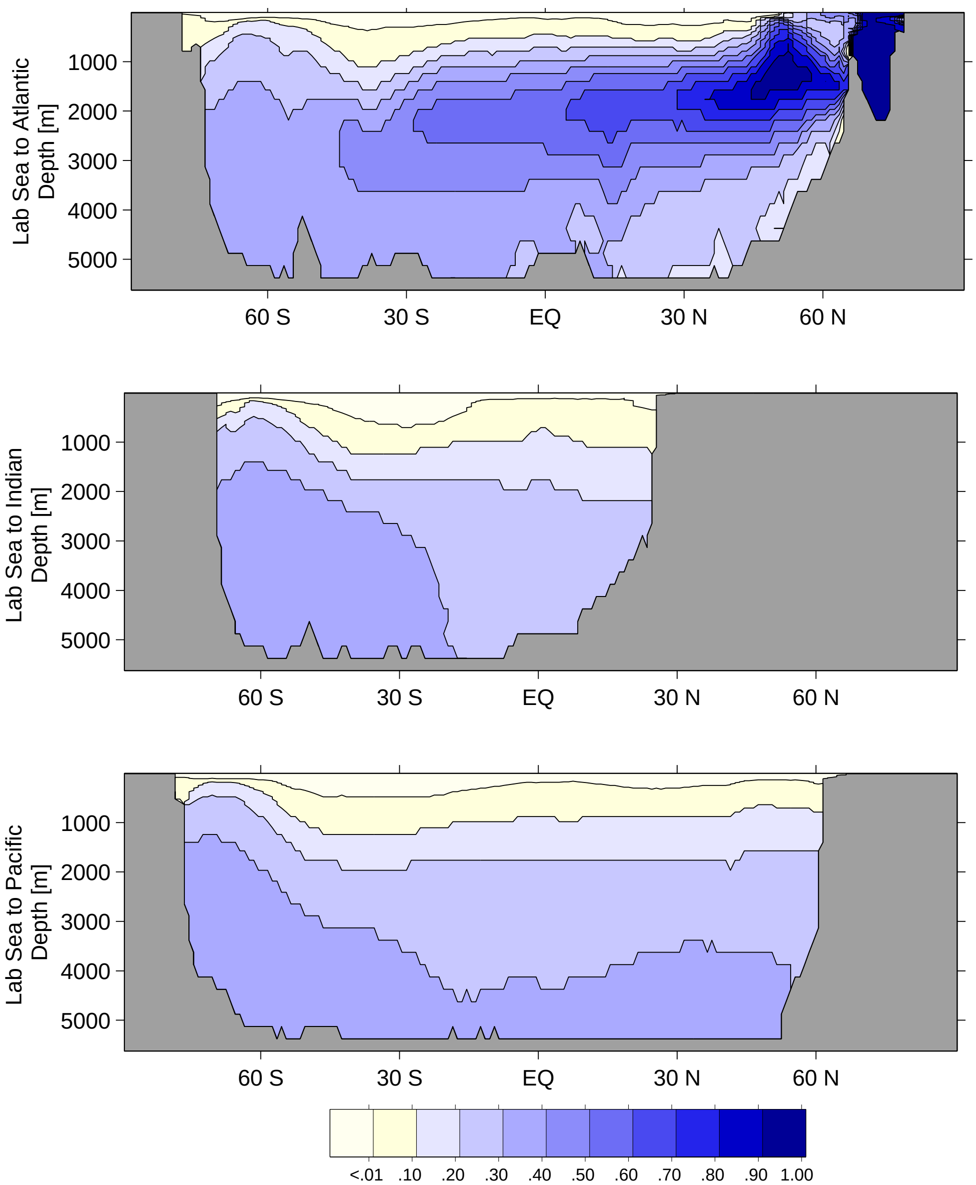

Figure 3.7: Labrador Sea Ventilation Fraction Zonal Averages in Various Basins. The zonal averages in the Southern Ocean were computed by extending the boundaries of the Atlantic, Indian, and Pacific Oceans into the Southern Ocean.

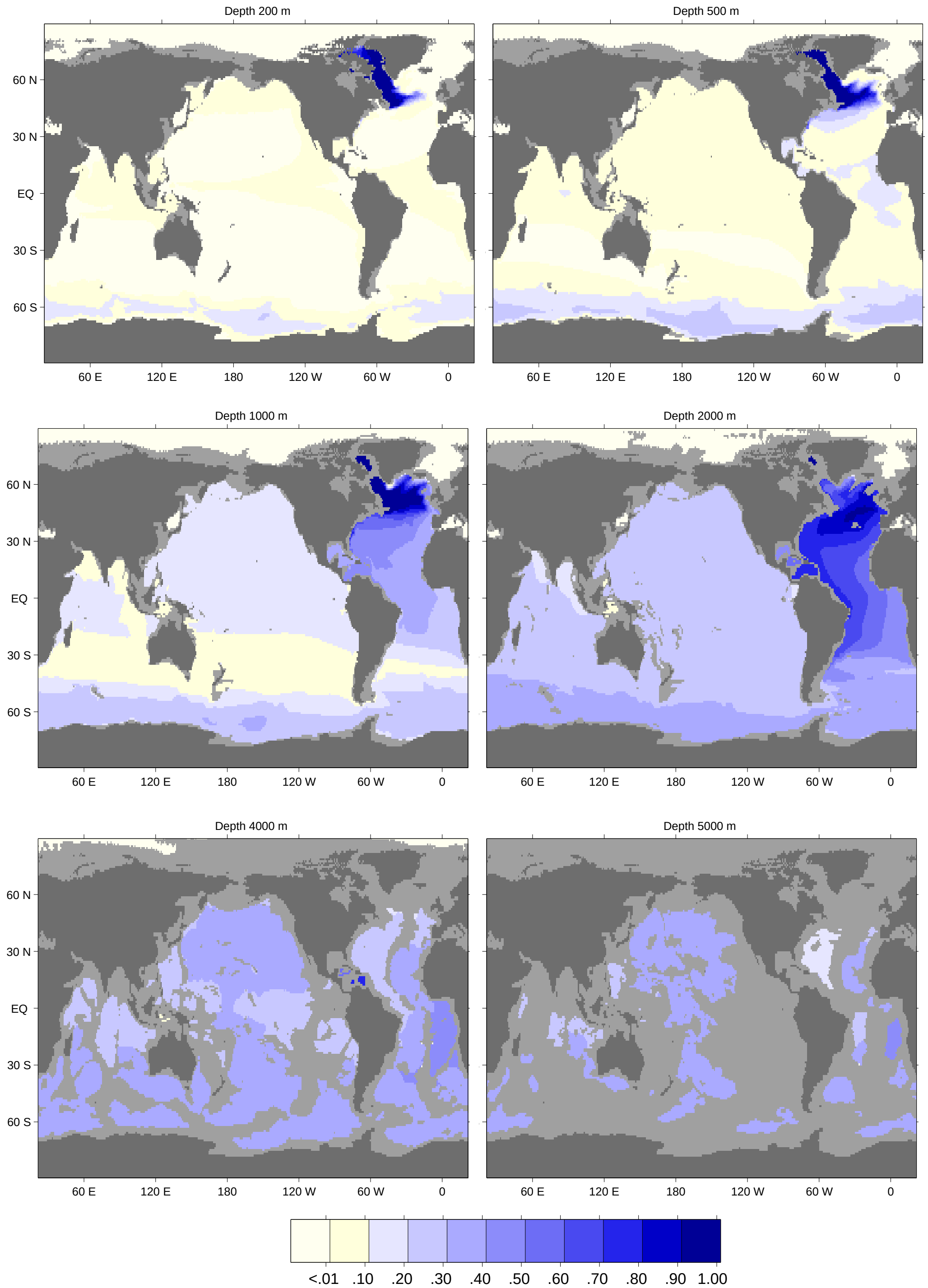

Figure 3.8: Labrador Sea Ventilation Fraction at various depths.

The major flow into the Atlantic is at around 2000 m, with a peak at around 3000 m all the way to the Southern Ocean. It sinks coming out of the Southern Ocean into the Indian and Pacific basins. Only the flow southward from the Labrador Sea is shown on the cross-sections; the flow into the Arctic is tiny, and not shown. It is to be noted that, in the model, Nares Straight is the only direct path through the Canadian Archipelago into the Arctic. Landcaster Sound, for example, does not connect the two.

Figure 3.8 examines the Labrador Sea ventilation fraction at various depths. This tiny sea, at a depth of 2000 m is supplying the majority of the ventilated water to the whole Atlantic Ocean. The presence is especially high along the western boundary of the basin. At a depth of 4000 m it is supplying 0.3 to 0.5 of the water. Remarkable.

3.4.3 GIN Sea

Figure 3.9 is a zonal average of the fraction of water that had its ventilation-source in the GIN Sea. The top panel illustrates the extension of the GIN Sea into the Atlantic, and on into the Southern Ocean. Similar to the Labrador Sea, the GIN Sea waters mix into the Southern Ocean and mix into the bottom reaches of the Indian and Pacific basins. As shown in the bottom two panels of Figure 3.9, the fraction contributed is up to 0.2. However, compared to the Labrador Sea, The GIN sea waters do not continue to have as strong a presence in the bottom of the northern end of the Pacific.

Note also, in the GIN Sea to Atlantic panel, the strong flow towards the bottom along the northern end of the Atlantic basin. This is likely due to the sill overflow, which has been parameterized in POP2 for both the Faroe Bank Channel and the Denmark Strait. Unlike the Labrador Sea inputs, the GIN Sea waters have their

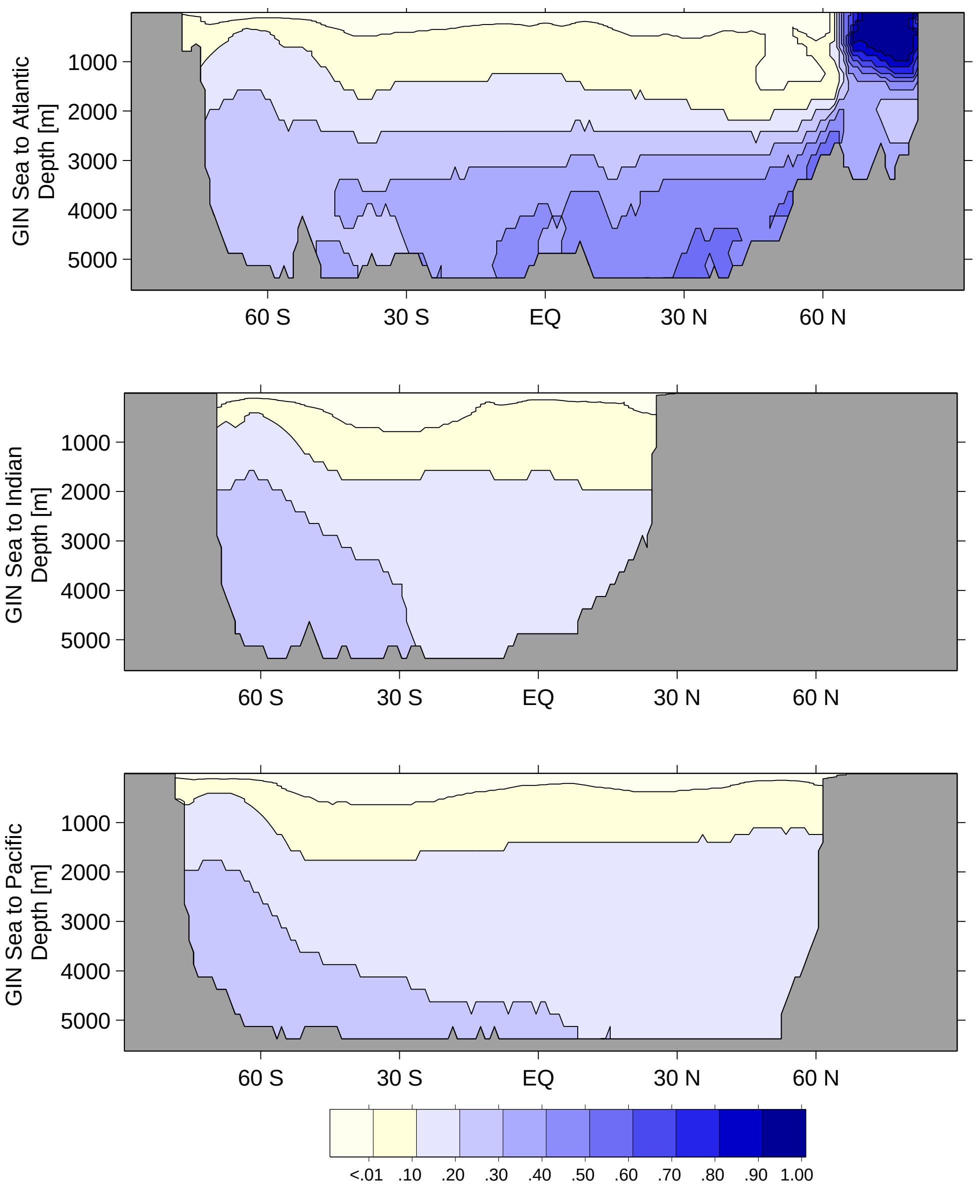

Figure 3.9: GIN Sea Ventilation Fraction Zonal Averages in Various Basins. The zonal averages in the Southern Ocean were computed by extending the boundaries of the Atlantic, Indian, and Pacific Oceans into the Southern Ocean.

largest fraction along the bottom of the basin. The flow from the GIN Sea to the Arctic is not shown in the zonal average because of the overlapping latitudes. In the Arctic, at 500 m, there is some GIN-ventilated waters along the coast east of the GIN Sea. There is also a substantial fraction of GIN waters at depths of 4000 and 5000 m (not shown).

Comparing Figure 3.9 with Figure 3.7, it can be seen that the water from the GIN Sea prevails along the bottom of the Atlantic, with the Labrador Sea waters above. This is in agreement with observations (Talley and McCartney, 1982). The combined GIN and Labrador waters have been traced to the Antarctic Circumpolar Current and beyond into the Pacific and Indian Oceans (Reid and Lynn, 1971), and this is in agreement with the CESM ocean model.

3.4.4 Major Basins

In Figure 3.10, the top panel shows the zonal average for water ventilated in the Atlantic Ocean, with extensions into the Arctic and Southern Ocean. The Atlantic-ventilated water is not the major component in its own basin below 1500 m.The hole at mid-depths is filled primarily by the Labrador Sea and the GIN Sea waters. Only north of the equator is the downward diffusion seen; the Atlantic surface ventilation stays very shallow in the whole South Atlantic. Even though 24% of Atlantic-ventilated water ends up residing in the Pacific, the volume of the Pacific is so large, and the volume ventilated in the Atlantic is so small, that the concentration in the Pacific is less than 0.1 everywhere (not shown). This is also true for the fractions that reside in the Southern Ocean, and in the Indian Ocean.

If we add all the contributors to the North Atlantic regions together (the Labrador Sea, the GIN sea, the Arctic and the Atlantic) then we get a different picture.

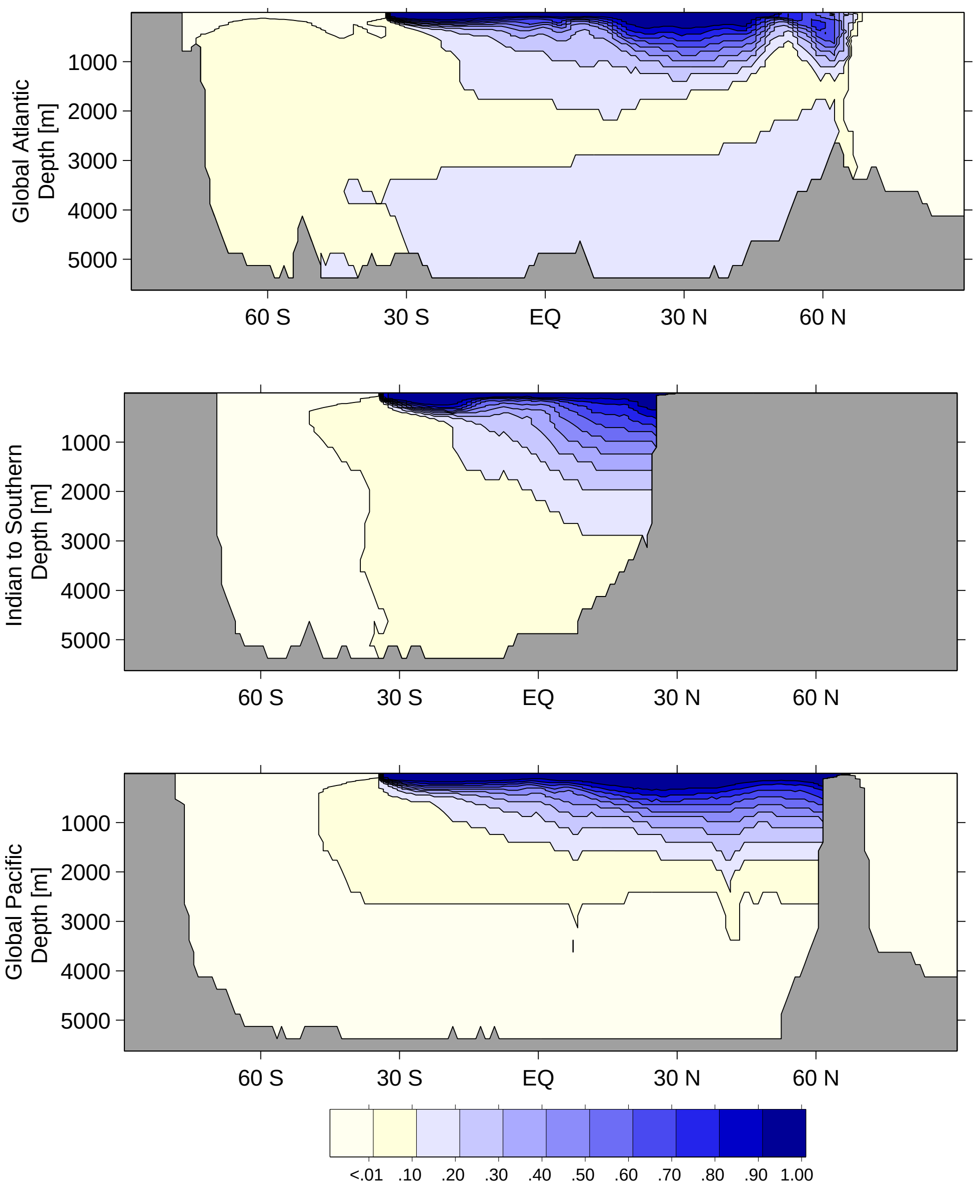

Figure 3.10: Atlantic, Indian, and Pacific Ocean Ventilation Fraction Zonal Average Cross-sections. Extensions into the Southern Ocean and the Arctic are also shown. In the Pacific basin, the blip at around 40 N, is caused by the Sea of Japan being included in the zonal average. As can be seen here, the major ventilation sources for these basins are outside of the basins themselves.

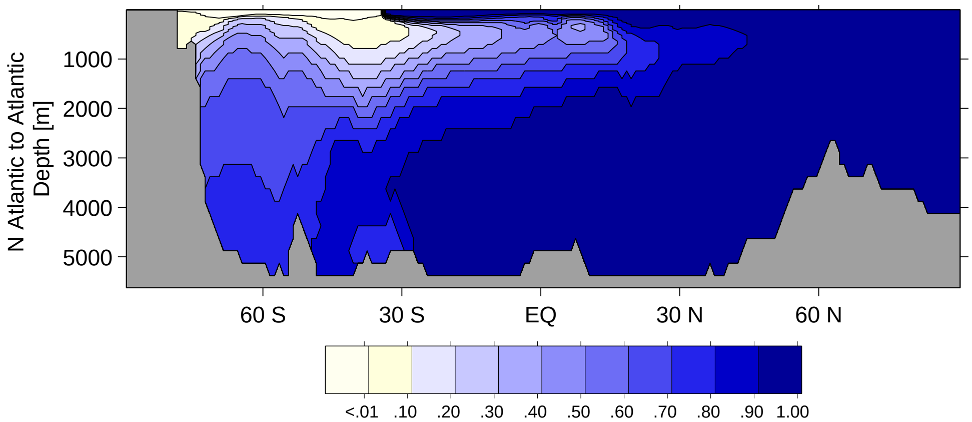

Figure 3.11: Total North Atlantic Ocean Ventilation Fraction Zonal Average. Note that the sum from the Labrador Sea, GIN Sea, the Arctic, and the Atlantic form a reverse pattern to the waters ventilated in the Southern Ocean.

Figure 3.11 shows a zonal average for the sum of these regions. Now we see that the Atlantic is completely supplied by the sum of these regions, except for a hole for ventilation from the Southern Ocean. Even the bottom of the Southern Ocean is 0.7 to 0.9 composed of water that was ventilated in the North Atlantic. Compare this with the ventilation from the Southern Ocean in Figure 3.5. It fits neatly into the hole in the North Atlantic ventilated water.

95% of the water ventilated in the Pacific remains there, with only small percentages in the Southern and Indian Oceans. In Figure 3.10, the bottom panel shows the zonal averages in the Pacific for waters ventilated there. It is clear that the water ventilating there does not travel very far; the depths below 1000m must be ventilated from other sources. The maximum depth of a fraction greater than 0.9 is around latitude 30N . It does not drop as far in the South Pacific gyre where there is a strong influence from the Southern Ocean. The dip in the contours near 40N is caused by the Sea of Japan, which is included in the Pacific Ocean zonal average. The Sea of Japan shows a fraction of greater than 0.9 all the way from the surface to the bottom below 3000 m.

The bottom panel of Figure 3.5 shows the water ventilating in the Southern Ocean that flows into the Pacific, peaking at intermediate depth. This fits together with the Pacific-ventilated fraction at intermediate depths. There is no significant Pacific-ventilated water in the Arctic. The fraction drops to below 0.1 in the Bering Straight, which is very shallow.

In Figure 3.10, the middle panel gives the zonal average for water ventilated in the Indian Ocean. The situation is similar to that seen in the Pacific, except that the surface ventilated water penetrates more deeply at the northern end of the basin. At 500 m, the resident fraction is high at the northern end of the basin, but quickly gets lower toward the south. This is consistent with the view from the Southern Ocean source waters, which can be seen to push northwards at that depth.

80% of the volume ventilated in the Indian Ocean remains in the Indian Ocean, with around 6% each ending up in the Pacific, Southern, and Atlantic oceans. Why are these external fractions higher from the Indian Ocean than for the Pacific? The Indian Ocean basin is much shorter than the Pacific, and it has a large interface with the Southern Ocean. The fraction in the Atlantic is carried to the external basins via the Southern Ocean. Layer views (not shown) show some water escaping the Indian basin via the Agulhas Current, around the tip of Africa. In the easterly direction, there is some water disappearing in the Indonesian Throughflow, which is considered as part of the Pacific region in the CESM model. It quickly becomes too diffuse to track any further into the Pacific.

3.5 Age of a Source Fraction

The age of each fraction was computed by the method derived in Primeau (2005), which provides a way to calculate the age of each fraction once the fractions are

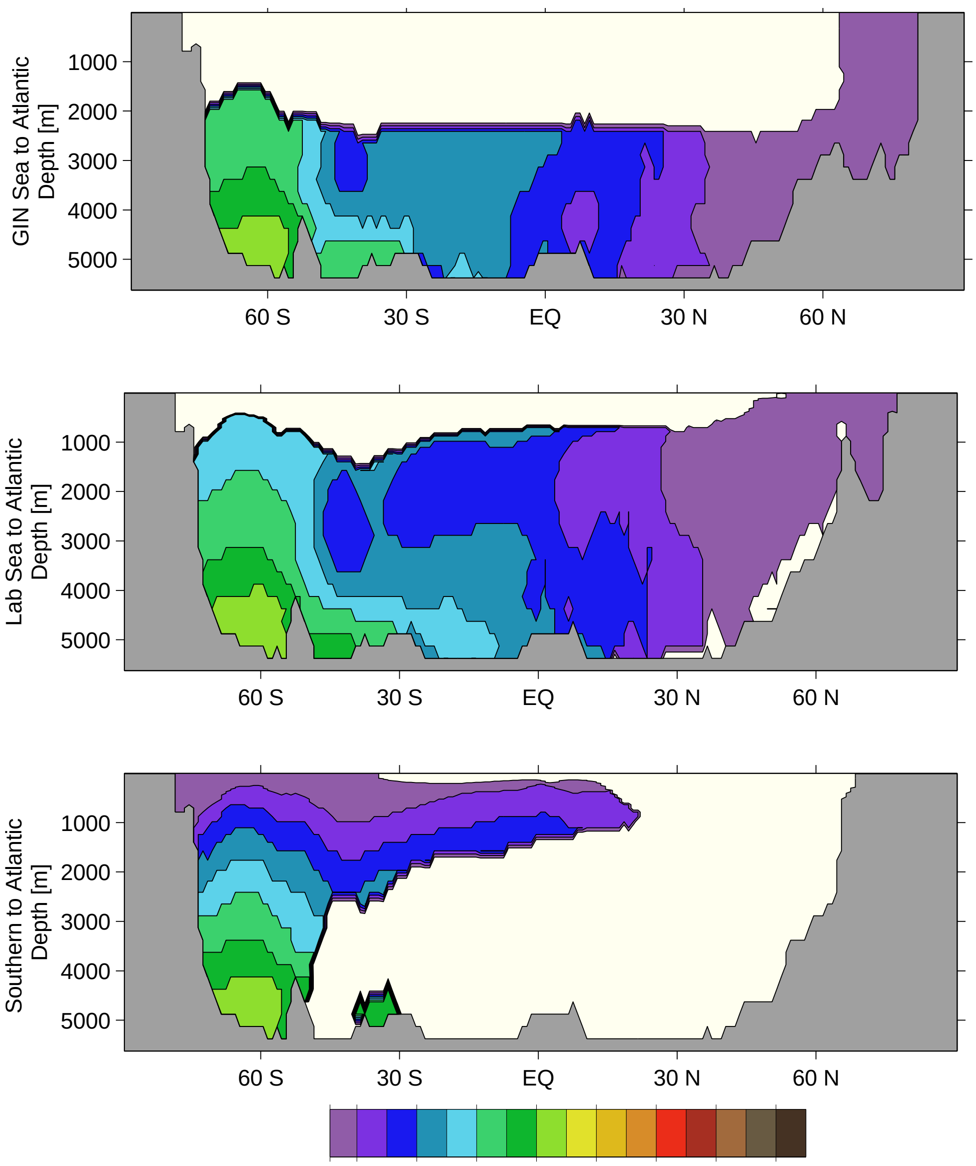

Figure 3.12: Ventilation age zonal average for the Atlantic basin, sourced from the GIN Sea, Labrador Sea, and Southern Ocean. The age is shown where the contributing fraction is greater than 0.20

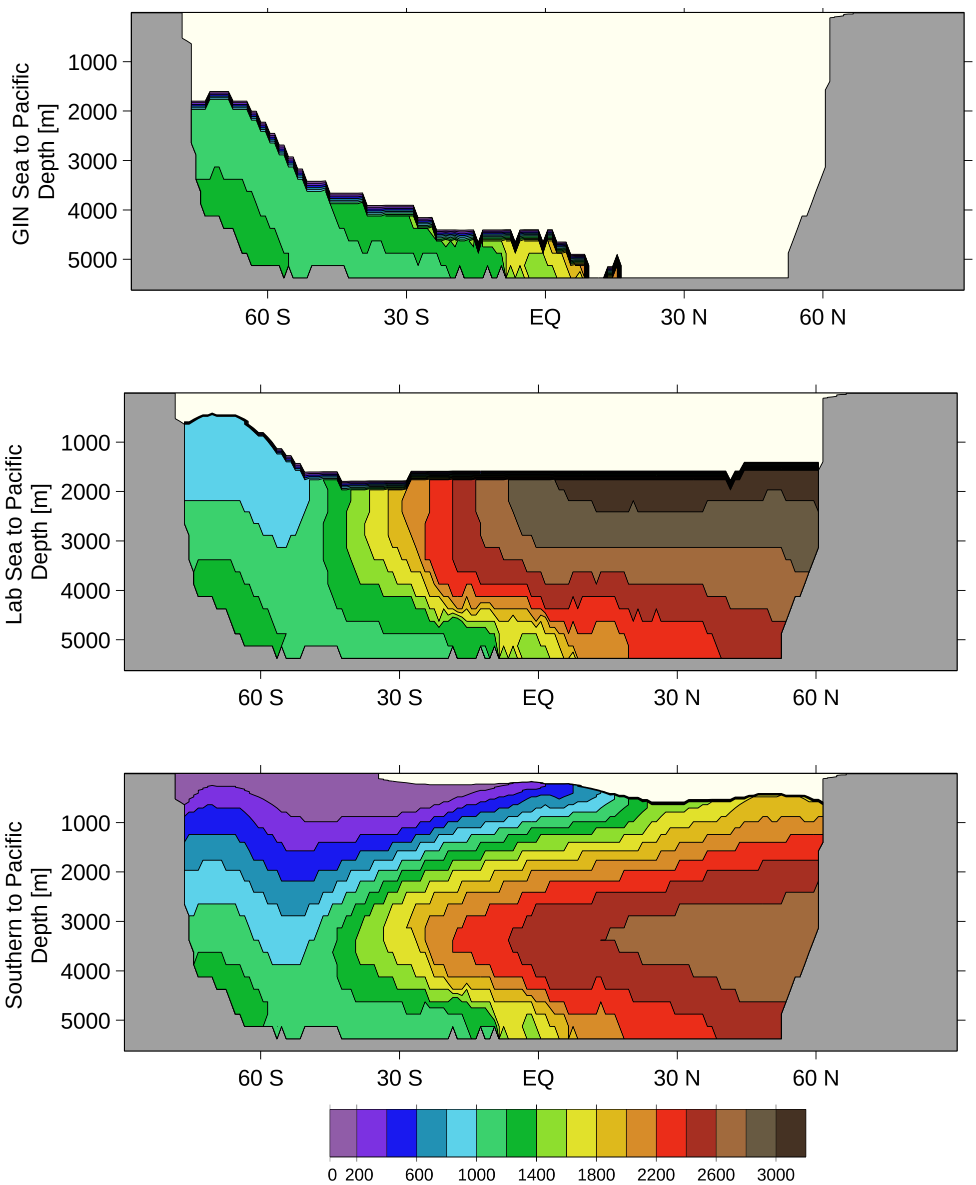

Figure 3.13: Ventilation age zonal average for the Pacific basin, sourced from the GIN Sea, Labrador Sea and the Southern Ocean. The age is shown where the contributing fraction is greater than 0.20.

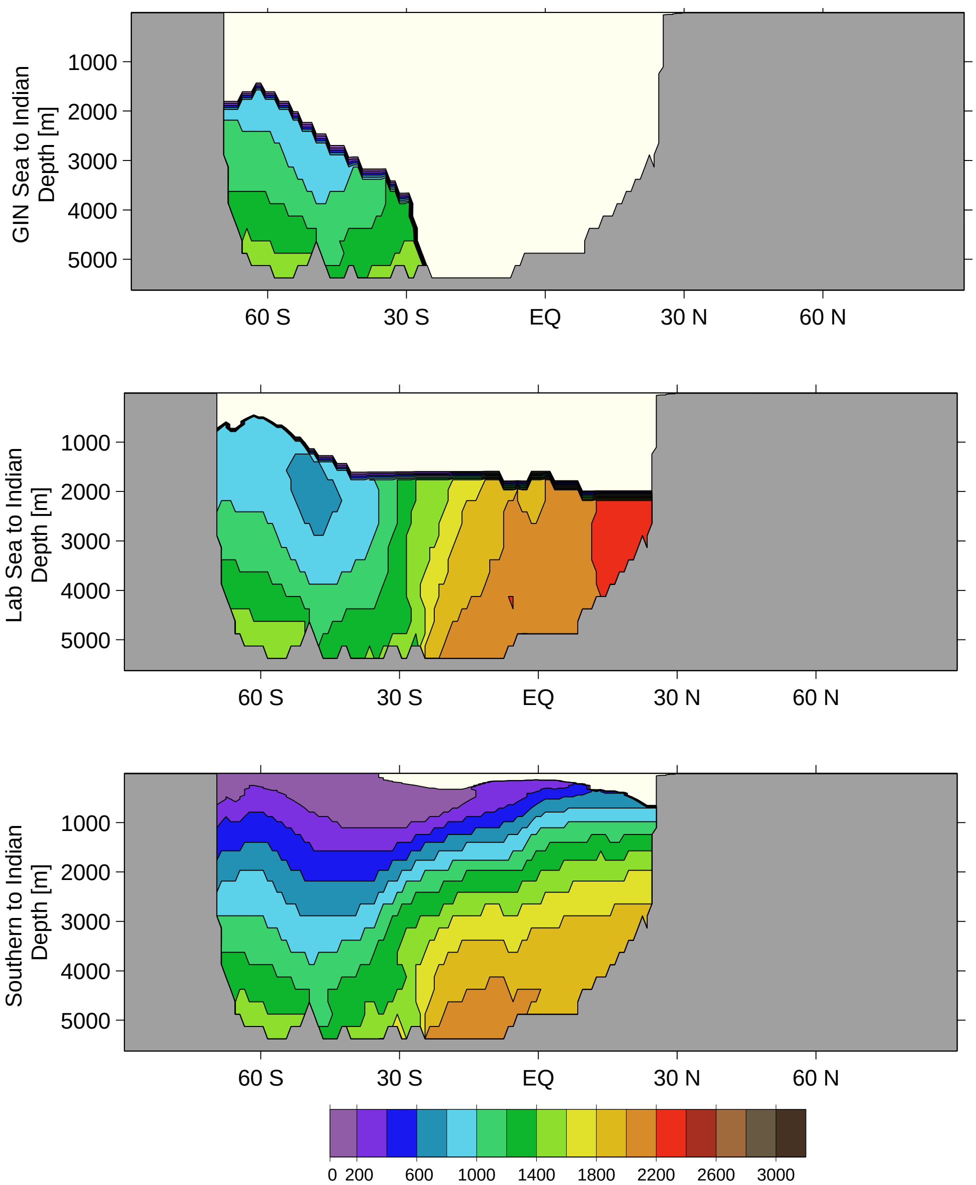

Figure 3.14: Ventilation age zonal average for the Indian basin, sourced from the GIN Sea, Labrador Sea and the Southern Ocean. The age is shown where the contributing fraction is greater than 0.20.

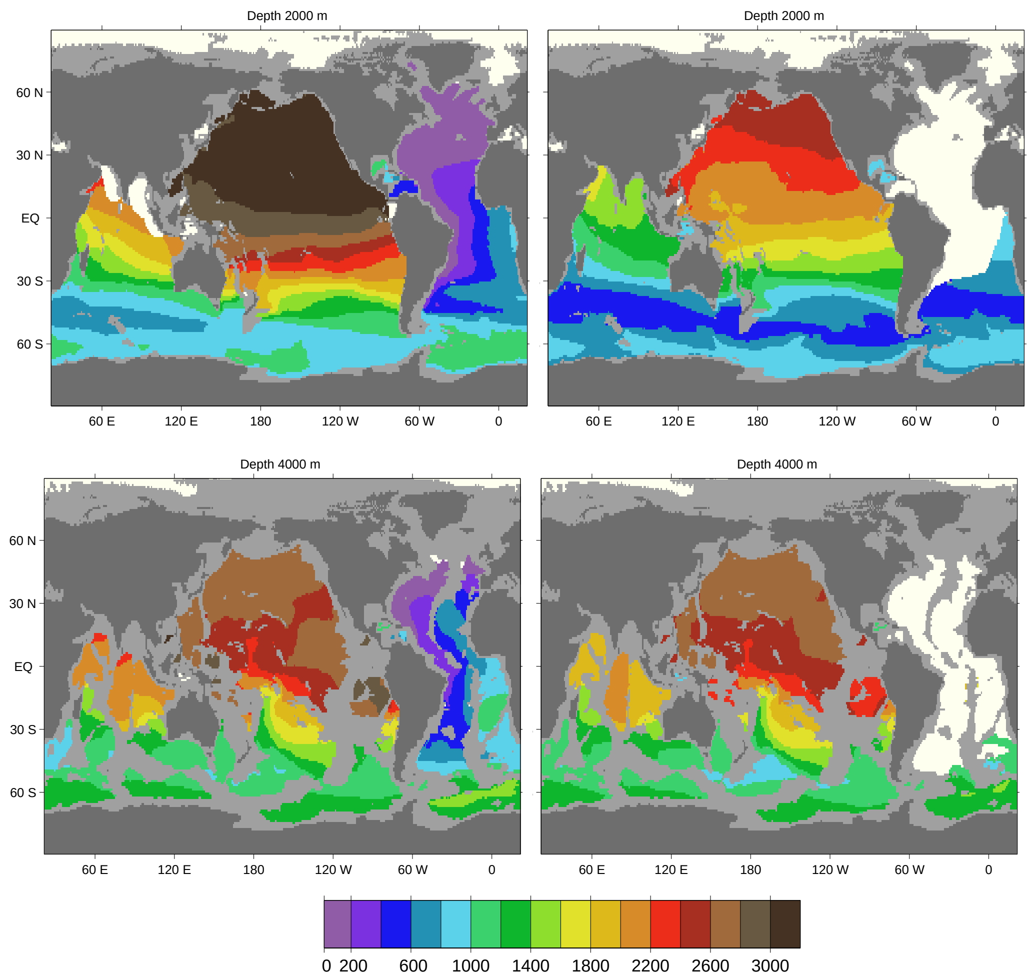

Figure 3.15: Ventilation age at 2000 m (top) and 4000 m (bottom), for ventilation fractions from the Labrador Sea (on the left) and the Southern Ocean (on the right). The age is shown where the contributing fraction is greater than 0.20.

known. This computation here serves as a further diagnostic on the circulation. How does the mean age for each fraction contribute to the total mean age of the water? This is implemented here as a two-step process, with an intermediate result γ_r for each region, for the efficiency gained by only having to invert the transport operator one time to obtain multiple solutions.

$$\mathbf{T}\gamma_r = f_r \tag{3.6}$$

from which the ideal age for each fraction can be calculated

$$\Gamma_r = \gamma_r / f_r \tag{3.7}$$

Here, f_r is the fraction computed previously, for the source region , and Γ_r is the ideal ventilation age of the source from the surface of the specified region.

From looking at the ocean basin composition of the source waters (refer back to Figure 3.4), the largest contributors for the major basins are the Southern Ocean, the Labrador Sea, and the GIN Sea. We examine how each of these major components ages as it travels away from its source. First, consider how the water ages traveling into the Atlantic. Figure 3.12 shows the time-travel for the GIN Sea, the Labrador Sea, and the Southern Ocean into the Atlantic basin as a zonal average. The age is shown wherever the fraction from the source region is greater than 0.2. There is an expected age progression for both the GIN and Labrador Seas, aging as they travel southwards. The Southern Ocean water's age increases with depth, to a greater extent than expected, to over 1400 years at the bottom. This may be another symptom of a lack of bottom water formation from near the surface. This water is taking as long to reach the bottom of the Southern Ocean as the Lab Sea and the Gin Sea waters take to travel from the North Atlantic to the Southern Ocean.

Figure 3.13 shows the time-travel for the GIN Sea, the Labrador Sea, and the Southern Ocean into the Pacific basin. The water ventilated in the Pacific itself stays mainly above 500 m. The contribution of the GIN Sea is relatively small, but it ages at about the same rate as the water from the Lab Sea or the Southern Ocean. The Labrador Sea shows the oldest age, over 3000 years extensively in the North Pacific at 2000 to 3000 m. Above 2000 m, it contributes less than 0.20 to the water mass present. The Southern Ocean waters have a significant presence throughout the basin, and a maximum age between 2600 and 2800 years at the North end of the basin at depths between 3000 and 4500 m. It is nearly as old as the water from the Lab Sea which has traveled much further.

Figure 3.14 shows the time-travel for the GIN Sea, the Labrador Sea, and the Southern Ocean into the Indian Ocean basin. The contribution of the GIN Sea does not extend very far, but it ages at about the same rate as the water from the Lab Sea or the Southern Ocean. The Labrador Sea shows the oldest age, over 2200 years at the northern end of the basin at 3000 to 4000 m. The aging rate is nearly the same at all depths, except at the bottom. The Southern Ocean waters have a significant presence throughout the basin, and a maximum age between 2000 and 2200 years at the bottom, just south of the Equator.

The evidence leads us to conclude that the Pacific and Indian oceans are sluggish at depth. For the Southern Ocean source: in the Pacific, the oldest is 2760 years old at around 3000 m; and in the Indian, the oldest is 2120 years old, near the bottom. For the Lab Sea source: in the Pacific, the oldest is around 3300 years old at around 2000 m; and in the Indian, oldest is around 2240 years old at 2000 to 4000 m.

The progression in age for all the North Atlantic source waters is similar, with the age at mid-depth in the Southern Ocean 1000 to 1200 years, with the waters getting progressively older as they move northward in the Pacific. $(3400 - 1000 =$

2400 years). The maximum ages are at around 2000 m, where the proportion of the North Atlantic source waters is getting lower. Figure 3.15 shows horizontal views at 2000 m and 4000 m, for the Labrador Sea and the Southern Ocean source waters. The maximum ages are on the eastern side of the basin, and at around 30N in the Pacific, as opposed to the far northern end of the basin. It is interesting to note that at the northern end of the Indian Ocean, at 2000 m, it is the Southern Ocean water that dominates. But in the Atlantic, the Southern Ocean water presence at 2000 m, while relatively young compared to that in the Pacific at the same latitude, barely extends to the equator.

3.6 Discussion

There are many features of the POP2 model's circulation that appear to be well-matched with observations of the real ocean; for example, the easy identification of Antarctic Intermediate Water. There remain concerns with the extreme old age in the deep North Pacific and North Indian basins. These old ages may result from sluggishness in the circulation, insufficient ventilated waters from the Southern Ocean, too much ventilated water from the North Atlantic, or some combination of these factors.

The comparison between the age in the deep Pacific and the age in the deep Atlantic is telling. Refer back to Figure 3.1. Everywhere in the deep Atlantic basin, the ventilation age is relatively youthful. But by the time it reaches the deep Southern Ocean, it has aged significantly. In this area the fraction of North Atlantic water is still high: 0.7 to 0.9. The fraction of Southern Ocean ventilated water is only 0.1 to 0.3. The fraction of Southern Ocean water decreases with increased depth. One might infer that there is not enough Southern Ocean ventilated water at depth in the Southern Ocean; that the age in the POP2 model is overwhelmed by the proportion of Atlantic waters in that area. However, in Figure 3.12 the age of the fraction ventilated in the Southern Ocean is almost the same as the waters ventilated in the Labrador or GIN Seas. Therefore, the accumulation of excessive age is beginning in the deep Southern Ocean.

In the Pacific, Figures 3.7, 3.9,and 3.5 together indicate that the composition of the water does not change much moving from about 20S to the northern end of the basin. However, Figure 3.13 shows a distinctive difference in the age from 20S northwards below 2000 m depth. Since the composition doesn't change much, the excessive model age is diagnosed as being due to sluggish circulation, particularly below depths of 2000 m.

The situation in the Indian Ocean is not so clear. Referring to the same figures, but examining the Indian basin, it can be seen that the composition changes as you move from the southern to the northern end of the basin, with the Atlantic waters decreasingly prevalent. Nevertheless, it is the Labrador Sea waters that show the oldest component age in the basin (Figure 3.14). This may be because in the model the youthful AAIW, which is also aging quickly at the end of the basin, dominates the mean age.

We have compared many of our results to those of DeVries and Primeau (2011) because the Inverse model's behavior has been constrained by temperature, salinity, sea-surface height, and freshwater fluxes. The most significant difference found between the POP2 model and the Inverse model is in the amount of ventilated waters resulting from the circulation characteristics in the Southern Ocean. In particular the DeVries and Primeau (2011) finding that 65% of the interior ocean water was ventilated there, as opposed to our finding of 39%. Clearly, the lack of AABW forming and pushing northward is affecting the circulation in the POP2 model. This may also contribute to the sluggishness of the circulation in the Pacific and Indian Ocean basins. On the other hand, in the North Atlantic, in

Chapter 2 the natural radiocarbon results of the model were found to be in excellent agreement with GLODAP data. From this we conclude that the strong ventilation found in the model in the North Atlantic cannot be too far off.

Gnanadesikan et al. (2002) studied the effects of the parameterization of vertical and lateral mixing on new production, because ocean biology is strongly controlled by ocean circulation. The authors found that the lateral and vertical diffusion coefficients could be modified to change the pathways of vertical exchange of nutrients without changing the structure of the thermocline. Using the Modular Ocean Model, Version 3 (Pacanowski and Griffies, 1999), they modified mixing parameters to determine the effects. While the shape of the remineralization profile had a dominant effect, holding that constant, they found a significant effect due to mixing, especially in the tropics. The conclusion was that the amount of vertical mixing, in particular, has a strong influence on the biological results.

In Chapter 2 some aspects of the parameterization of the mixing in the POP2 model are discussed. The vertical diffusion coefficient is weakest to mid-depths of 3000 m between 40S and 40N, and also below 4000 m between 50S and 30S. It is strongest in the far North Atlantic Labrador Sea region; nowhere in the Southern Ocean is it close to that strength. The isopycnal diffusion coefficient shows seasonal strengthening at depth in regions with latitudes polewards of 30N and 30S, but not to the intensity seen in the Labrador and GIN Sea regions.

3.7 Conclusions

It is important to understand the modeled ocean's characteristics when interpreting the results from application of the ocean model to further biological tracer or flux studies. The usefulness of the offline transport matrix for analysis and diagnosis of the circulation of the model becomes quite apparent from the above analysis. The transport matrix makes it feasible to do this kind of analysis in a relatively small amount of real time. The analysis can help with interpreting the results from applications that use the circulation model as a basis, such as nutrient and carbon cycling, or heat transport. The analysis results may also give insight into the physical processes and parameters in the model where further improvements could be made.

The Southern Ocean is considered to be critical for carbon cycling in the ocean (Toggweiler et al., 1989b). The amount of water that is ventilated there and carried to other locations is thus an important component in calculations of carbon uptake and release by the ocean. While this analysis has made visible the AAIW formation and its projection into the Atlantic, Indian, and Pacific basins (Figure 3.5), this analysis has also shown a lack of bottom water forming in the Southern Ocean. The excessive age of the Southern Ocean ventilated water at depths below 3000 m is visible in the Atlantic, Pacific, and Indian Ocean views (Figures 3.12, 3.13, and 3.14). The proportion of AABW protruding into the Atlantic, in particular, is missing (Figure 3.12). In Figure 3.11 , the waters from the North Atlantic fill in along the bottom where the proportion of AABW should be visible. Note also that the fraction of Southern Ocean-ventilated water in the Southern Ocean itself is small below 3000 m (Figure 3.5). This has consequences for the amount of carbon that will be carried to depth in the Southern Ocean.

The circulation in the model provides the underpinnings for nutrient cycling. Estimates of new production are based on nutrient consumption. That, in tern, is based on the difference between the nutrient concentration that is calculated to have arrived with the current, and what is observed in the water. Differences with the real ocean circulation may make the new production estimates either too high or too low. This analysis provides insight into the effects of the circulation in the deep; most of the nutrient cycling takes place in the upper layers, with some impact from the additional mixing that takes place due to storms primarily in the winter or early spring season. The Labrador Sea and the North Atlantic show a good match with the age of the water with observations (refer to Figures 3.1, 3.12, and Chapter 2. In the South Atlantic, in the Pacific, and in the Indian Ocean, the ventilated waters do not sink to depth, and maintain their youthful age (Figures 3.2 and 3.10). And from the Southern Ocean, the AAIW maintains its youth in the subsurface layer as it travels into the Atlantic, Pacific, and Indian basins (Figures 3.12, 3.13, and 3.14). This supports the underpinnings for nutrient cycling.

Oxygen minimum zones are an example of a phenomenon that depends on both the circulation model and the biological model being correct. Determining where oxygen minimum zones occur, and the circulation surrounding them, is important for determining where and how much denitrification is likely to be occurring as well. Here the excessive age in the Pacific and the Indian Oceans (Figure 3.1) , where the oxygen minimums zones tend to form, has an impact. The sluggish circulation can result in insufficient transport of oxygen into the zones, with a resulting exaggeration of the extent of the low oxygen regions. This symptom can be seen when a biological model uses the circulation as a basis for its computations (Moore et al., 2013).

Further research, beyond the scope of this paper, is needed to find the proximate causes of the characteristics of this ocean model that do not match well with observations. It is hoped that this analysis will aid in the quest for improving the model.

Chapter 4

A Study of Oxygen Concentrations in the Indian Ocean Using a Limited-domain Transport Matrix Technique

4.1 Abstract

In order to be able to predict the behavior of the oxygen minimum zones (OMZs) in the presence of anthropogenic perturbations, it is essential to understand the influence of both the circulation and the biogeochemistry on the present day conditions. This is a study of the interaction of the circulation and biogeochemistry on the concentrations of oxygen in the Indian Ocean, with a special focus on the OMZs. An offline seasonally-cycling version of the ocean component of the Community Earth System Model (CESM) is used, with the Indian Ocean effectively isolated, in a newly developed technique which takes into account the impact of

advection and diffusion from the boundaries. The biological effects on oxygen levels are estimated from production and consumption variables saved from an online simulation of the Biogeochemical Ecological Cycling (BEC) model.

By isolating the basin, we were able to separate of the influences of the biology and circulation inside the basin from those outside of it, providing a platform for studying the local influence of biological activity and circulation. Replacing the BEC-simulated oxygen concentrations on the boundaries with observational values greatly improved the agreement between the modeled and observed oxygen concentrations, and provided visibility into the remaining biases in oxygen concentration. Most notable is the mismatch in the position of the Arabian Sea OMZ, and the lack of intensity in both it and the Bay of Bengal OMZ. Oxygen ventilation pathways to the core of the OMZs originate predominantly from the Indian Ocean surface, rather than either the Southern Ocean or Indonesian Throughflow.

4.2 Introduction

Although IPCC-class Earth System models agree in predicting that the oceans are likely to lose oxygen in response to climate change (Bopp et al., 2013; Stramma et al., 2008; Matear and Hirst, 2003; Bopp et al., 2002), all the models are unable to match the observed present-day spatial patterns of oxygen concentrations. This is particularly true for areas of low oxygen concentrations (Bopp et al., 2013). Since observations suggest that a loss of oxygen from the ocean is already underway (Whitney et al., 2007; Chan et al., 2008; Stramma et al., 2012), the impact on species sensitive to oxygen levels, fishes and crustaceans (Vaquer-Sunyer and Duarte, 2008; Gray et al., 2002; Keeling et al., 2010), makes timeliness of the essence in the understanding of the mechanisms involved.

As oxygen is lost, the expansion of oxygen minimum zones (OMZs) can have a large impact on the habitat for the majority of the biota that require high oxygen concentrations to survive (Keeling et al., 2010). An additional concern with expanding OMZs is the impact of increased denitrification, and associated production of N_2O (a greenhouse gas); the loss of fixed nitrogen from the Arabian Sea OMZ is estimated to be 30 to 50% of the global oceanic water column fixed nitrogen loss from the oceans (Bulow et al., 2010), disproportionately large for its area. Changes in the effectiveness of the biological pump for sequestering CO_2 come from feedbacks that are both positive and negative. The heavier remineralization close to the surface increases the DIC close to the surface, which provides a shortened path for the return of CO_2 to the atmosphere, decreasing the effectiveness of the biological pump (Paulmier et al., 2011, 2006). The same remineralization converts nutrients to bioavailable form close to the surface, promoting additional production, and enhancing the biological pump (Paulmier et al., 2011). Within the OMZ itself, the bacterial consumption of particulate organic matter (POM) is retarded (Rogers, 2000; Levin et al., 2000; Gooday et al., 2000), which allows more POM to sink to lower depths in the water column, enhancing the effectiveness of the biological pump (Gage et al., 2000).

The impacts of losing oxygen in the ocean, and a desire to understand the mechanisms that are needed to make a good model representation of the dynamics controlling oxygen levels, are the motivation for this study. It is a challenge to recognize the controlling factors for oxygen concentrations, particularly at low levels, that result in the correct balance between the supply of oxygen-rich waters and the conditions for its biological consumption.

Among the models participating in CMIP5, there was general agreement that the oceans are likely to lose oxygen due to climate change, but on the geographic locations of the changes there was little agreement. The tropics, where the largest

OMZs reside, had the least convergence among the models, with less than 80% agreeing on the sign of the change. The estimates of the current global volume of water with oxygen concentrations of less than 5 mmol m^{-3} varied by a factor of 120, ranging both above and below the observed volume (Bopp et al., 2013). Stramma et al. (2012) compared modeled results with observed changes of O_2 concentrations over a 50 year historical period. Although suspected controlling factors of the circulation in the model were varied, the global pattern of the change in oxygen concentrations could not be matched.

Here we isolate the Indian Ocean from the CESM global model to create a regional offline model. The focus is on the oxygen sources and sinks within the region and from the boundaries of the region. Chapter 1 provided background from the scientific literature on what is known about the circulation in the Indian Ocean, the strong monsoonal effects, and the interfaces with the the Southern Ocean, the Indonesian Throughflow, the Persian Gulf, and the Red Sea. Background information was also presented on the physical structure of the OMZs, and on modeling studies that have encompassed the issues regarding the Indian Ocean and its OMZs (Bopp et al., 2013; Deutsch, 2011; Stramma et al., 2012; Resplandy et al., 2011, 2012; McCreary et al., 2013).

The construction of good biophysical models of the Arabian Sea and the Bay of Bengal is particularly challenging. A persistent problem is that models simulate lower O_2 concentrations in the Bay of Bengal than in the Arabian Sea, instead of the opposite seen in observations (Moore and Doney, 2007; Oschlies et al., 2008; Gnanadesikan et al., 2012; Moore et al., 2013). Another recurrent bias is the underestimation of primary production in the central Arabian Sea, which has been blamed on poor representation of the ecosystem complexity, on the lack of a diurnal cycle, and on mesoscale dynamics (Resplandy et al., 2011). While some modeling efforts have focused on trying to understand the controlling factors in the Arabian Sea (for example, Anderson et al. (2007); Kawamiya (2001); Resplandy et al. (2011, 2012)), there has been less scientific effort focused on the Bay of Bengal.

In Chapters 1 and 2, the circulation in the Pacific and the Indian Oceans were diagnosed as being too sluggish. In the Pacific, the ^{14}C age in the model reached over 3000 years, compared with observed ^{14}C age on the order of 1500 years. A low bias in oxygen concentrations will occur because 1) the instantaneous remineralization of POM will generate an oxygen deficit due to an insufficient rate in the supply of oxygen-rich waters; and 2) the model parameterized dissolved organic material (DOM) remineralization rates are based on time, resulting in excessive remineralization and oxygen consumption since the waters take more time to travel between locations. The BEC, in the 20th-century CMIP5 simulation has low oxygen concentrations at too many locations. We would like to analyze both the role of the tracer transport in the CESM model and the role of the boundary oxygen concentrations in the excessively-low oxygen concentration bias. The circulation is complex and highly seasonal at the surface. We need many ways of analyzing the model, including traditional ones and new ones, to diagnose the situation.

4.3 Research Questions and Strategy

This is a study of the interaction of the circulation and biogeochemistry of the Indian Ocean, and their combined effects on the Arabian Sea and the Bay of Bengal OMZs. The questions being examined are:

1. How much of the bias in the circulation is attributable to factors external to the Indian Ocean? To distinguish the circulation component from the

biological component of the biases in oxygen concentration within the region, we use a ^{14}C simulation as a metric. ^{14}C age gives us an integrated view of the rate of ventilation from the surface to the interior of the ocean. If the simulated ^{14}C age is too old compared to observations then the integrated water movement is too slow. As a result, the rate of arrival of oxygen-rich water from the source will be too slow. We know that there are substantial circulation biases as diagnosed with ^{14}C in the global circulation of the offline tracer transport model. If we can effectively isolate the Indian Ocean circulation, how much of that circulation bias remains within the region? How sensitive is the bias to the latitude of the southern boundary?

2. How much influence does the oxygen concentration on the boundaries with the Southern Ocean or the ITF have on the oxygen concentrations in the Indian Ocean? This breaks down into two more questions.

    (a) What is the oxygen concentrations at each oxygen-ventilation source? How much difference is there between using observations on the boundaries, and using the global BEC solution oxygen values for those boundaries?

    (b) How much of the water that is resident in an OMZ comes from each of the possible oxygen-ventilation sources: the Southern Ocean to the south, the Indonesian Throughflow to the east, or the surface of the Indian Ocean itself?

3. If we take away the external-to-the-region biases in oxygen on the boundary for the BEC calculated production and consumption of oxygen, do the biases in the oxygen concentrations within the region decrease?

4. Without external-to-the-region oxygen biases, what are the remaining biases in the oxygen concentrations within the region?

To study these questions, we isolated the Indian Ocean for examination, creating a regional model from the global offline seasonally-cycling tracer transport operator. Using ^{14}C as a tracer within the region, we can distinguish the impact of the circulation outside of the region from that within the basin by placing either ^{14}C observations or the the previously calculated global ^{14}C results on the boundaries of the region. Using BEC oxygen production and consumption variables inside the region, and either oxygen observations or the previously calculated global BEC oxygen concentration values on the boundaries, we can gain some insights into the difference between the local effects of the simulated biology and the effects stemming from outside of the region.

The Indian Ocean is isolated using a newly developed technique which preserves the advection and diffusion on the ocean boundaries, such that the waters incoming from the Southern Ocean from the south and the Indonesian Throughflow (ITF) to the east are incorporated into the regional model.

4.4 Methods

To answer the questions listed in Section 4.3 a limited domain offline matrix transport model and a suite of accompanying diagnostics has been developed. These are explained in this section. Also, the monsoonal seasonality of the Indian Ocean circulation in the offline model is examined.

4.4.1 The CESM ocean offline model

In Chapter 2 we developed an offline tracer transport operator, representing the seasonally-cycling advection and diffusion operators on a global basis, and

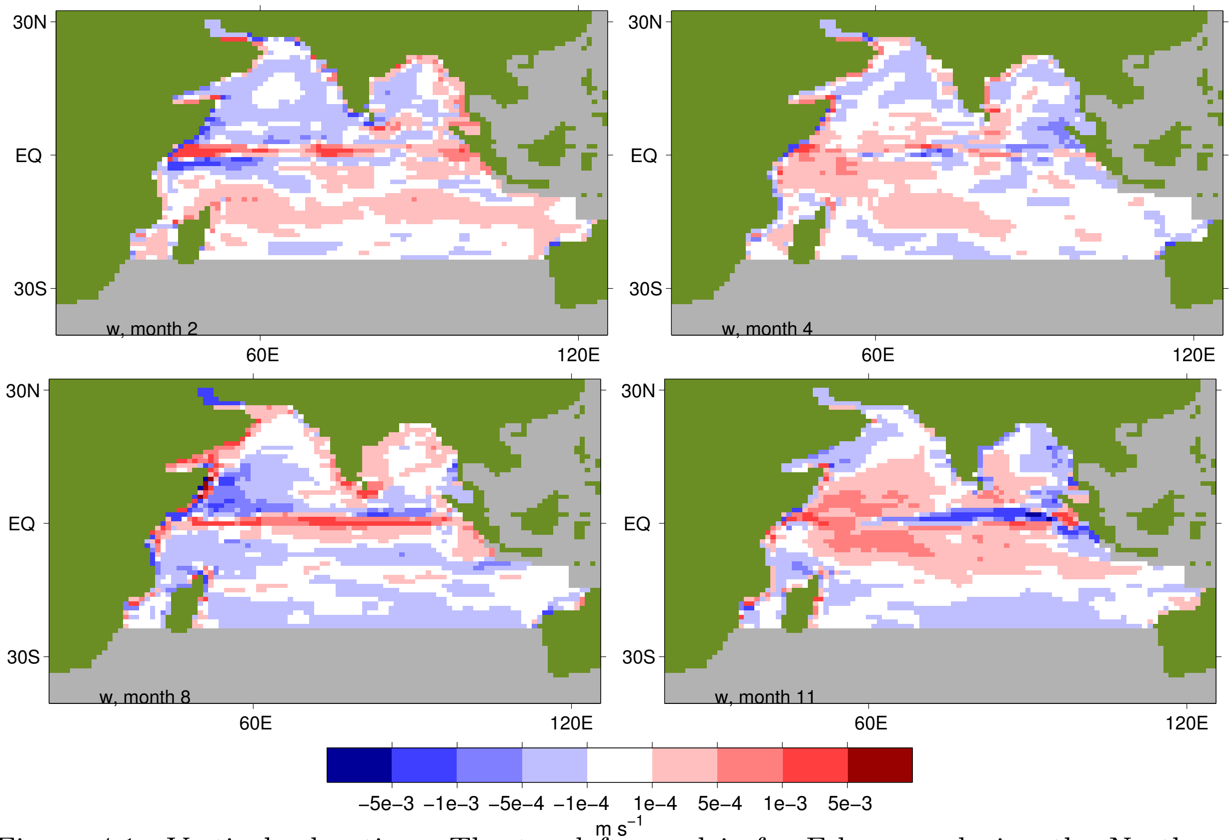

Figure 4.1: Vertical advection. The top left panel is for February, during the Northeast Monsoon; the top right panel is for April, during the Spring inter-monsoon; the bottom left panel is for August, during the Southwest Monsoon; the bottom right panel is for November, during the Fall inter-monsoon. The vertical advection is averaged over the top 100 m depth.

which was based on the CESM ocean component. In Section 4.4.2 the method of isolating the Indian Ocean region from the global offline model is given.

Documented in the literature are strong monsoonal winds that have a dominating influence on the surface currents north of 15S. To examine whether the surface circulation in the offline model has a reasonable representation of the strong monsoonal seasonal shifts, the components of the circulation are provided for the Indian Ocean region. Figure 4.1, shows the vertical component of advection, w, in the top 100 m. Values for months during the Northeast Monsoon, the Spring inter-monsoon, the Southwest Monsoon, and the Fall inter-monsoon are shown. Figure 4.2 shows the seasonal variations for the vertical diffusion coefficient. The western boundary current for the Arabian Sea is apparent in Figures 4.1 and 4.2.

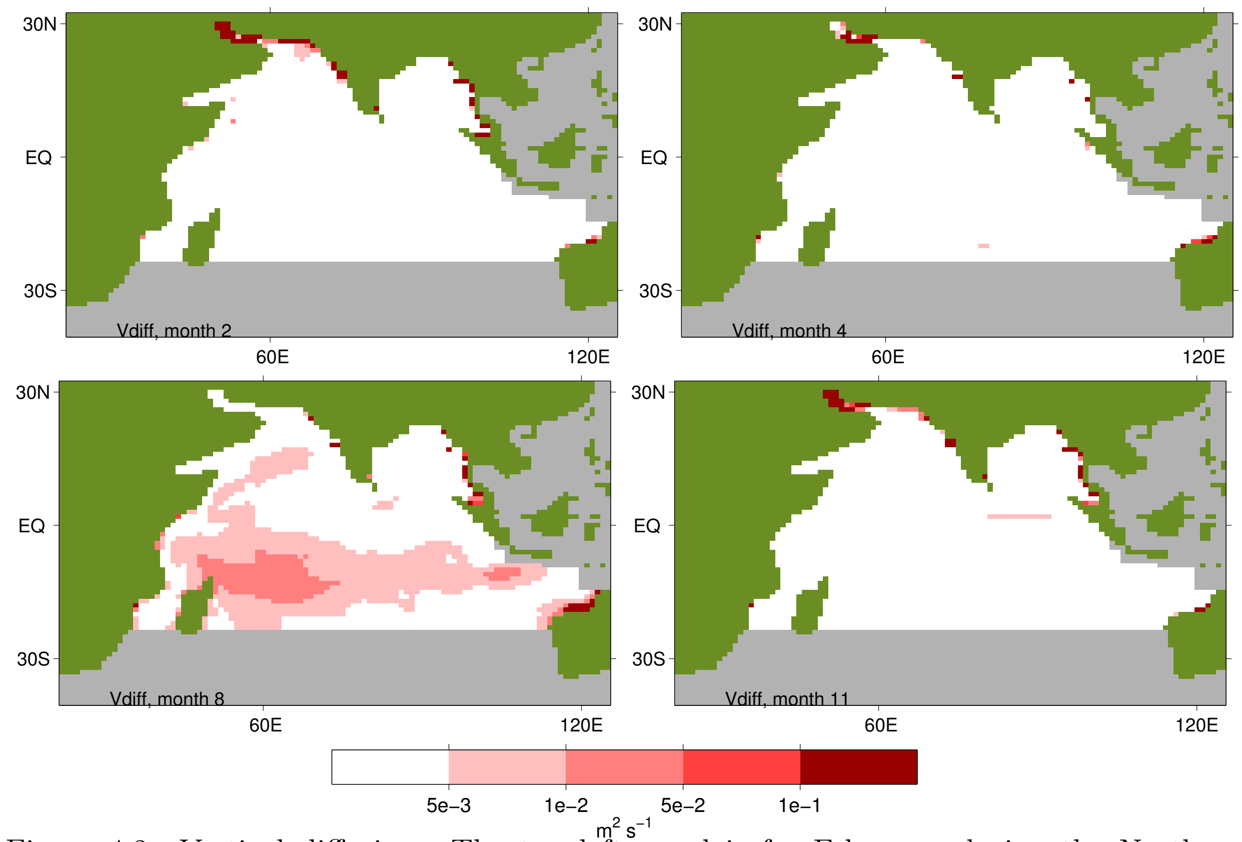

Figure 4.2: Vertical diffusion. The top left panel is for February, during the Northeast Monsoon; the top right panel is for April, during the Spring inter-monsoon; the bottom left panel is for August, during the Southwest Monsoon; the bottom right panel is for November, during the Fall inter-monsoon. The vertical diffusion is given as the average vertical diffusion coefficient, K_V, over the top 100 m depth color-coded for mid-range values.

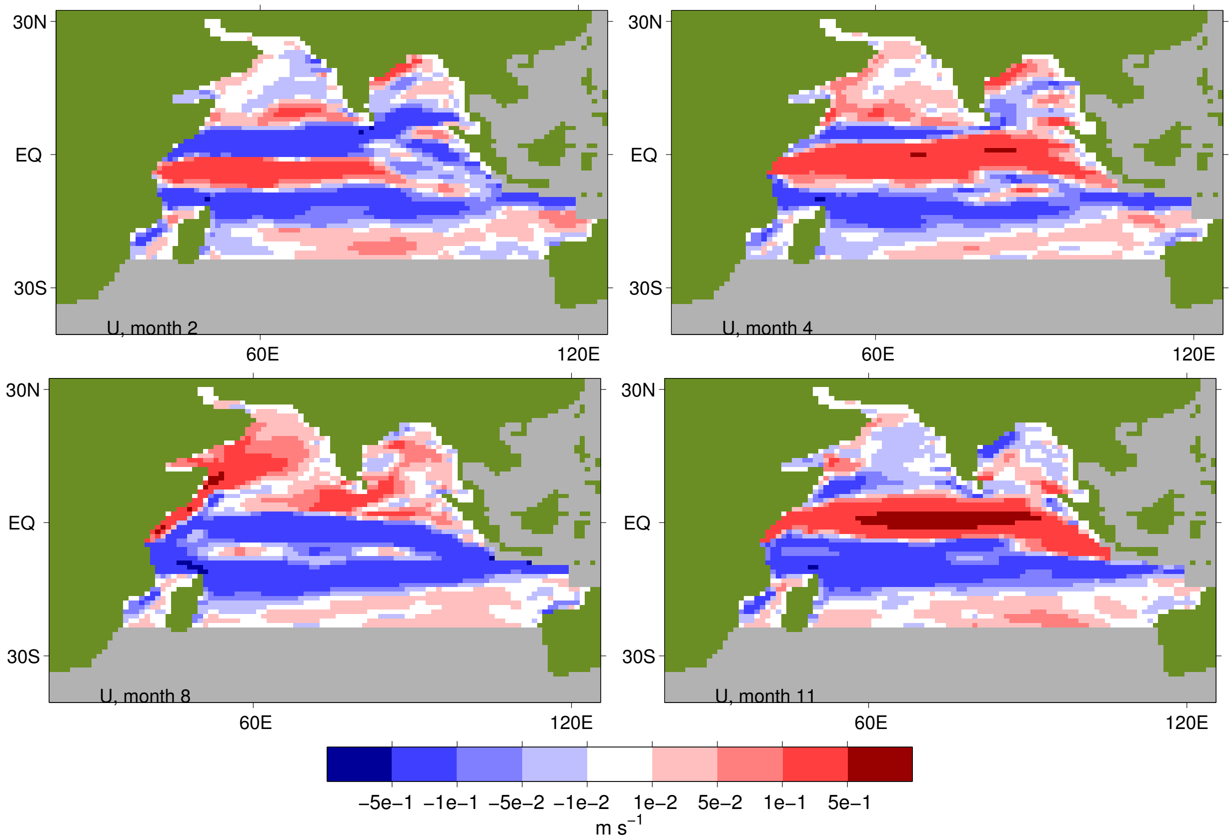

Figure 4.3: The zonal component of advection (eastwards positive). The top left panel is for February, during the Northeast Monsoon; the top right panel is for April, during the Spring inter-monsoon; the bottom left panel is for August, during the Southwest Monsoon; the bottom right panel is for November, during the Fall inter-monsoon. The zonal advection is averaged over the top 50 m depth. The seasonal shifts are striking.

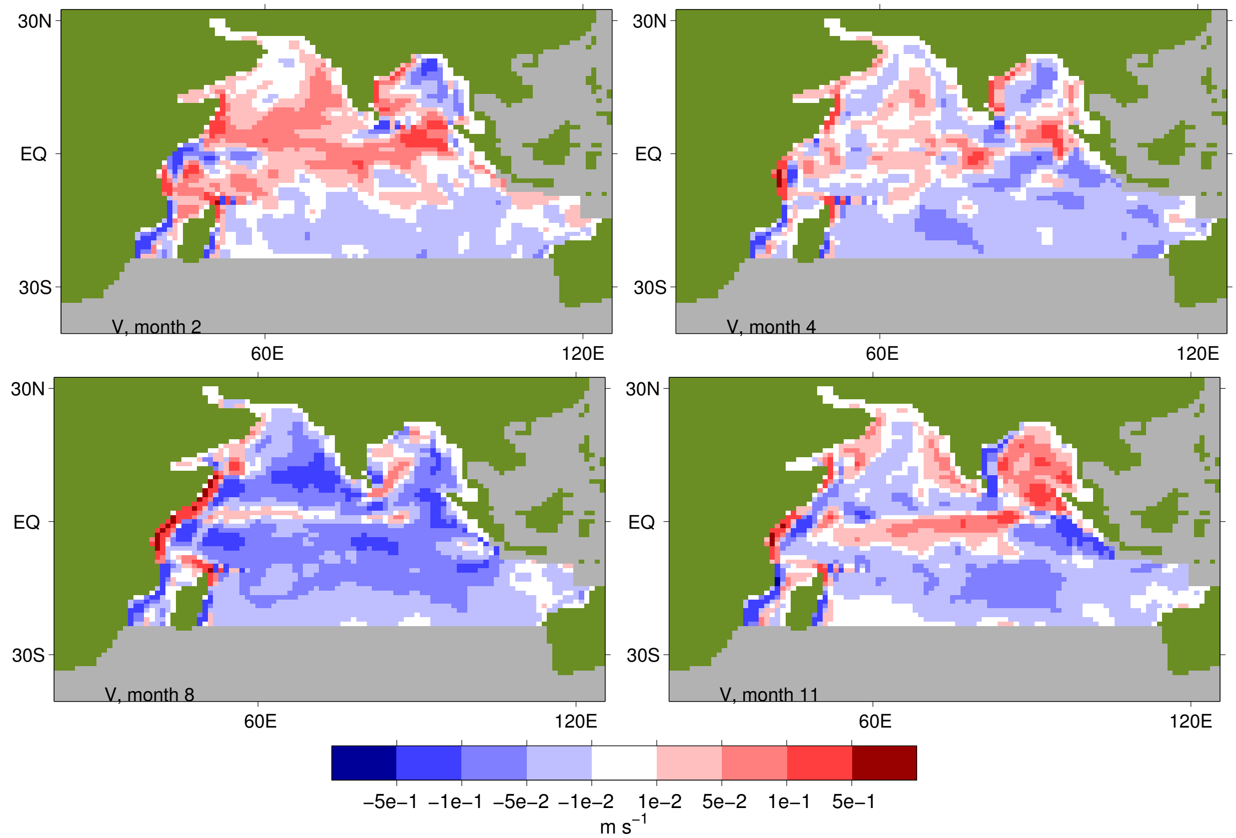

Figure 4.4: The meridional component of advection (northwards positive). The top left panel is for February, during the Northeast Monsoon; the top right panel is for April, during the Spring inter-monsoon; the bottom left panel is for August, during the Southwest Monsoon; the bottom right panel is for November, during the Fall inter-monsoon. The meridional advection is averaged over the top 50 m depth. Note the strength of the western boundary current along the Somali coast in the Southwest Monsoon.

During the Southwest Monsoon, there is strong upwards and downwards advection (Figure 4.1) and some vertical diffusion (Figure 4.2). There is no equivalent strong western boundary current for the Bay of Bengal.

The horizontal flow patterns are also of interest. Figure 4.3 shows the zonal (U) and Figure 4.4 the meridional (V) components of the surface circulation, as averaged in the top 50 m, for the monsoonal seasons. Note the zonal seasonal shift around the bottom of the Indian Subcontinent. During the Northeast Monsoon, the circulation is from the Bay of Bengal towards the Arabian Sea, while during the Southwest Monsoon the situation is reversed. There is a strong meridional component northwards during the Southwest Monsoon along the Somali Coast, with an eastward component in the Arabian Sea that would bring the well-oxygenated water in toward the central Arabian Sea.

The advection and diffusion fields do not lend themselves to directly answering the question of how much of the BEC excessively-low oxygen concentration bias is the result of the tracer advection and diffusion in the CESM model. We will need additional techniques to provide more insight.

4.4.2 Isolating the Region

Here we use a geographical subset of the previous global transport operator, where the boundaries are partly in the water, as opposed to the all-land boundaries in the global case. Tracer values at the oceanic boundaries appear as sources or sinks to the interior cells of the region.

Method development

The sub-setting, allowing the incorporation of the desired boundary condition, is accomplished as follows. For the equilibrium steady-state solution:

$$\frac{\partial c}{\partial t} + \mathbf{T}c + S = 0. \tag{4.1}$$

$\mathbf{T}$ is the tracer transport operator, a large sparse square matrix, with the dimensions of the number of ocean grid-cells in the parent model. The entries in the matrix are taken from the 3-D advection fields and the diffusivity tensor of the parent prognostic model (see Chapter 2 for more details). c is a vector of the tracer concentrations in each ocean grid-cell. S represents sources or sinks of the tracer, such as the air-sea flux of O_2, the respiration losses of O_2, or the radioactive decay of ^{14}C.

The grid cells can be divided into those to be included in the region of interest, and those outside of the region. Likewise, the transport operator can be partitioned into parts that deal only with the interior of the region, only with the exterior of the region, and the parts that treat the interactions between the interior and exterior regions:

$$\frac{\partial}{\partial t}\begin{bmatrix} c_{\mathsf{i}} \\ c_{\mathsf{e}} \end{bmatrix} + \begin{bmatrix} \mathbf{T}_{\mathsf{ii}} & \mathbf{T}_{\mathsf{ie}} \\ \mathbf{T}_{\mathsf{ei}} & \mathbf{T}_{\mathsf{ee}} \end{bmatrix} \begin{bmatrix} c_{\mathsf{i}} \\ c_{\mathsf{e}} \end{bmatrix} + \begin{bmatrix} S_{\mathsf{i}} \\ S_{\mathsf{e}} \end{bmatrix} = 0, \tag{4.2}$$

where $\mathbf{T}_{\mathsf{ii}}$ is the transport operator only for the interior grid-cells; $\mathbf{T}_{\mathsf{ee}}$ is the transport operator only for the exterior grid-cells; $\mathbf{T}_{\mathsf{ie}}$ and $\mathbf{T}_{\mathsf{ei}}$ are the operators for the interactions between the interior and exterior grid-cells. $\mathbf{T}_{\mathsf{ie}}$ contains the rows corresponding to the indices for the interior grid-cells and the columns corresponding to the indices for the exterior grid-cells. Likewise, $\mathbf{T}_{\mathsf{ei}}$ contains the rows for the exterior grid-cells and the columns for the interior grid-cells. c_{i} is a vector of the tracer concentrations of the interior grid-cells; c_{e} is a vector of the tracer concentrations exterior to the region. Likewise S_{i} and S_{e} are the source or sink terms for the interior and external grid-cells.

Explicitly writing out the block multiplication for equation (4.2), and shifting the source or sink terms to the right-hand side gives:

$$\frac{\partial c_{\mathsf{i}}}{\partial t} + \mathbf{T}_{\mathsf{ii}} c_{\mathsf{i}} = -\mathbf{T}_{\mathsf{ie}} c_{\mathsf{e}} - S_{\mathsf{i}} \tag{4.3}$$

$$\frac{\partial c_{\mathsf{e}}}{\partial t} + \mathbf{T}_{\mathsf{ee}} c_{\mathsf{e}} = -\mathbf{T}_{\mathsf{ei}} c_{\mathsf{i}} - S_{\mathsf{e}} \tag{4.4}$$

Our analysis is focused on the selected region and its boundaries, and not on the exterior. Therefore only equation (4.3) is needed. This form of the equation provides a mechanism to replace model tracer concentrations with observations on the boundary by replacing c_{e} in the term $\mathbf{T}_{\mathsf{ie}} c_{\mathsf{e}}$. It becomes a source term for the interior grid-cells next to the boundary.

For the steady-state equilibrium case, where the transport and the tracer concentrations are held at their average values, $\frac{\partial c_{\mathsf{i}}}{\partial t} = 0$, and assuming S_{i} is not a function of c_{i}, we have only to solve the rate equation:

$$-\mathbf{T}_{\mathsf{ii}} c_{\mathsf{i}} = \mathbf{T}_{\mathsf{ie}} c_{\mathsf{e}} + S_{\mathsf{i}} \tag{4.5}$$

This form of the equation can be solved directly by inverting the matrix to find the equilibrium values of the tracer concentration of the regional interior grid-cells.

$$c_{\mathsf{i}} = -\mathbf{T}_{\mathsf{ii}}^{-1} (\mathbf{T}_{\mathsf{ie}} c_{\mathsf{e}} + S_{\mathsf{i}}) \tag{4.6}$$

To adapt this to a seasonal-cycling equilibrium solution for the tracer, the transport operator, the boundary tracer values, and the source-sink terms must be allowed to vary with time. We define the function:

$$\mathcal{F}(c_{\mathsf{i}}, t) \equiv \int_{t}^{t+\Delta t} (\mathbf{T}_{\mathsf{ii}}(t)c_{\mathsf{i}} + \mathbf{T}_{\mathsf{ie}}(t)c_{\mathsf{e}}(t) + S_{\mathsf{i}}(t, c_{\mathsf{i}}))\mathrm{d}t \tag{4.7}$$

Here, $\mathbf{T}_{\mathsf{ii}}(t)$ reflects the time dependence of the transport operator. This is implemented as a set of 12 monthly transport operators, with monthly-average concentrations on the boundary. The time t to $t + \Delta t$ in the limits of integration correspond to 1 year. Note that the $S_{\mathsf{i}}(t, c_{\mathsf{i}})$ term can be a function of the tracer concentration as well as time, as is the case for a seasonal air-sea interface. In seasonal equilibrium, the tracer values are the same at the end of the year as at the beginning, and thus the problem to be solved is to find $c_{\mathsf{i}}(t)$ such that:

$$\mathcal{F}(c_{\mathsf{i}}, t) = 0 \tag{4.8}$$

The above problem can be solved for c_{i} using a Newton-Krylov solver. The evaluation of $\mathcal{F}(c_{\mathsf{i}}, t)$ is performed by time-stepping through a 1-year cycle, as described in Chapter 2.

Validation of regional partitioning using Δ^{14}C

To validate the partitioning into the regional model, prebomb Δ^{14}C results from the previous study of the global ocean circulation in Chapter 2 can be compared to the results from the regional model. If we use boundary Δ^{14}C values obtained in the previous global model solution, this should produce the same results in the regional model as the full global model. Figure 4.5 demonstrates that this is so; that using just the regional part of the model did not change the tracer result. The regional and the global solution are indistinguishable. It should be noted that both the global and the regional results were calculated using the same offline circulation to achieve this degree of agreement.

4.4.3 Boundary ventilation sources of oxygen

To examine the impact of boundary conditions on the resulting OMZ oxygen concentrations, the source of the waters resident in an OMZ is of interest. An efficient method of calculating the proportion of source water from each of the grid-cells on the surface to an interior defined region, such as an OMZ, is derived below. This method will be applied to both the surface and the lateral boundaries of the region. The derivation is based on an annually-averaged transport matrix.

The discretized tracer transport equation, partitioned into surface (labeled s) and interior (labeled i) grid-cells can be written as follows:

$$\frac{d}{dt}\begin{bmatrix} c_{\mathsf{s}} \\ c_{\mathsf{i}} \end{bmatrix} + \begin{bmatrix} \mathbf{T}_{\mathsf{ss}} & \mathbf{T}_{\mathsf{si}} \\ \mathbf{T}_{\mathsf{is}} & \mathbf{T}_{\mathsf{ii}} \end{bmatrix} \begin{bmatrix} c_{\mathsf{s}} \\ c_{\mathsf{i}} \end{bmatrix} = 0. \tag{4.9}$$

$\mathbf{T}_{\mathsf{ii}}$ is the transport operator only for the interior grid-cells; $\mathbf{T}_{\mathsf{ss}}$ is the transport operator only for the surface grid-cells; and $\mathbf{T}_{\mathsf{is}}$ and $\mathbf{T}_{\mathsf{si}}$ are the operators for the boundaries between the interior and surface grid-cells. c_{i} is a vector of the tracer concentrations of the interior grid-cells; c_{s} is a vector of the tracer concentrations on the surface.

If we prescribe the surface concentration to be 1 in the k'th surface grid-cell and zero in all other surface grid-cells and integrate Equation (4.9) until the steady state is reached, the final state is the solution that satisfies the following linear system of equations:

$$\mathbf{T}_{\mathsf{ii}}\mathbf{f}_{\mathsf{i}}^{k} + \mathbf{T}_{\mathsf{is}}\mathbf{e}_{\mathsf{s}}^{k} = 0, \tag{4.10}$$

where the vector $\mathbf{e}_{\mathsf{s}}^{k}$ is a vector of 0's except in the k'th surface box where it is equal to 1; and $\mathbf{f}_{\mathsf{i}}^{k}$ represents the fraction of water last ventilated from the k'th surface grid-cell. Solving for $\mathbf{f}_{\mathsf{i}}^{k}$ we obtain:

$$\mathbf{f}_{\mathsf{i}}^{k} = -\mathbf{T}_{\mathsf{ii}}^{-1}\mathbf{T}_{\mathsf{is}}\mathbf{e}_{\mathsf{s}}^{k}. \tag{4.11}$$

Now suppose we only care about the elements of $\mathbf{f}_{\mathsf{i}}^{k}$ corresponding to grid-cells inside a particular OMZ of the ocean. Let $\mathbf{o}_{\mathsf{i}}$ be a vector with 0's everywhere except for the grid-cells in the OMZ where the elements are set to 1. Then the proportion of the water in the OMZ that was last ventilated from the k'th surface grid-cell is given by

$$p^{k} = \frac{\mathbf{o}_{\mathsf{i}}'\mathbf{V}_{\mathsf{ii}}\mathbf{f}_{\mathsf{i}}^{k}}{\mathbf{o}_{\mathsf{i}}'\mathbf{V}_{\mathsf{ii}}\mathbf{o}_{\mathsf{i}}}, \tag{4.12}$$

where the matrix $\mathbf{V}_{\mathsf{ii}}$ is a diagonal matrix whose non-zero elements are the grid-cell volumes. Note that right multiplying by $\mathbf{o}_{\mathsf{i}}'\mathbf{V}_{\mathsf{ii}}$ is equivalent to integrating over the volume of the OMZ. We wish to repeat the above computation for all n surface grid-cells to get

$$\mathbf{p}_{\mathsf{s}}^{'} = \frac{1}{\mathbf{o}_{\mathsf{i}}'\mathbf{V}_{\mathsf{ii}}\mathbf{o}_{\mathsf{i}}} \left(\mathbf{o}_{\mathsf{i}}'\mathbf{V}_{\mathsf{ii}} \left[\, \mathbf{f}_{\mathsf{i}}^{1} \quad \mathbf{f}_{\mathsf{i}}^{2} \quad \cdots \quad \mathbf{f}_{\mathsf{i}}^{n} \,\right]\right), \tag{4.13}$$

where $\mathbf{p}_{\mathsf{s}}^{'} = [\, p^1 \quad p^2 \quad \cdots \quad p^n \,]$. Substituting in Equation (4.11) we get

$$\mathbf{p}_{\mathsf{s}}^{'} = \frac{-1}{\mathbf{o}_{\mathsf{i}}^{\prime}\mathbf{V}_{\mathsf{ii}}\mathbf{o}_{\mathsf{i}}} \left(\mathbf{o}_{\mathsf{i}}^{\prime}\mathbf{V}_{\mathsf{ii}}\mathbf{T}_{\mathsf{ii}}^{-1}\mathbf{T}_{\mathsf{is}} \,[\, \mathbf{e}_{\mathsf{s}}^{1} \quad \mathbf{e}_{\mathsf{s}}^{2} \quad \cdots \quad \mathbf{e}_{\mathsf{s}}^{n} \,] \right). \tag{4.14}$$

Note that since the number of surface grid-cells is large ($n \gg 1$), the computational burden can be excessive even with a fast matrix solver. To speed things up we take the transpose and obtain

$$\mathbf{p}_{\mathsf{s}} = \frac{-1}{\mathbf{o}_{\mathsf{i}}^{\prime}\mathbf{V}_{\mathsf{ii}}\mathbf{o}_{\mathsf{i}}} \left([\mathbf{T}_{\mathsf{is}}]^{\prime} \left([\mathbf{T}_{\mathsf{ii}}^{\prime}]^{-1} \left(\mathbf{V}_{\mathsf{ii}}\mathbf{o}_{\mathsf{i}} \right) \right) \right), \tag{4.15}$$

where we used the fact that

$$\mathbf{I}_{\mathsf{ss}} = [\, \mathbf{e}_{\mathsf{s}}^{1} \quad \mathbf{e}_{\mathsf{s}}^{2} \quad \cdots \quad \mathbf{e}_{\mathsf{s}}^{n} \,]^{\prime} \tag{4.16}$$

is the $n \times n$ identity matrix. Note that the expression in Equation 4.15 involves only one matrix inversion provided one respects the order of operations implied by the parentheses, which will therefore be computationally efficient.

$\mathbf{p}_{\mathsf{s}}$ gives the proportion of the water in the OMZ that was last ventilated from each surface grid-cell. This method is applied to all the boundaries we have defined: the Southern Ocean and ITF boundaries in addition to the surface of the Indian Ocean.

We have the case of needing to determine the source from more than one in-the-water boundary. To be assured that the boundary sources are not intermingled or counted more than once, we use the minimum number of grid-cells necessary from the exterior adjacent to the interior grid-cells on the boundary. In the case of the surface layer, the top side of the grid-cells interface with the air, and the water mass does not cross that boundary. Tracer fluxes in and out of the surface ocean layer involve processing of the "air-sea flux", rather than being transported across that boundary by the ocean advection or diffusion. The surface layer of grid-cells is sufficient. For the in-the-water boundaries this is not the case. As discussed in Chapter 2, the total transport operator matrix is the sum of advection, horizontal diffusion, and vertical diffusion operator matrices. Within one time-step, advection tendencies are influenced by a 2 grid-cell range in the upwind direction. That range is incorporated within the transport operator matrices. Thus, a grid-cell at the edge of the defined interior region can have an advective or diffusive interface with the ocean grid-cells in the exterior that are anywhere within the 2 grid-cell radius if not blocked by land. This leads to an in-the-water boundary that is basically 2 grid-cells wide. The vertical diffusion presents no additional complication because the effects are straight up and down the water column, and the in-the-water boundaries share that alignment.

4.4.4 Oxygen Observations

For comparison with model results, and for observational boundary conditions, the monthly mean climatological values of oxygen from the World Ocean Atlas 2013 (WOA13) (Garcia et al., 2014) were used. For oxygen, WOA13 covers the oceans on a 1° grid with a set of objectively analyzed climatological fields. The thickness of the depth levels in WOA13 ranges from 5 m in the top 100 m, increasing to 100 m thickness below 2000 m. The WOA13 database [O_2] data is supplied on a climatological-month basis to a depth of 1500 m; below that depth data is supplied on a climatological-season (a 3 month average) basis. To create the set of monthly [O_2] values used in this analysis, WOA13 [O_2] values were remapped to the CESM ocean component's configuration, using the monthly averages where available, and filling in with the seasonal values as constant for the 3-month season.

4.4.5 The Oxygen Regional Model

We want to determine how much of the oxygen concentration biases seen in the global BEC solution are from outside of the Indian Ocean region, as opposed to locally produced. And what the biases are in the oxygen concentrations when the influence of the external biases in oxygen concentrations has been eliminated.

To drive the regional oxygen model, BEC production and remineralization output variables are used from the CMIP5 BEC simulation with the conditions described in Chapter 1. The remineralization term comes directly from the O_2 consumption calculated in the BEC. The oxygen consumption is decreased to zero as the O_2 concentration decreases from 6 to 4 mmol m^{-3}, preventing the consumption of O_2 under low-oxygen conditions (Moore et al., 2013). O_2 consumption includes oxygen consumption from remineralization of both POM and semi-labile DOM.

The oxygen production in the offline regional model is based on a total of the organic carbon produced during photosynthesis by the multiple phytoplankton types in the BEC: small phytoplankton, diatoms, and diazatrophs. Production is tracked in units of carbon. For the regional model, as in the full BEC, the units of carbon produced are converted to units of oxygen, using a Redfield ratio of 170/117.

To make the regional model based on the BEC-calculated O_2 production and consumption is straightforward:

$$\frac{\partial[\mathrm{O}_{2(\mathsf{i})}]}{\partial t} = \mathbf{T}_{\mathsf{ii}}[\mathrm{O}_{2(\mathsf{i})}] + P - C + A + \mathbf{T}_{\mathsf{ie}}[\mathrm{O}_{2(\mathsf{e})}]. \tag{4.17}$$

where $[O_2]$ is the oxygen concentration, $\mathbf{T}_{\mathsf{ii}}$ is the time-dependent transport operator for the interior grid-cells; P is the time dependent O_2 production rate; C is the time dependent O_2 consumption rate; A is the air/sea transfer rate term, calculated per the Ocean Carbon-Cycle Model Intercomparison Project 2 (OCMIP2) specification; and $\mathbf{T}_{\mathsf{ie}}\mathrm{O}_{2(b)}$ is the one-way flux of O_2 coming through the lateral boundaries.

For the seasonal cycle equilibrium solution, over the course of a year, the change in O_2 concentration is zero:

$$\mathcal{F}([\mathrm{O}_{2(\mathsf{i})}], t) = 0 \tag{4.18}$$

where

$$\mathcal{F}([\mathrm{O}_{2(\mathsf{i})}], t) \equiv \int_0^{1yr} (\, \mathbf{T}_{\mathsf{ii}}[\mathrm{O}_{2(\mathsf{i})}] + P - C + A + \mathbf{T}_{\mathsf{ie}}[\mathrm{O}_{2(\mathsf{e})}] \,) \, \mathrm{d}t \tag{4.19}$$

A Newton-Krylov technique applied to Equation 4.18 is used to solve for the $[O_2]$ seasonal-cycling equilibrium solution, as described in Chapter 2.

4.5 Determining circulation biases

How much of the bias in the circulation is generated externally, outside of the Indian Ocean region? And how sensitive is the bias within the region to the latitude of the southern boundary? We use ^{14}C as a non-biological tracer to determine the answers.

4.5.1 Local versus global biases

To examine this issue, two cases using differing boundary values applied to the regional ^{14}C simulation are defined. First, boundary values of $\Delta^{14}C$ from the global simulation (from the previous study in Chapter 2) are used. Second,

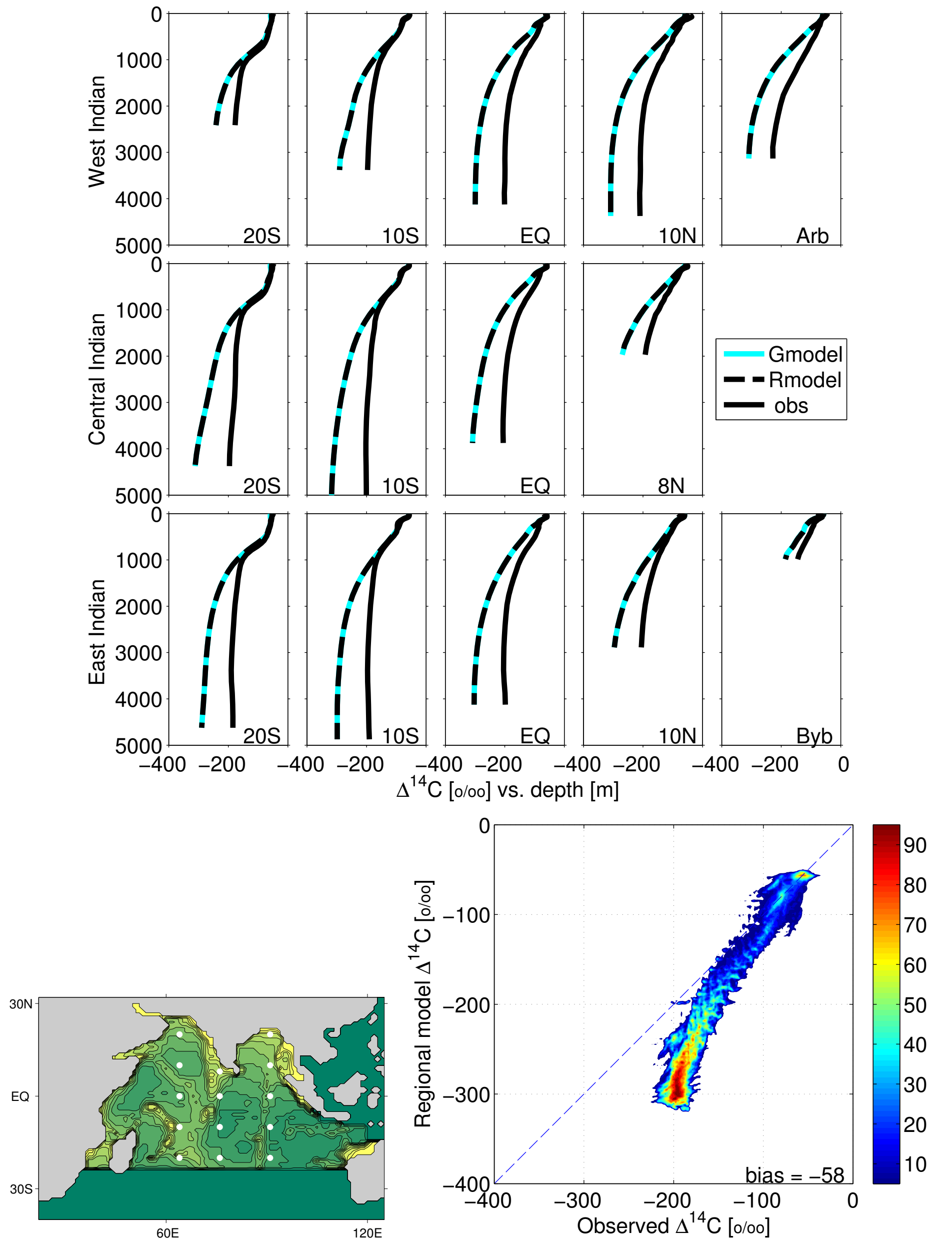

Figure 4.5: Results using boundary conditions from the global offline model solution for $\Delta^{14}C$. The top panel shows profiles of $\Delta^{14}C$ from the regional model (dashed, black); from the global model solution (solid,cyan); and from GLODAP observational data (solid, black); all versus depth. The latitude of the profile is indicated at the bottom right of each panel. "Arb" stands for the Arabian Sea. "Byb" stands for the Bay of Bengal. The global and regional values are nearly the same. The bottom left panel shows the locations of the profiles as white dots on a background topographical map based on the model. The bottom right panel is a scatter-density diagram of the regional results versus GLODAP observations. This is similar to a scatter diagram, but the color-codes give the relative density of the data points.

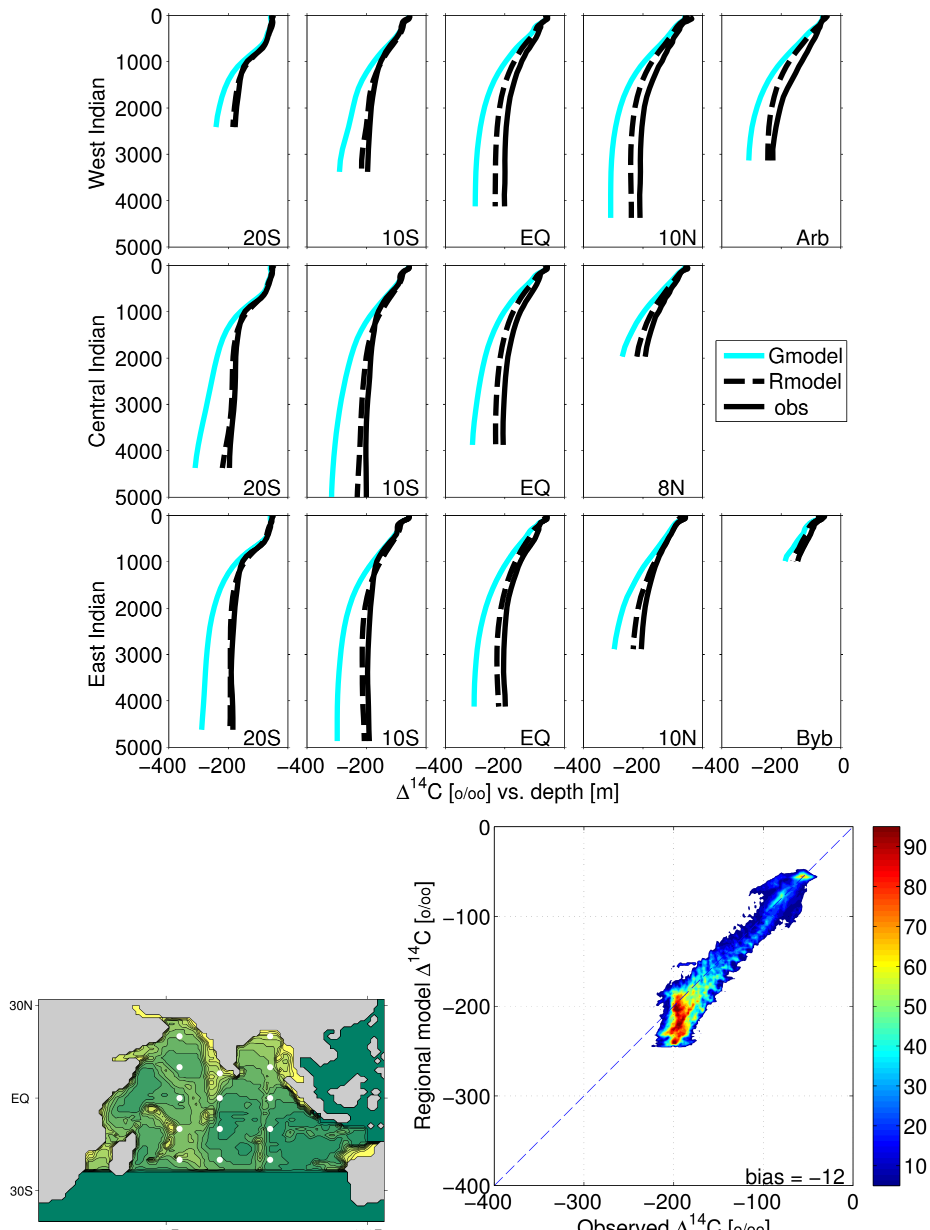

Figure 4.6: Results using GLODAP observational Δ^{14}C for boundary conditions; this is the only change in the conditions from the results shown in Figure 4.5. The top panel shows profiles of Δ^{14}C from the regional model (dashed, black); from the global model (solid,cyan), and from GLODAP observational data (solid, black); all versus depth. The bottom left panel shows the locations of the profiles as white dots on a background topographical map from the model. The bottom right panel is a scatter-density diagram of the regional model results versus GLODAP observations.

boundary values of $\Delta^{14}C$ from the GLODAP observational data set are used. The remaining deviations from observations in the second case are then attributable to circulation biases within the region.

In Figure 4.5 both the global-solution values (from Chapter 2) and the regional model results are compared to GLODAP gridded observational prebomb $\Delta^{14}C$ values (Key et al., 2004). Since the GLODAP $\Delta^{14}C$ data does not extend into the Indonesian Through Flow (ITF) area, the border between the ITF and the Indian Ocean basin was chosen such that GLODAP data is available for the boundary. The GLODAP $\Delta^{14}C$ data also does not extend into the Persian Gulf; however placing the boundary at the entrance to the Persian Gulf puts the boundary into a low oxygen region, which is undesirable for this study. As a result, the Persian Gulf has been included in the Indian Ocean region, making the northern boundary all land. The modeled $\Delta^{14}C$ values in the Persian Gulf are excluded from the comparisons with observations. $\Delta^{14}C$ observational data availability was not a concern for the Southern Ocean boundary.

Figure 4.5 also compares the results for water column profiles in various locations in the basin. The global-solution values are shown in cyan. The GLODAP values are the solid black lines. The regional model results, using the boundary conditions of the $\Delta^{14}C$ values from the global offline ocean model solution, are shown as a dashed black line.

The differences with the GLODAP observational data are significant. The volume-weighted bias (the average of the modeled data minus the observational data for each grid-cell, weighted by the volume of the grid-cell) is -59‰. From the scatter-density diagram, it is apparent that the differences are the worst for the most-negative (oldest) values. Where the GLODAP $\Delta^{14}C$ observations are around -200‰, the model values are around -300‰. For the least-negative (youngest) values, which occur near the ocean surface, the match to observations is much better.

Figure 4.6 illustrates the resulting profiles when observatrions are used on the boundaries: nothing is different from Figure 4.5 except the dashed line for the regional results. The regional model results are markedly closer to the observations. The technique has effectively greatly reduced the effect of circulation problems that occur outside of the regional study area. There remains a small bias of $-12‰$, compared to the bias of $-59‰$ for the global solution of the region. The scatter-density diagram gives the same picture: the regional model results fall much closer to the 1-to-1 line with the observations. It is the most-negative (oldest) values that show the most improvement.

4.5.2 Sensitivity to the latitude of the Southern Ocean Boundary

To examine how sensitive the latitude of the Southern Ocean boundary is to the regional model, experiments varying the latitude of the Southern Ocean boundary for the Indian Ocean study region were performed. All of the experiments used GLODAP $\Delta^{14}C$ values on the boundaries, and computed the $\Delta^{14}C$ values in the region defined by the Southern Ocean boundary. The latitudes chosen were 34S, near the southern tip of Africa; 26S, near the southern end of Madagascar; and 12S, near the top of Madagascar.

Southern boundary at 34S A southern boundary of 34S, near the southern tip of Africa resulted in the profiles and scatter-density diagram for the regional model and the global model shown in Figure 4.7. A comparison with GLODAP observational data is also shown. The $\Delta^{14}C$ values retain a substantial bias of

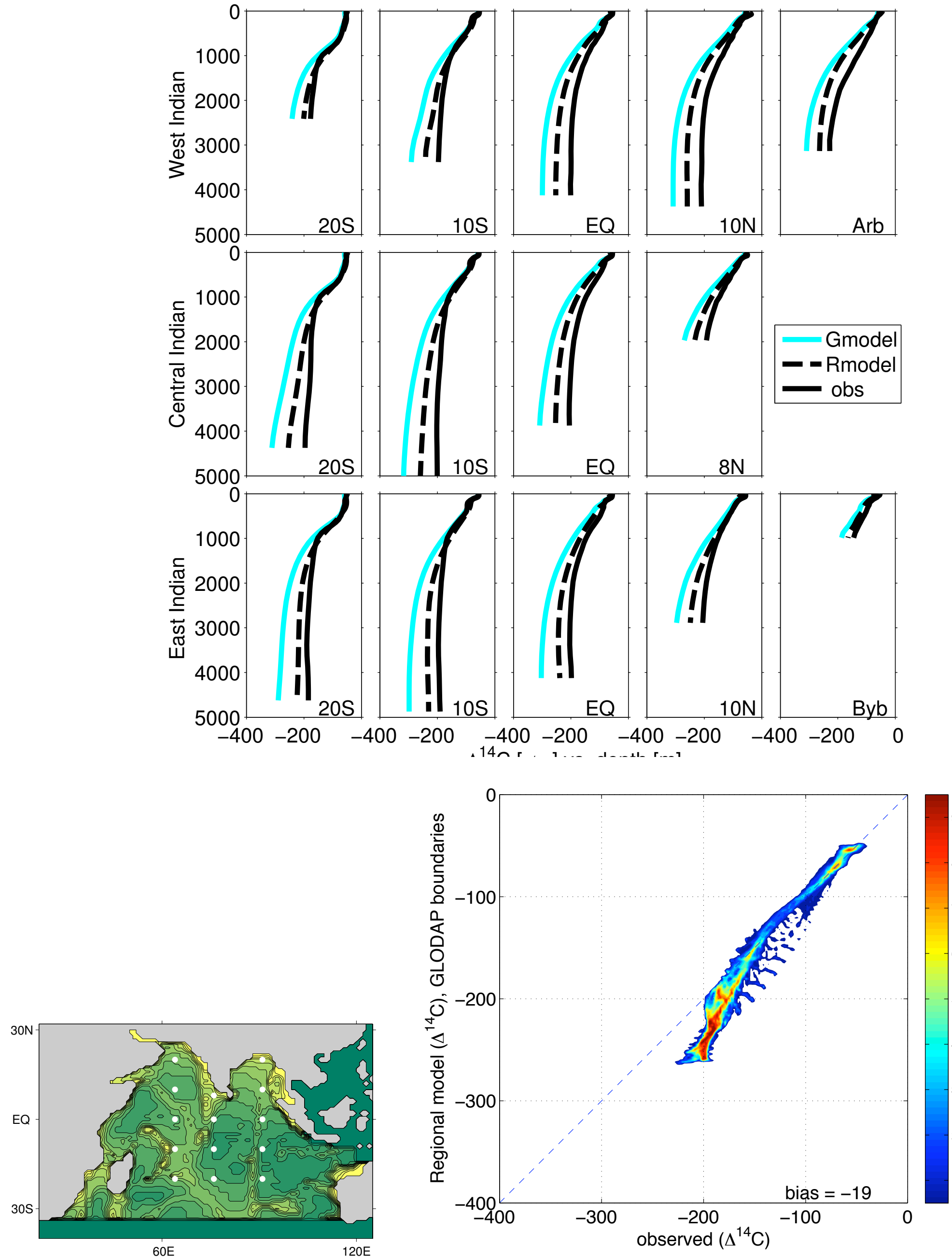

Figure 4.7: Results with the Southern Ocean boundary at 34S, and using GLODAP observations on the boundaries; moving the boundary was the only change in the conditions from the results shown in Figure 4.6. The top panel shows profiles of Δ^{14}C from the regional model (dashed, black); from the global model (solid,cyan), and from GLODAP prebomb observational data (solid, black); all versus depth. The bottom left panel shows the locations of the profiles as white dots on a background topographical map from the model. The bottom right panel is a scatter-density diagram of the regional model results versus GLODAP observations.

being too old. The results indicate that the $\Delta^{14}C$ substantial bias at depth did not increase above 10S; the bias remained fairly consistent looking northwards.

Southern boundary at 25S Putting the boundary northwards at 25S latitude, near the southern end of Madagascar, gave significantly better results throughout the basin. This puts the boundary north of the Southwest Indian Ridge on the west side of the opening with the Southern Ocean, and north of Broken Ridge on the east side. These results are shown in Figure 4.6. The 25S latitude boundary gives a startling improvement in the match with observations, not only close to the defined Southern boundary, as would be expected, but also all the way to the northern end of the Indian Ocean. The scatter-density diagram also shows improvement at the most negative end of the scale. There remains some bias, but it has improved from -19‰ for the 34S boundary to -12‰.

Southern boundary at 12S If the boundary is placed even further northwards at latitude 12S, near the top of Madagascar and beyond the Mozambique Channel, there is only a slight improvement in the results. Figure 4.8 shows profiles and the scatter density diagram for this case. The bias is not reduced, but the scatter-density diagram has a narrower band of points around the 1-to-1 line. Note that all of these boundaries are on the south side of the equator, so the equatorial effects are still captured.

Selection of southern boundary The 25S bottom-of-Madagascar Southern Ocean boundary definition was selected to define the region of interest for this study. Although using the 12S boundary gave somewhat less spread in the modeled results compared to the the GLODAP $\Delta^{14}C$ data, putting the boundary at 12S made the distinction between the ITF source waters and the Southern Ocean source waters inconclusive, and that is one of the factors to be studied.

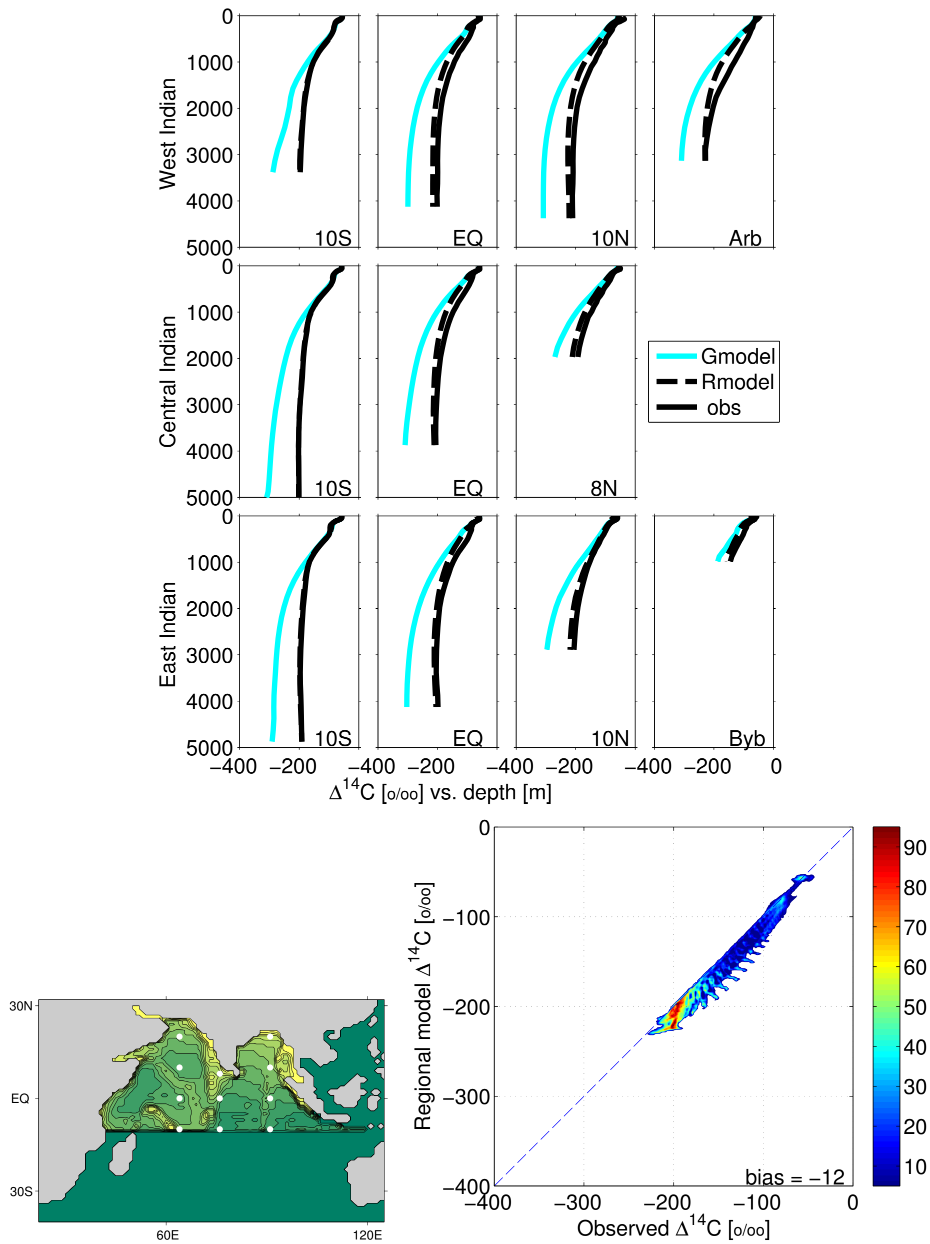

Figure 4.8: Results with the Southern Ocean boundary at 12S, and using GLODAP observations on the boundaries; moving the boundary is the only change in conditions from the results shown in Figures 4.6 and 4.7. The top panel shows profiles of Δ^{14}C from the regional model (dashed, black); from the global model (solid,cyan), and from GLODAP prebomb observational data (solid, black); all versus depth. The bottom left panel shows the locations of the profiles as white dots on a background topographical map based on the model. The bottom right panel is a scatter-density diagram of the regional model results versus GLODAP observations.

The $\Delta^{14}C$ shows minimal bias in the region thus defined, and it puts the boundaries well outside of the low oxygen regions of interest. It reduced our substantial concern with the biases in the circulation of the global ocean model, and the circulation influences on the biogeochemical processes being modeled. By localizing the circulation contribution to the result, concerns that the oxygen results are overwhelmed by the biases in the global circulation are minimized.

4.6 Impact of Boundary Conditions

How important is the source of oxygen from the Southern Ocean and ITF boundaries? These boundary values are being propagated into the region; how much influence do these boundary values have? There are two considerations to be made to address this issue.

First, how much difference is there in the oxygen concentration on the boundaries between the global BEC values and the WOA13 values? Figure 4.9 shows the O_2 on the boundaries with the Southern Ocean and the ITF from WOA13 observations; from the BEC global model values; and the difference. The major difference for both boundaries is that values of $[O_2]$ are too low in the upper layers, above 1000 m depth, and too high from 1000 m to 4000 m. While the difference pattern is the same for both boundaries, the ITF upper levels near Java and Sumatra are extremely low compared to the WOA13 gridded observations.

Second, what proportion of the water resident in the OMZs comes from each of these boundaries? How much comes from the Southern Ocean versus the ITF? To determine the sources of well-oxygenated waters, the ocean surface of the Indian Ocean is treated as an additional boundary and source of water for the OMZs. This provides a way to distinguish the more "remote" Southern Ocean and ITF from the more "local" surface effects. The ocean surface is a ventilation

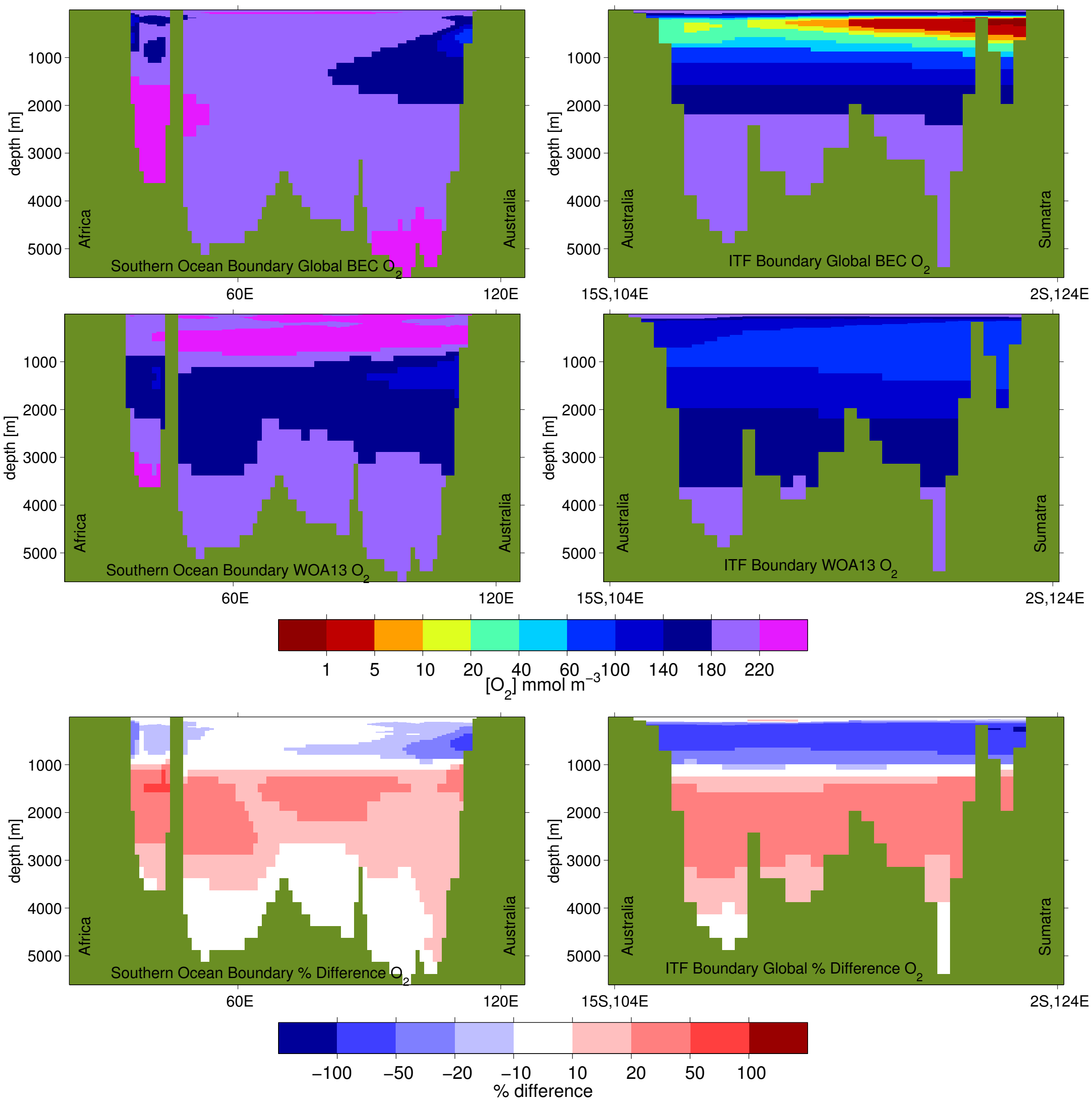

Figure 4.9: The $[O_2]$ on the Southern Ocean and ITF boundaries. The top panels show the BEC global solution $[O_2]$ values on the Southern Ocean boundary (left) and ITF boundary (right). The middle panels show the WOA13 $[O_2]$ values on the Southern Ocean boundary and ITF boundary. The bottom panels give the % difference for the BEC global values minus the WOA13 values for each of the boundaries. The ITF boundary is represented as a track along the boundary.

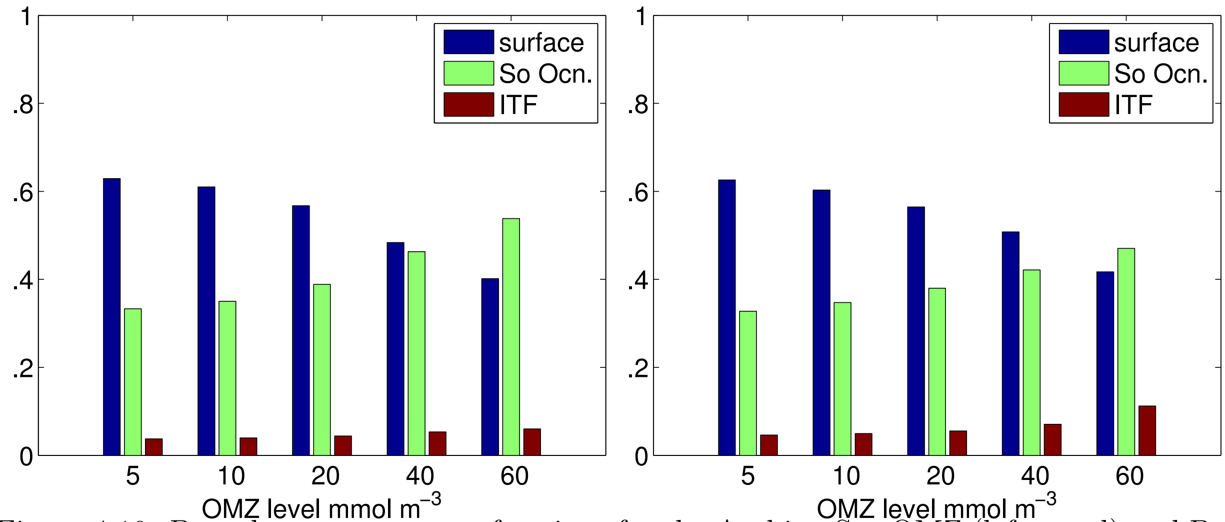

Figure 4.10: Boundary source water fractions for the Arabian Sea OMZ (left panel) and Bay of Bengal OMZ (right panel) The boundaries are the Indian Ocean surface, and the borders with the Southern Ocean and the ITF as shown in Figure 4.18.

source in the classic sense; for our purposes, the in-the-water boundaries are also treated as oxygen ventilation sources. We use the method described in Section 4.4.3 to perform the calculation.

Immediately notable in Figure 1.1 of Chapter 1 is that the core of the OMZ in the Arabian Sea, < 20 mmol m^{-3}, extends horizontally throughout the Arabian Sea, and across the northern part of the Bay of Bengal. Low oxygen levels of < 60 mmol m^{-3} extend from both the Arabian Sea and the Bay of Bengal to beyond the Equator. The proportion of the source water from each of the boundaries is calculated separately for the OMZ in the Arabian Sea and that in the Bay of Bengal. Further, because of the extensiveness of the low oxygen regions, the calculation is made for several defined levels of OMZ intensity in order to find out if the characteristic patterns are different: oxygen concentrations of less than 5, 10, 20, 40, and 60 mmol m^{-3}. The WOA13 observational data is used to define the various levels intensity of the OMZs.

A summary of the results for the Arabian Sea OMZ are shown in the bar chart in the left panel of Figure 4.10. The most striking feature is the proportion that comes from the surface: 63% for the most intense part of the OMZ, and still 40% at the 60 mmol m^{-3} level. The ITF provides only a small percentage and the balance is from the Southern Ocean. The results for the Bay of Bengal OMZ are shown in the right hand panel of Figure 4.10. The source percentages are quite similar to those for the Arabian Sea, but with a higher fraction from the ITF.

This result, with a substantial fraction of the oxygen supply coming from the surface, raises further questions about where on the surface is the water coming from? And where on that large expanse of the Southern Ocean boundary is the water coming from?

Figure 4.11 shows the surface origin of the source waters that ventilate the Arabian Sea OMZ levels of 5 mmol m^{-3} and 60 mmol m^{-3}; the $[O_2]$ levels between the two levels shown were similar. The source fractions are shown scaled to the maximum from any grid-cell on the boundary to allow visualization of the pattern. The areas where the source fraction is too small to be significant are set to light gray. The source water from the grid-cells at the entrance to the Persian Gulf dominate. Locations along the coast of India and Pakistan contribute. These surface sources are very local to the most intense part of the OMZ. The western side of the basin along the Somali coast also contributes. The 60 mmol m^{-3} zone also has its strongest surface source at the entrance to the Persian Gulf, but a larger contribution from the Somali coast. Both zones also show a source south of the Bay of Bengal, just north of the Equator.

The regional model shows ventilation into the OMZ from the surface, with the dominant location being the entrance to the Persian Gulf. The source at the entrance to the Persian Gulf shows very strong seasonal vertical diffusion, strongest in the Northeast Monsoon and Spring inter-monsoon, with nothing significant during the Southwest Monsoon (Figure 4.2). This finding is in contrast with both that of Fine et al. (2008), where it was found that neither the Persian Gulf

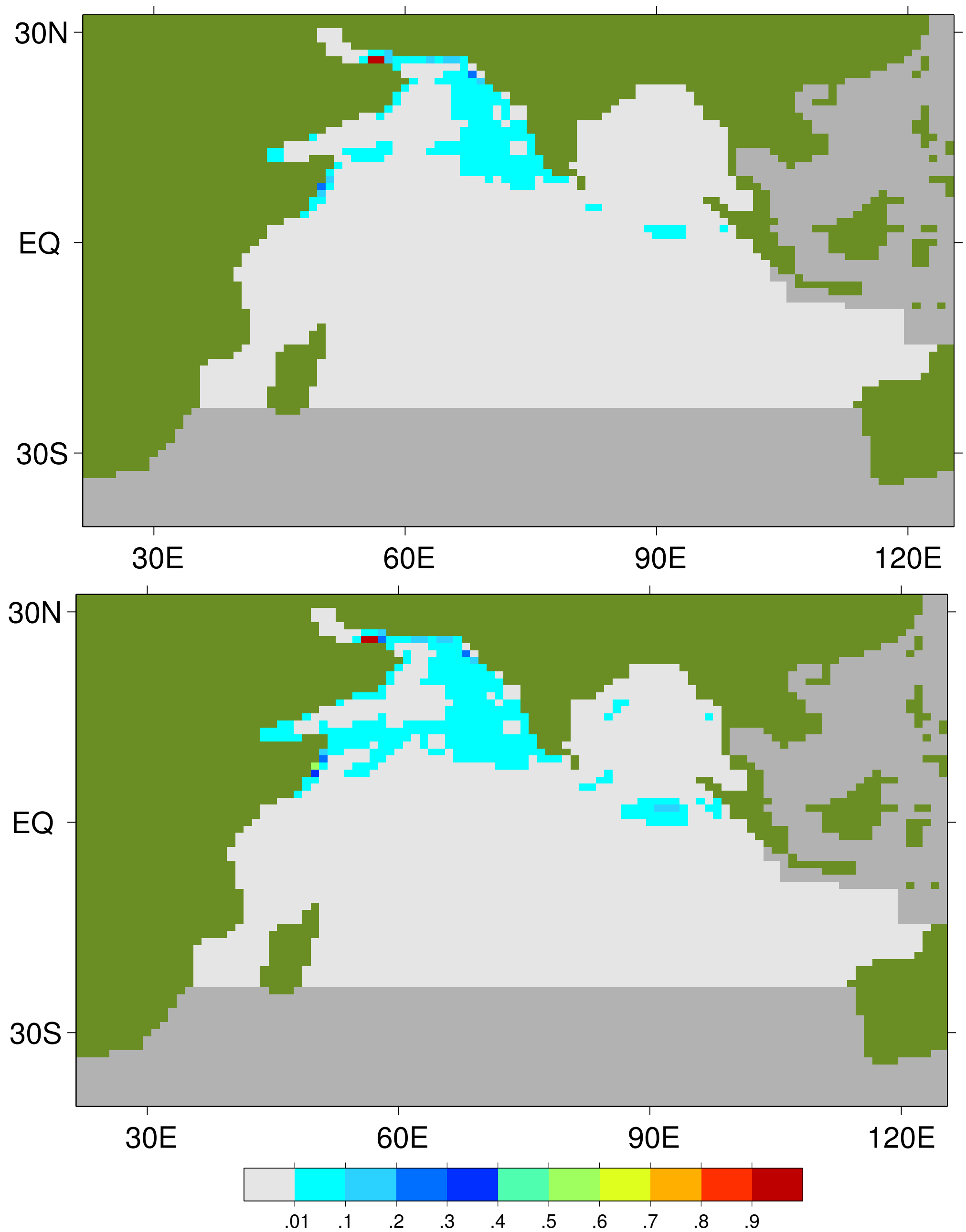

Figure 4.11: Arabian Sea OMZ with $[O_2]$ of < 5 mmol m^{-3} (top panel) and < 60 mmol m^{-3} (bottom panel) Indian Ocean surface source. This is shown proportional to the maximum grid-cell source for this boundary.

nor the Red Sea were major contributors to the ventilation of the Arabian Sea OMZ based on CFC concentration distributions; and of Beal et al. (2003), where the Red Sea was thought to be a major source for a deeply ventilated water column in the Arabian Sea.

Figure 4.12 shows the surface source waters that ventilate the Bay of Bengal OMZ. The sources for the 5 mmol m^{-3} and the 60 mmol m^{-3} zones differ only in detail. Both have a major source just north of the Equator. The surface area of the whole Bay of Bengal is also a source, but more distributed. There are small sources along the coasts as far away as the entrance to the Persian Gulf.

The strong surface source south of the Bay of Bengal, just north of the Equator is most notable. Several previous studies of Indian Ocean circulation (for example, Morrison et al. (1999); Schott et al. (2002)) have mentioned Ekman pumping as a source for sub-surface water. In Figure 4.1, the downwelling just north of the Equator is conspicuous during the Fall inter-monsoon, shown for November. However, examination of the meridional and zonal components of advection, shown in Figures 4.4 and 4.3, show a strong convergence in the zonal direction, and a weak divergence in the meridional direction at that location. Vertical diffusion, shown in Figure 4.2, while not strong is non-zero. It seems more likely that this is an area of turbulent flow, with the zonal convergence dominating, that would explain the strong surface source waters at that location particularly in that season.

There are more distributed surface oxygen ventilation sources close to the OMZs, as seen in Figures 4.11 and 4.12. Figure 4.1 shows seasonal periods of both downward and upward advection. In the northern Arabian Sea, downward advection prevails, except during the Southwest Monsoon, when there is significant upwelling along the coasts. This is in general agreement with (Morrison et al. (1999) and Schott and McCreary (2001)), in which they found the downward

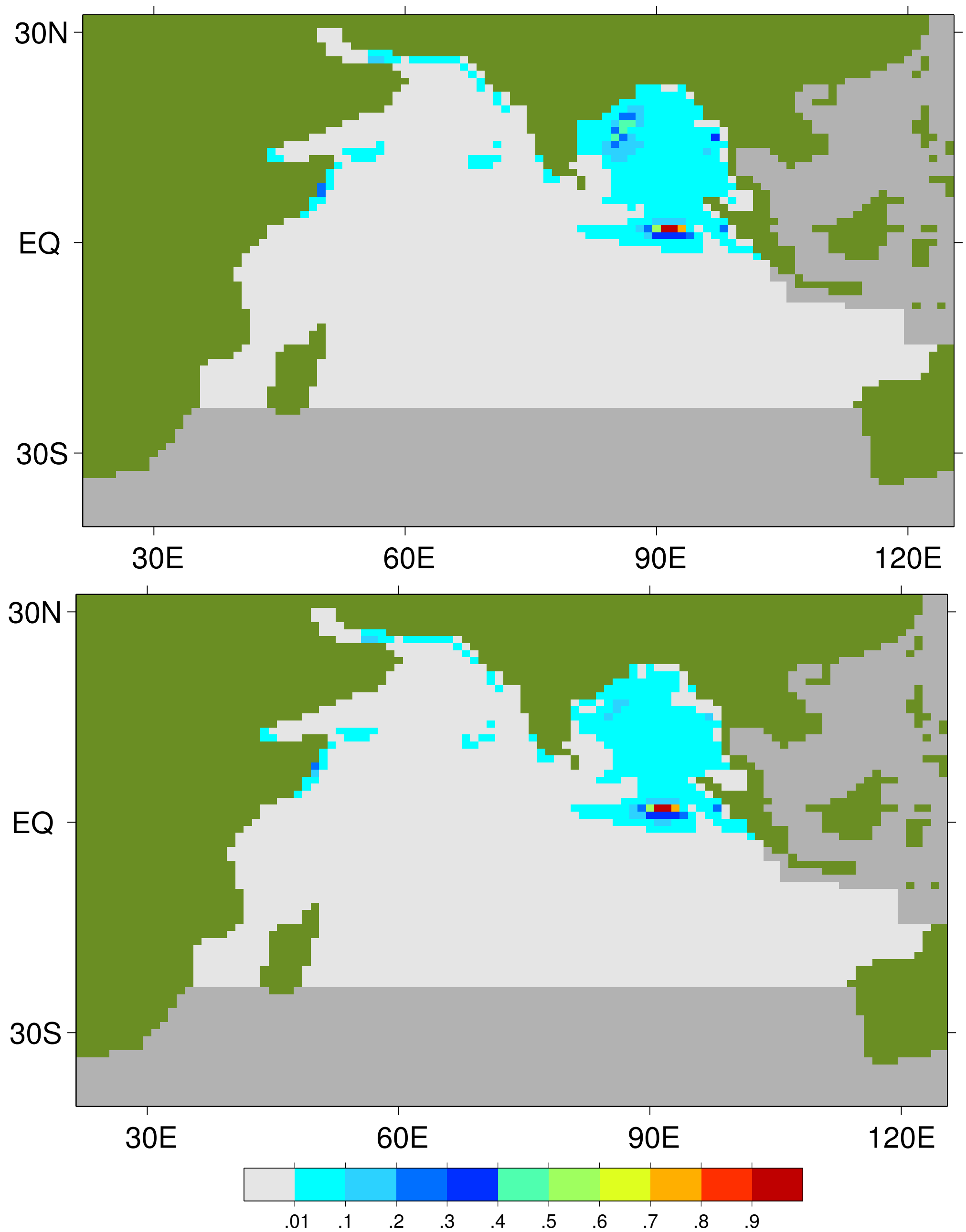

Figure 4.12: Bay of Bengal OMZ with $[O_2]$ of < 5 mmol m^{-3} (top panel) and < 60 mmol m^{-3} (bottom panel) Indian Ocean surface source. This is shown proportional to the maximum grid-cell source for this boundary.

advection occurs strongest in the Northeast Monsoon. During the Southwest Monsoon, shown for August, along the Somali coast there is strong vertical advection in both directions. The Bay of Bengal is a mix of upward and downward advection that changes with the monsoonal season. Upwelling dominates only during the Southwest Monsoon and even then it is weaker than in the Arabian Sea.

Figure 4.13 shows the origin on the southern boundary of the source waters that ventilate the Arabian Sea OMZ. The source is clearly not evenly distributed, but focused on two areas. The first is the deep western boundary current, in the channel west of Madagascar, where the flow is to the north, in the opposite direction from the surface western boundary current. The second focused area is on the eastern side of the basin, centered around 500 m depth, and is probably from Sub-Antarctic Mode Water (SAMW), which is known for its maximum oxygen content from forming by deep convection rather than subduction at 40S to 50S. The deep water, below about 1000 m, hugs the western side of the basin, in contrast to the shallower SAMW, which comes in on the eastern side, just west of Australia. The notable difference between the source for 5 mmol m^{-3} zone and the 60 mmol m^{-3} zone is a shift from the major portion coming from the SAMW for the 5 mmol m^{-3} zone to a higher portion coming from the deep western boundary current for the 60 mmol m^{-3} zone. It is also interesting to note that some of the southern boundary source water comes from all depths; it is not limited to the depths of the OMZ. This is in contrast to an image of the water chiefly traveling along isopycnals.

Figure 4.14 shows the origin of the ventilation source waters from the southern boundary for the Bay of Bengal OMZ for $[O_2]$ levels of 5 mmol m^{-3} and 60 mmol m^{-3}. The 5 mmol m^{-3} source water patterns are similar to those for the Arabian Sea OMZ, but with a higher proportion coming from the SAMW, and less from

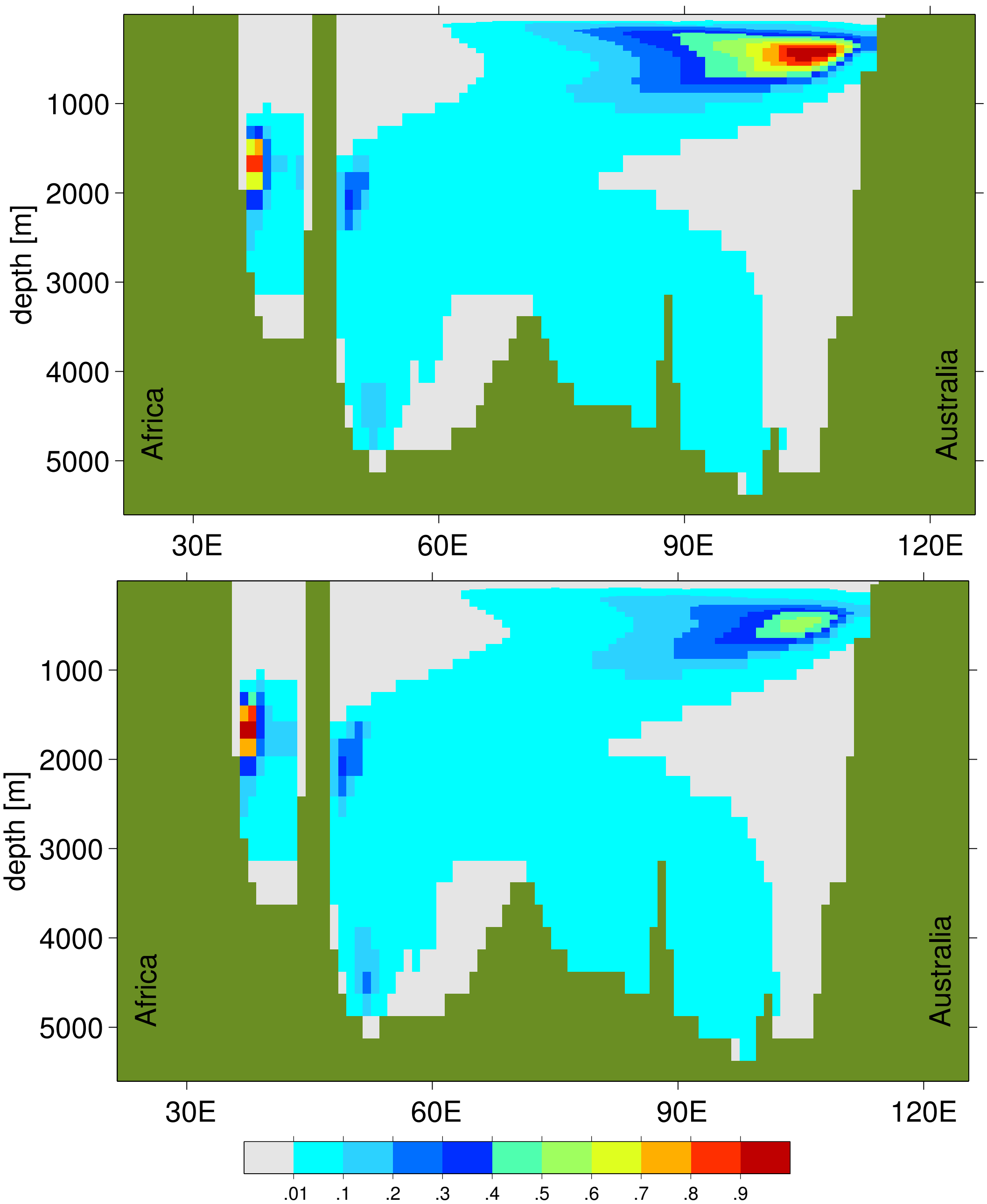

Figure 4.13: Arabian Sea OMZ with $[O_2]$ of < 5 mmol m^{-3} (top panel) and < 60 mmol m^{-3} (bottom panel) Southern Ocean source. This is shown proportional to the maximum grid-cell source for this boundary.

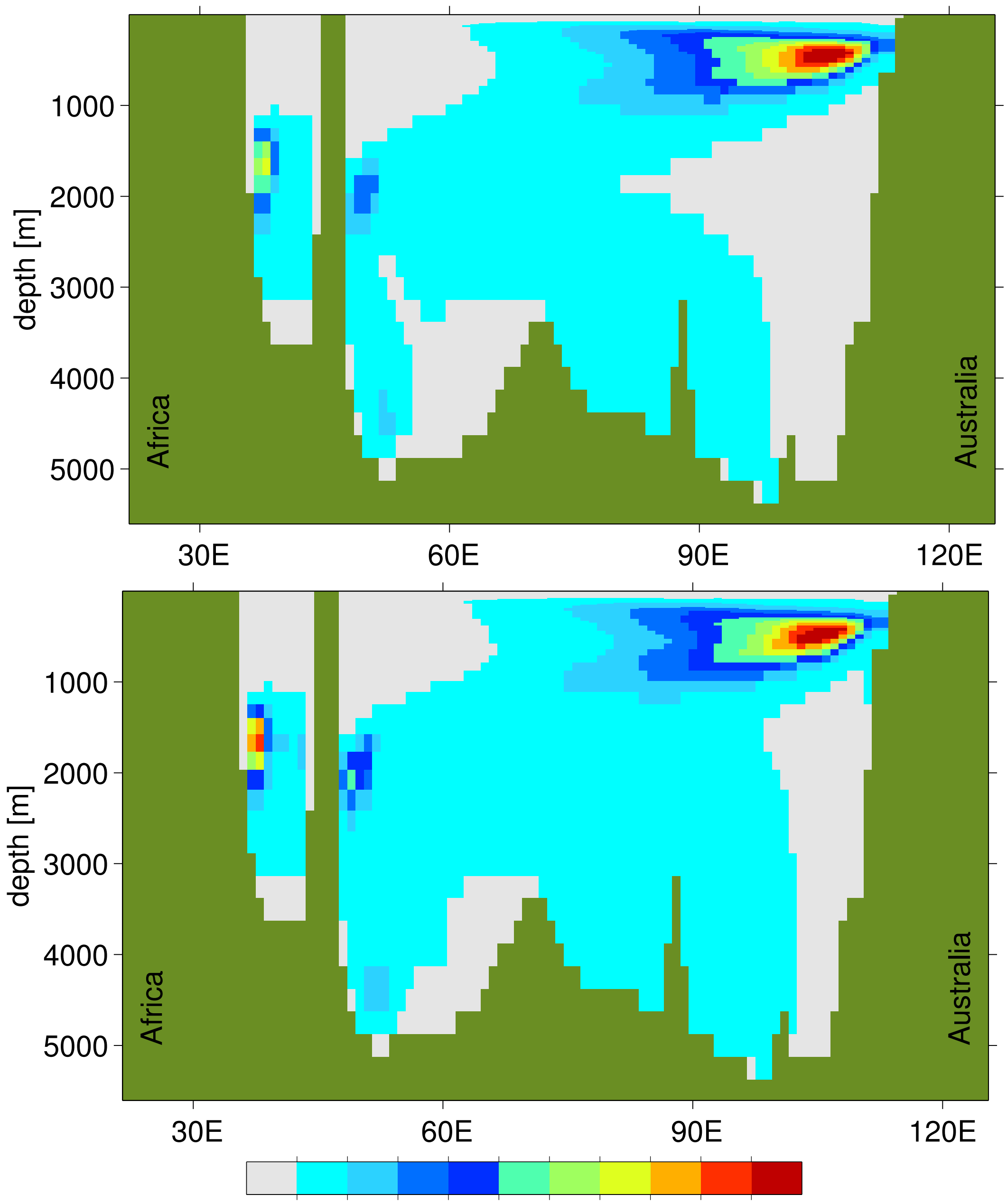

Figure 4.14: Bay of Bengal OMZ with $[O_2]$ of < 5 mmol m^{-3} (top panel) and < 60 mmol m^{-3} (bottom panel) Southern Ocean source. This is shown proportional to the maximum grid-cell source for this boundary.

the deep western boundary current. There is also a source from a deep western boundary current on the eastern side of Madagascar. The source for the 60 mmol m^{-3} zone is similar, but shows a relatively stronger source from the deep western boundary currents on both sides of Madagascar.

What does not appear on the southern boundary for either OMZ is any significant source from Antarctic Bottom Water (AABW), which is contrary to expectations based on observations (for example, Swallow and Pollard (1988) and Fine et al. (2008)). To understand whether this reflects the lack of production in the Southern Ocean in the model, or that the AABW does not extend this far north, refer back to Chapter 3 where a global analysis of ventilation sources was made. Figure 3.5 of Chapter 3 shows the zonal average fraction of the water from the Southern Ocean extending into the Indian Ocean. The dividing line between the two oceans for the Chapter 3 analysis was at the tip of Africa. Figure 3.10 in Chapter 3 shows the zonal average fraction of the water ventilated from the surface of the Indian Ocean. The Southern Ocean contribution into the Indian Ocean basin is significant in the subsurface and mid-ocean depths, but there is little Southern Ocean surface ventilated water that is present in the bottom of the Southern Ocean. This is due to a lack of formation of AABW in the model. The waters at the bottom of the Southern Ocean are dominated by the mixing in of waters ventilated in the North Atlantic (shown in Figure 3.11 in Chapter 3). The zonal average for the Indian Ocean shows deep ventilation at the northern end, where the OMZs are, but no significant extension into the Southern Ocean. This confirms the picture of the Southern Ocean as a minor contributor to the waters above 1000 m in the northern end of the Indian Ocean.

The Southern Ocean boundary showed a strong source from the Southern Ocean in SAMW waters at about 500 m depth (Figures 4.13 and 4.14). In the global ventilation study in Chapter 3, Figure 3.6 provides layer views of the source fractions at 500 m and 1000 m for the Southern Ocean. At 500 m, the Southern Ocean source is dominant south of the Equator, but not north of the Equator. At 1000 m, however, the Southern Ocean dominance extends further, although it is not dominant in the Bay of Bengal and the Arabian Sea. This is in general agreement with Tomczak and Godfrey (2003), who found that the AAIW was blocked by the equatorial system from extending further north.

The influence of the oxygen concentrations on the boundaries is due to the combination of the the boundary oxygen levels and the fraction of the boundary waters that becomes resident in the OMZ. Figure 4.15 convolves the oxygen concentration on the boundaries with the fractions of water containing those concentrations, for the Arabian Sea OMZ. The surface contribution to all oxygen concentration levels of the OMZ has two peaks: the lower peak at about 170 mmol m^{-3} matches the surface values at the entrance of the Persian Gulf. The oxygen levels from the southern boundary vary from about 150 to 250 mmol m^{-3}. The ITF has much lower values, but a very small contribution.

Figure 4.16 shows the equivalent information for the Bay of Bengal OMZ. There is one major peak for the values at the surface, as would be expected. The values on the southern boundary have an outline similar to that for the Arabian Sea. But the ITF low values for the 60 mmol m^{-3} OMZ level make a more significant contribution than was seen for the Arabian Sea. Still, the overwhelming majority of the water from the boundaries is between 150 to 250 mmol m^{-3}.

With these oxygen sources on the boundaries, we can infer that the low oxygen concentrations found in the OMZs are primarily the result of local biological action. The challenge for the biological models is to simulate the environment in which the oxygen production and consumption can balance the supply. Clearly, there is a dependence on the circulation as an important part of the environment, and a factor to be taken into account by the biological model.

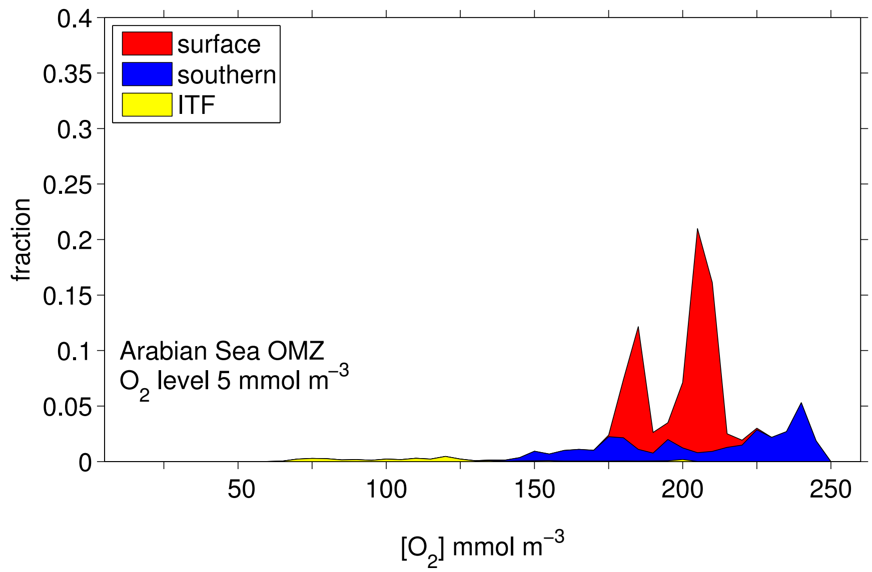

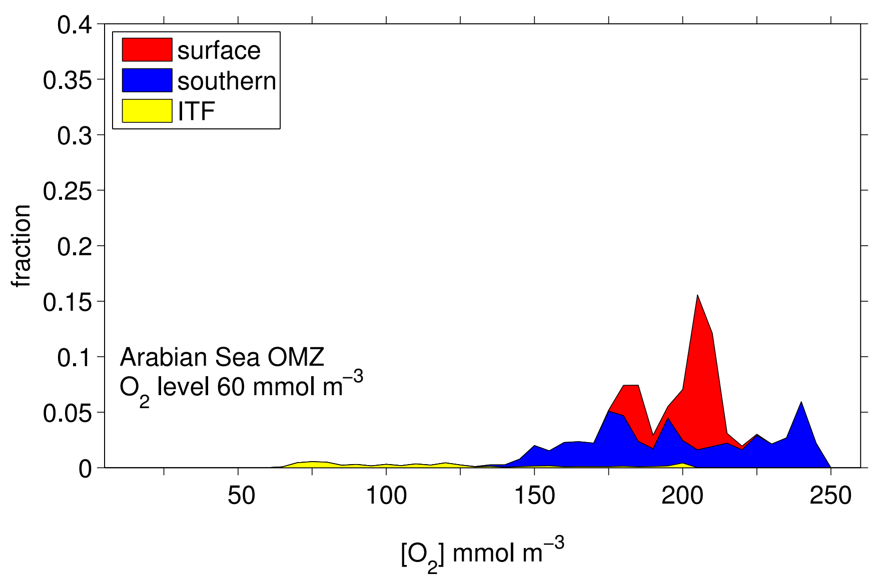

Figure 4.15: Boundary source oxygen concentrations versus fractions of the water containing the given oxygen concentration that is resident in the Arabian Sea OMZ. The fractions for the OMZ oxygen concentration level of less than 5 mmol m^{-3} is shown in the top panel, and for less than 60 mmol m^{-3} in the bottom panel. The intermediate oxygen concentration levels had similar configurations. The boundaries are the Indian Ocean surface, and the borders with the Southern Ocean and the ITF.

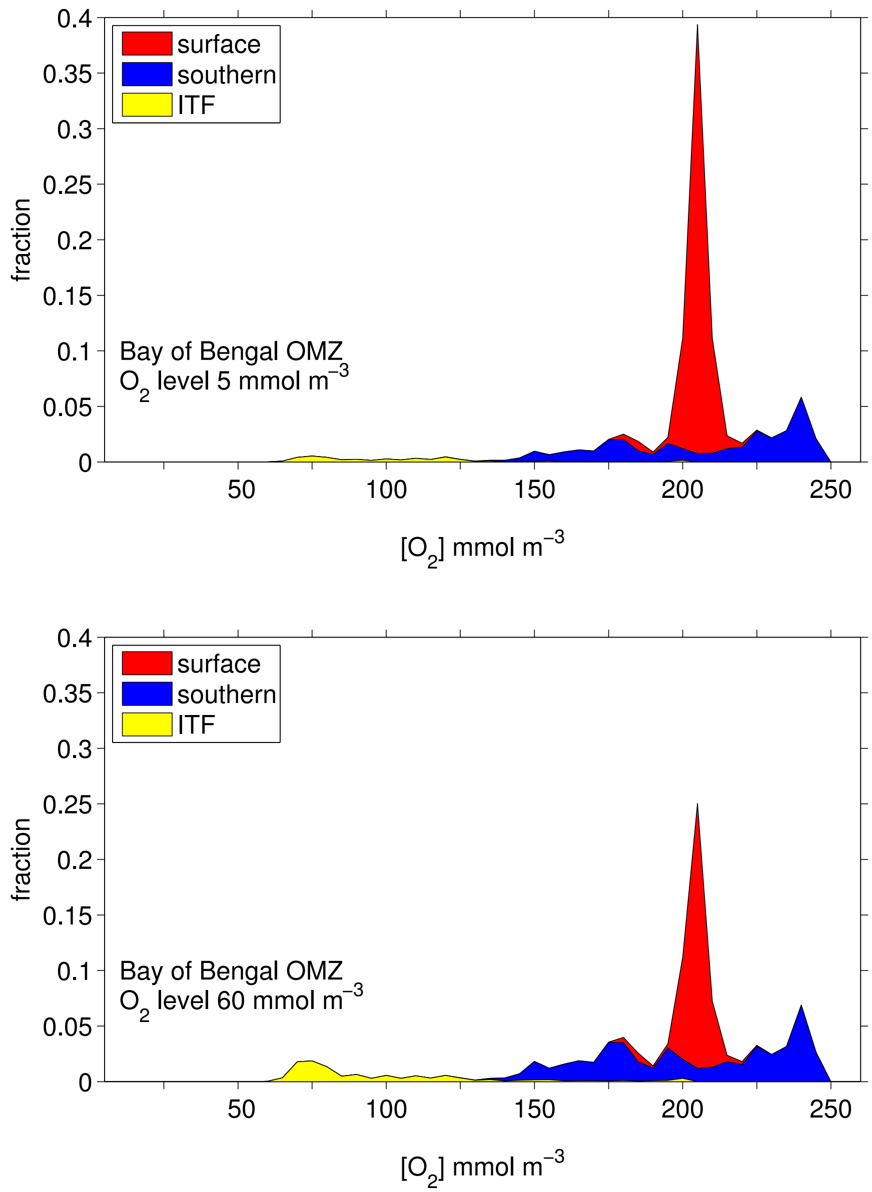

Figure 4.16: Boundary source oxygen concentrations versus fractions of the water containing the given oxygen concentration that is resident in the Bay of Bengal OMZ. The fractions for the OMZ oxygen concentration level of less than 5 mmol m^{-3} is shown in the top panel, and for less than 60 mmol m^{-3} in the bottom panel. The intermediate oxygen concentration levels had similar configurations. The boundaries are the Indian Ocean surface, and the borders with the Southern Ocean and the ITF.

4.7 Regional Oxygen Simulation Results

In the first regional simulation with the BEC biological component incorporated, global BEC [O_2] values were placed on the boundaries. The results are compared with the previously obtained global BEC results from the CMIP5 simulation.

Figure 4.17 shows profiles and a scatter-density diagram comparing the resulting [O_2] annually-averaged values for the region. The global BEC [O_2] values and the offline regional [O_2] values do not match as well as the $\Delta^{14}C$ equivalent comparison did. This is primarily due to changes in the circulation resulting from differences in the forcings used and spin-up methods. The offline regional model shows improvements in the excessive low [O_2] values found in the global BEC solution above 1000 m, and generally fall between the WOA13 values and the global BEC solution values. While the global BEC volume-averaged bias of 13 mmol m^{-3} is not particularly large, the spread of the 1-to-1 line is. The largest values, around 200 mmol m^{-3}, are too big, while the lowest values are too low, resulting in much bigger volumes for the OMZs. This characteristic of over-sized OMZs was reported in Moore et al. (2013). The regional model with global BEC boundaries has reduced the volume-weighted bias, but retains the global BEC characteristics of too large high [O_2] values, and too small low [O_2] values.

To determine how much of the bias in oxygen concentration is from outside the region versus produced locally, in the second regional simulation we use observational values of [O_2] on the Southern Ocean and ITF boundaries. Figure 4.18 shows profiles and a scatter-density diagram of the results. In the profiles, only the dashed line for the regional model results is changed from Figure 4.17. The regional model results are in good alignment with the observations. On the scatter-density diagram, the 1-to-1 line of observations vs regional model results is much narrower, with a good match for higher values of [O_2], above 150 mmol

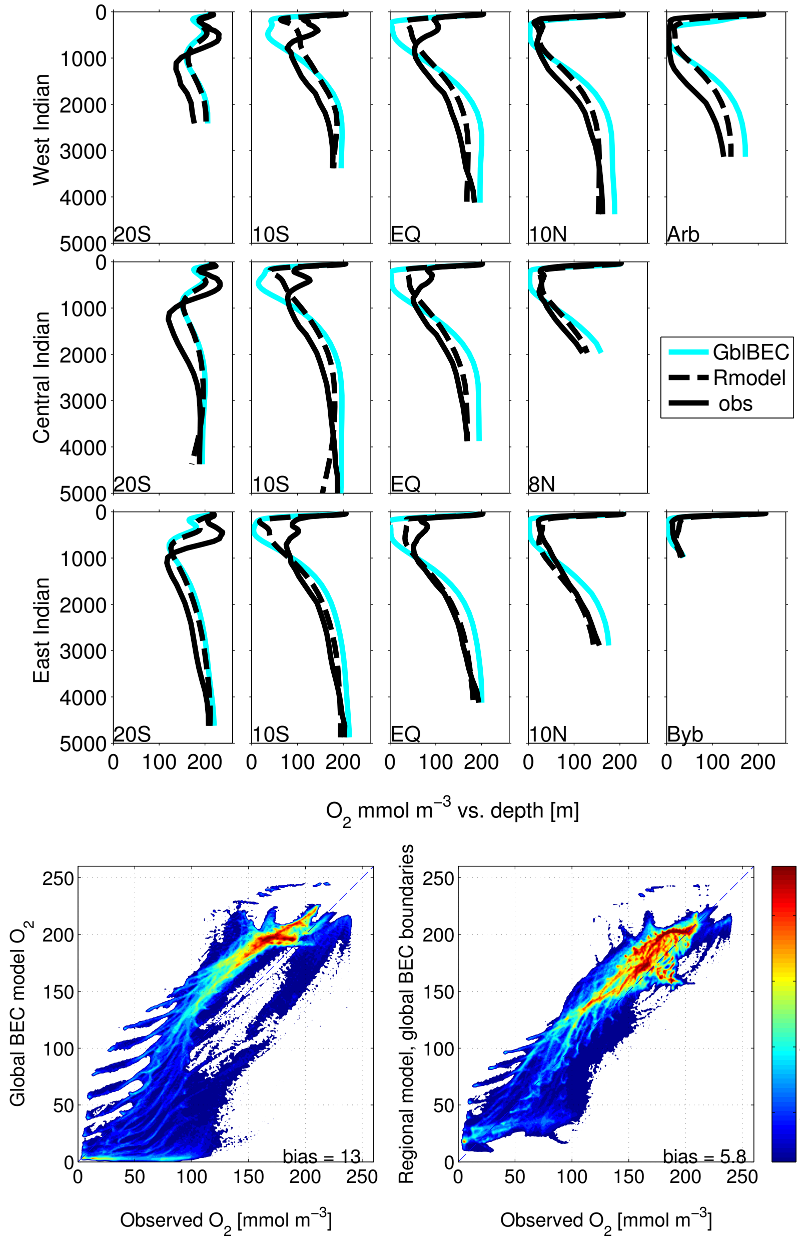

Figure 4.17: The [O_2] results for the regional model with global BEC modeled [O_2] values on the boundaries. The top panel shows profiles of [O_2] from the regional model (dashed, magenta); from WOA13 observational data (solid, black); and from the global BEC modeled oxygen (solid, cyan); all versus depth. The locations of the profiles are the same as shown on Figure 4.6. In the bottom left panel is a scatter-density diagram of the global BEC [O_2] results versus WOA13 [O_2] observations for the Indian Ocean region. The bottom right panel is a scatter-density diagram of the regional model results using the global BEC [O_2] values on the boundary, versus WOA13 observations.

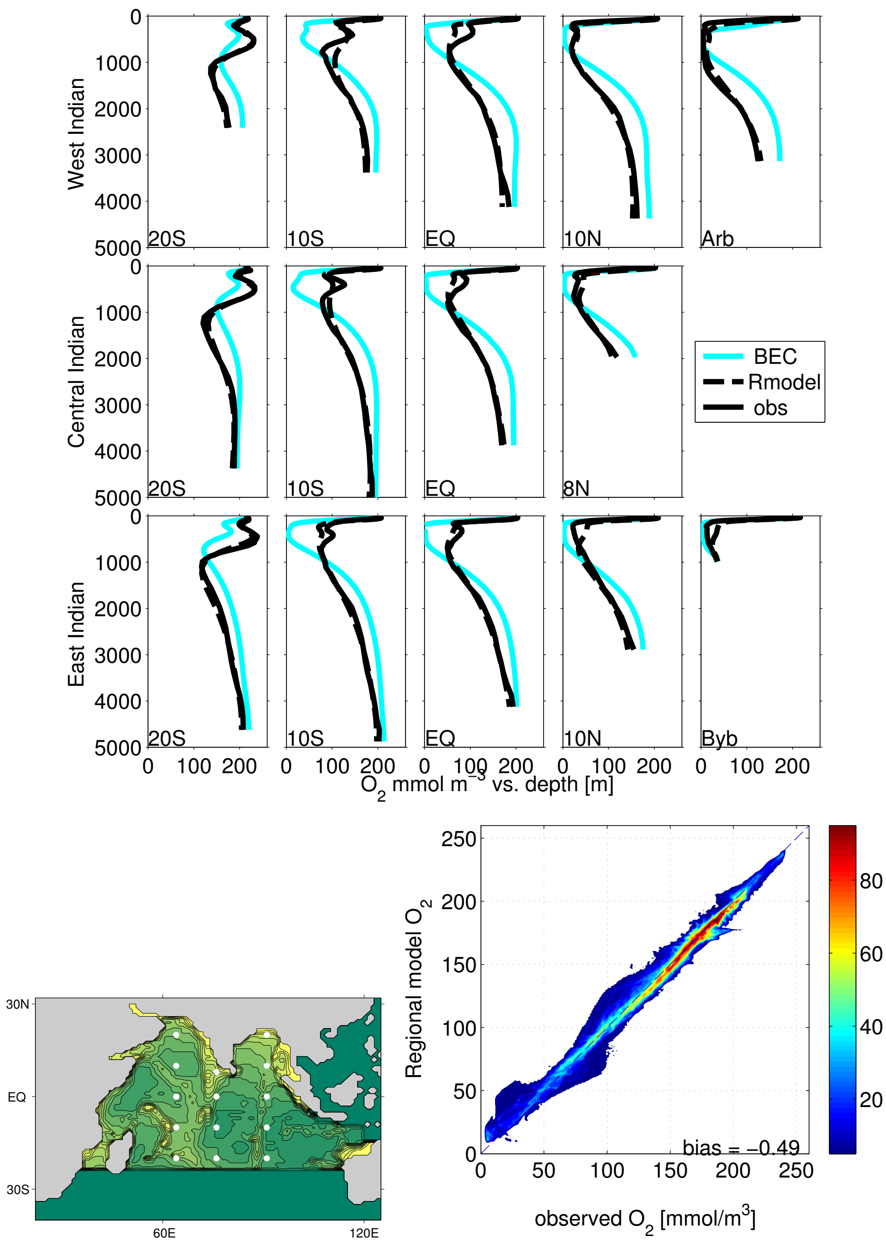

Figure 4.18: The $[O_2]$ results for the regional model with WOA13 $[O_2]$ values on the boundaries. This is the configuration used for the rest of the study. The top panel shows profiles of $[O_2]$ from the regional model (dashed, black); from WOA13 observational data (solid, black); and from the BEC modeled oxygen (solid, cyan); all versus depth. The bottom left panel shows the locations of the profiles as white dots on a background topo map. In the bottom right panel is a scatter-density diagram of the regional model results versus WOA13 observations. Compare with Figure 4.17.

m^{-3}, and some room for improvement below that level. The excessive volume of low-oxygen concentrations is gone. Deviations from observations are from the biological activity and the physical circulation inside of the region of study, because the region has been effectively isolated, with observational values on the boundaries.

Figure 4.19 provides section views of the regional solution $[O_2]$ values, and compares them with the WOA13 O_2 values, for the Arabian Sea. While the lower layers, below 2000 m, show good agreement, the regional model does not capture the intensity of the OMZ. Figure 4.20 provides section views for the Bay of Bengal from the regional model and a comparison with the WOA13 O_2 values. The figure shows good agreement between the regional model solution and the observations, but, again, missing the intensity in the core of the OMZ.

To see how the regional model and WOA13 observational $[O_2]$ agree and differ at the depths with minimum $[O_2]$ values, Figure 4.21 gives model to observational data comparisons at depths of 200 m and 600 m. These particular depth levels were chosen for display because they demonstrate the problems in modeling the OMZs. The observations show a more intense OMZ in the central Arabian Sea, and off the coast of India than is seen in the regional model. The regional model shows lower values of $[O_2]$ along the Somali Coast and adjacent to the Red Sea. The Bay of Bengal also has less intensity in the regional model than is indicated by the WOA13 values. The results for the regional model using global BEC $[O_2]$ values on the boundary are also shown. The generally lower $[O_2]$ levels across the Indian Ocean basin are noticeable, with levels of < 20 mmol m^{-3} at the 200 m depth levels near Sumatra. The intensity of the OMZ in the central Arabian Sea is missing.

We found that there remain differences between the regional results and observations primarily in 1) the formation of a low oxygen region along the coast of

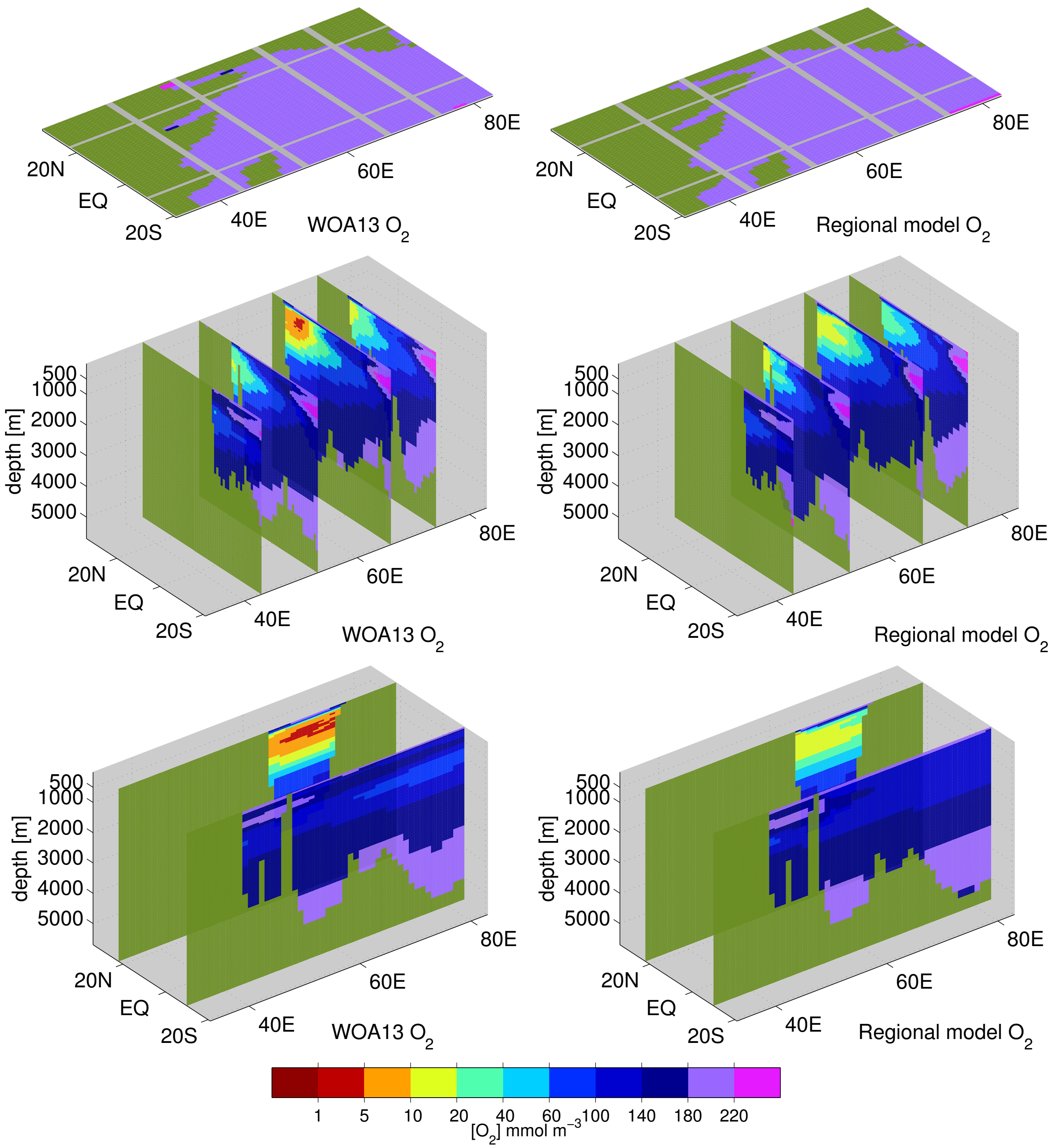

Figure 4.19: The $[O_2]$ in the Arabian Sea. On the left are sections showing WOA13 observational values. On the right are sections showing the regional model solution values. The surface values, in the top panels, have lines showing where the sections were taken.

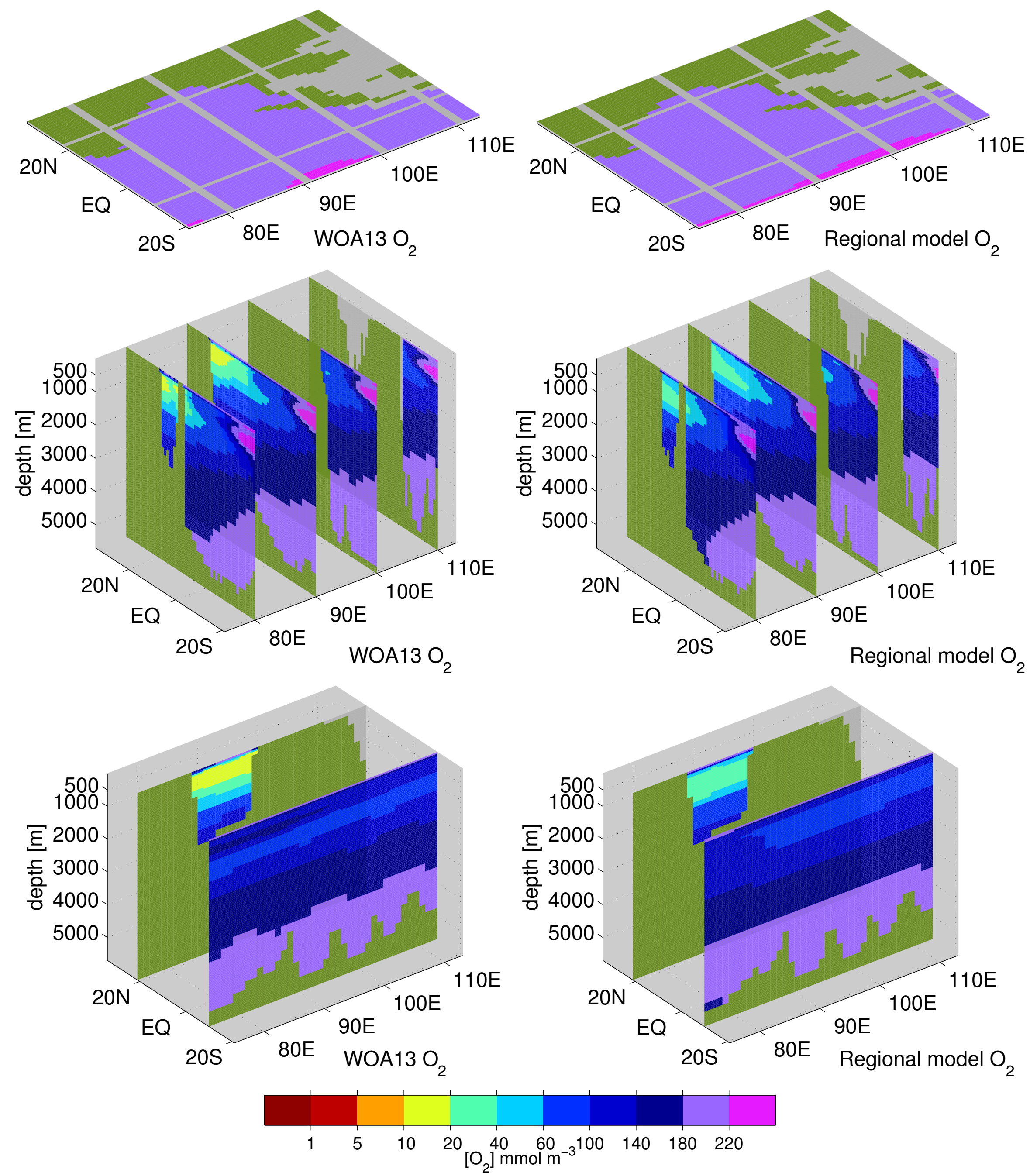

Figure 4.20: The $[O_2]$ in the Bay of Bengal. On the left are sections showing WOA13 observational values. On the right are sections showing the regional model solution values. The surface values, in the top panels, have lines showing where the sections were taken.

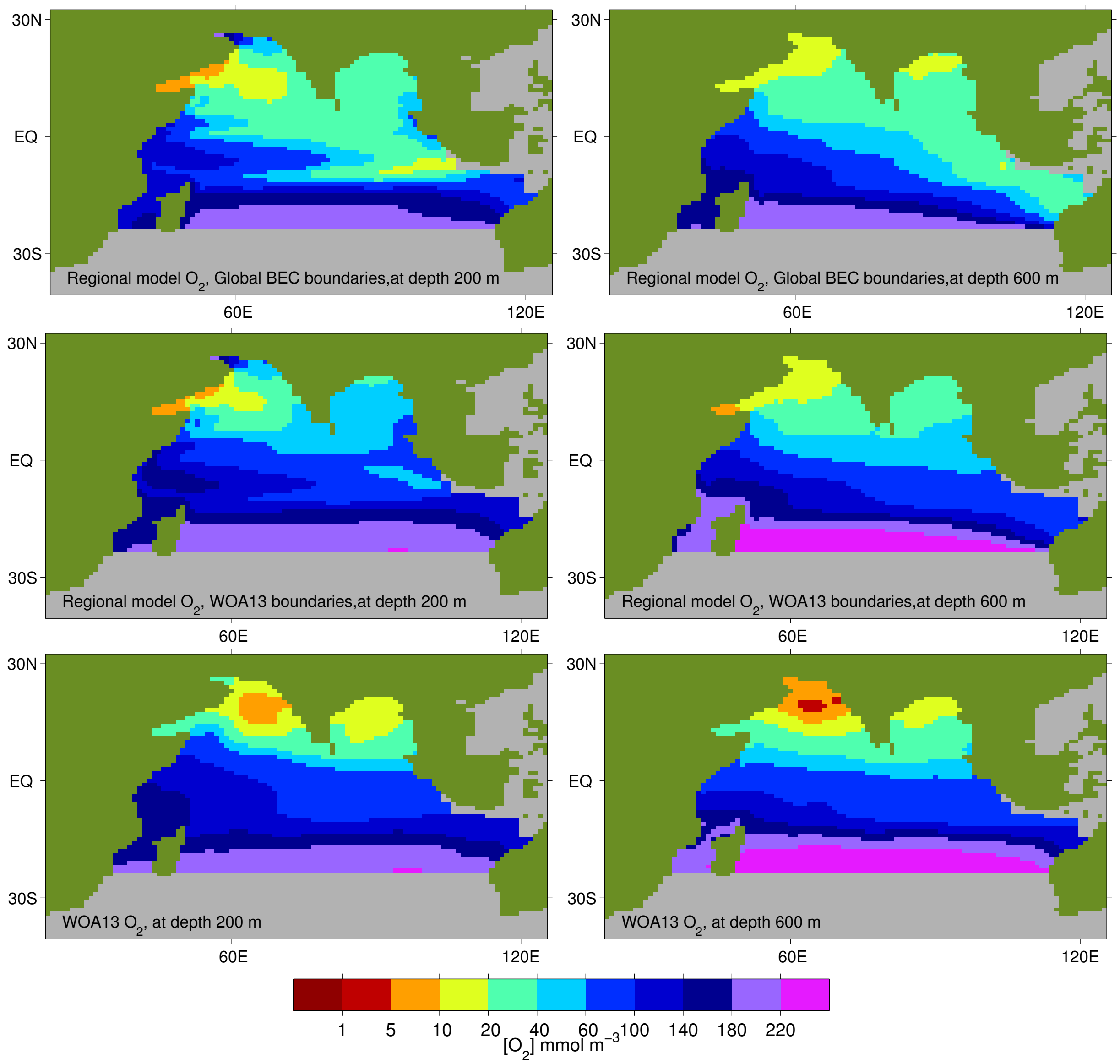

Figure 4.21: The $[O_2]$ in the layers at 200 m and 600 m, comparing the regional model with global BEC $[O_2]$ on the boundaries (top panels); the regional model with WOA13 $[O_2]$ on the boundaries (middle panels); and WOA13 observational $[O_2]$ values for the region (bottom panels).

Somalia; 2) in a shift from the east side of the Arabian Sea to the west side for oxygen levels of less than 10 mmol m^{-3}; and a lack of intensity of the OMZ in the both the Arabian Sea and the Bay of Bengal.

4.8 Discussion and Conclusions

We have demonstrated an approach to making a regional seasonally-cycling offline ocean model, based on the global offline model. The regional ocean boundaries can be populated with observational data, and appear to the interior regional ocean to be connected to the global ocean because of active advection and diffusion fields on the boundary. This is a useful mechanism to isolate the interior regional circulation from the remainder of the global ocean, and the regional biogeochemical model from the effects of the biogeochemical model outside of the region. This approach can be used to gain insight into regions of the ocean of interest, without having to deal with the entire ocean, and to discriminate between biases that develop inside and outside of the region.

A regional offline ocean model was built for the Indian Ocean basin. It was determined that the latitude at which the boundary with the Southern Ocean was placed made a difference in the results. The appearance of sluggishness in the circulation in the vicinity of 30S, for whatever reason, meant that the boundary needed to be set above that latitude in order to be able to study the northern Indian Ocean, where the OMZs are located, without having the results unfavorably skewed away from observations. This suggests that limiting the domain may be a helpful diagnostic for identifying geographical areas with problems in the circulation.

The amount of the oxygen ventilation from the boundaries into the OMZs was determined. Our analysis showed the somewhat surprising result that the surface, considered as a boundary, was a bigger contributor than either the Southern Ocean or the ITF for the most intense part of the OMZs. This was true for both the Arabian Sea and the Bay of Bengal, although the surface locations within the basin for the most intense surface sources were different. In the less intense part of the OMZs, less than 60 mmol m^{-3}, which extends further south in the basin, the southern boundary becomes the dominant contributor. We infer that the basis for maintenance of the OMZs is the lack of horizontal flows into the OMZ under a highly seasonal productive surface. It is also interesting to note that the southern boundary oxygen ventilation source is largest from SAMW coming in next to Australia, and from the deep western boundary current in the Mozambique Channel. Only the SAMW source is at about the same depth as the OMZs. The rest of the source water from this boundary must be arriving in the OMZ mostly by means of diffusive tendencies or convective mixing.

An oxygen regional model was built using oxygen production and consumption as calculated by the BEC. Using this model the Indian Ocean oxygen fields and the OMZs were examined. The resulting oxygen fields were a much better match to observations within the region when oxygen observations were placed on the boundaries, than when the global BEC solution boundary values were used. This leads to the conclusion that the bulk of the bias in the Indian Ocean are from circulation and/or BEC calculations that are external to the Indian Ocean. From the experiment with ^{14}C in the regional context, we found that the ^{14}C results were substantially better in the regional model with observations on the boundaries. Since there is not a biological component to the ^{14}C, the results lead to the conclusion that the circulation outside of the basin in the deep ocean, is the main culprit. It follows that this is also a major effect for the oxygen results.

With the external circulation influences removed, the oxygen results were examined, focusing on the OMZs. The general agreement with observations in the profiles is encouraging. There remain differences between the regional results and observations primarily in 1) the formation of a low oxygen region along the coast of Somalia; 2) in a shift from the east side of the Arabian Sea to the west side for oxygen levels of less than 10 mmol m^{-3}; and a lack of intensity of the OMZ in the both the Arabian Sea and the Bay of Bengal. The first two of these differences may be partially due to insufficient seasonal northwards flow at the same time that the upwelling is occurring along the coast, and/or due to the BEC algorithm of remineralization of particulate organic matter in the water-column immediately below the surface layer where it is produced, regardless of the speed of the current. Several studies (Tomczak and Godfrey, 2003; Resplandy et al., 2011; McCreary et al., 2013), have commented on the importance of the seasonally upwelled nutrients and the detritus produced in this area being swept northward and into the Arabian Sea.

The insights gained from this analysis leads to a recommendation to use a validated regional model to examine the parameterization of the biological model. The framework provides a mechanism for the separation of concerns between local and remote influences in determining the biological parameters and model configuration. The biases from outside the region of interest are eliminated. As a practical matter, it should be noted that time-stepping the regional model, the equivalent of OCMIP2 convergence criteria for ^{14}C (1 part in 10^6 for 98% of the volume) can be achieved in 408 model years without using a Newton-Krylov solver. This compares favorably with the more than 4000 model years (Orr, 2002) for time-stepping a prognostic global model for ^{14}C, which has a smoother path to convergence.

Future research subjects recommended based on this study include further investigation into the parameterization of the biological model in the production and consumption of oxygen, particular in the low oxygen regions, and the effects of the seasonality of the sources of oxygen ventilation source water. Further consideration of the age of the water within the region may reveal additional factors on the influence of the circulation within the region on oxygen levels.

Chapter 5

Conclusions

5.1 Overview

Throughout this dissertation, there has been a focus on developing and applying new tools — mathematical methods — for diagnosing the characteristics and behavior of ocean models. The focus of Chapters 2 and 3 was on the characteristics of the circulation, because of its critical importance for biogeochemical modeling. While the analysis was on a particular OGCM, the ocean component of CESM, and the BEC model, the applicability of the techniques extends to other models.

The development of the offline seasonally-cycling model documented in Chapter 2 provides a platform that makes possible the analysis of ^{14}C age, and the ventilation studies in Chapter 3. The regional model documented in Chapter 4 was formed by isolating a piece of the global ocean in an offline model, and provides a platform suitable for regional biogeochemical studies. The regional isolation technique shows promise as a method of separating local versus global influences, as well as providing substantial computational savings.

As a result of the work encompassed in this dissertation, there exists additions to the tool sets and platforms for doing the analysis that will lead to better models. The practical application of previously available tools (Kwon and Primeau, 2008; Primeau, 2005) has brought their utility into focus.

The results from the work in each chapter have held some enlightening, and sometimes surprising, results. We discovered that the model circulation in the Pacific Ocean was extremely sluggish. We found that in the model a large proportion of the ventilation of the entire global ocean comes from the tiny Labrador Sea. It was discovered that, contrary to observations, the model lacks of bottom water formation in the Southern Ocean. We found that, according to the model, the major oxygen ventilation source for the most intense part of the Indian Ocean OMZs is the surface of the Indian Ocean, a substantial fraction is from the southern boundary, and only a tiny fraction is from the Indonesian Throughflow; we do not have sufficient observations to verify this finding. All of these results were obtained using the new tools that were developed and applied in this work, and are available for future ocean model analysis.

5.2 Summary and Future Research Stemming from Chapter 2

An offline seasonally-cycling tracer-transport model was built using an Impulse-Response-Function approach to capture the advection and horizontal diffusion fields of the parent prognostic model. The vertical diffusion was obtained by explicit coding using the diffusion coefficient which was dynamically calculated during the same model simulation. This approach allowed the offline tracer transport matrix to represent the net effect of all the physics in the parent model.

We ran a natural ^{14}C simulation with the offline model, and found that while the surface and North Atlantic values were a good match with observations, the ^{14}C age in the Pacific and the Indian Oceans showed an excessively old ^{14}C age bias. This was convincing evidence that ^{14}C analysis of the deep ocean circulation in OGCMs is necessary in order to learn at least whether or not there is a problem. This extreme ^{14}C age bias result helped to explain some of the problematic results seen when the BEC was run using this circulation as a basis. There is an impact on oxygen concentrations from the sluggish circulation in the Pacific. The rate of oxygen-rich water supplied by the circulation is insufficient to counteract the losses due to remineralization, making the resulting estimates of oxygen concentration too low.

We were successful in finding a preconditioner that worked well with the ^{14}C tracer for the Newton-Krylov solver. This allowed what would have taken over 4000 model years of time-stepping the model to achieve a steady-state result to be achieved in 23 model years.

The message of Chapter 2 is loud and clear: ^{14}C tracer studies should be done on OGCMs to characterize the circulation in the deep, and here is a set of tools to make this possible. Future research effort to follow up on the work documented in Chapter 2 is, first, to develop the interface to updated versions of the CESM ocean component, so that we can continue to provide the mechanism to make the ^{14}C simulation practical. And second, to look into creating an offline version of a higher resolution eddy-resolving model. The eddy-resolving class of models may need the technique even more critically than the 1° horizontal resolution configuration we used, because the higher resolution substantially increases the computational costs of tracer spin-up times.

An open question is whether or not the spin-up of the circulation dynamics of 150 years from rest was adequate before taking the one-year snapshot of the advective and diffusive tendencies to build the offline tracer transport model. Recent informal experiments with a similar model configuration are showing that the excessive old age in the Pacific becomes even more excessive with continued spin-up of the circulation. I think this is symptomatic of the situation facing the development of many OGCMs. It is a hard choice for the use of computer resources and the clock-time to do the circulation spin-up long enough to achieve a quasi-equilibrium in the deep ocean. Note, however, that even if the 150 year spin-up was not sufficiently long to generate the quasi-equilibrium answer, it was long enough to see the gross symptoms of excessive ^{14}C age, and trigger additional questions as to the cause.

Extensions of the seasonally-cycling offline model approach to cover the next-biggest cycle in the ocean, El Niño, should be considered. There is nothing inherent in the method that restricts its application to a one year cycle. We should consider how we might encompass the hysteresis effects of long time-scale processes that take greater than a year that are present in the ocean circulation, such as results in El Niño (Trenberth and Stepaniak, 2001; Qu and Yu, 2014) or the Pacific Decadal Oscillation (Saravanan and McWilliams, 1998; MacDonald and Case, 2005; Newman et al., 2003); or that results from the heat up-take of the ocean due to climate change (Raper et al., 2002; Meehl et al., 2011; Balmaseda et al., 2013).

5.3 Summary and Future Research Stemming from Chapter 3

The ventilation source analysis in Chapter 3 complemented the ^{14}C analysis in Chapter 2, providing additional insight into the circulation in the deep ocean in the model. The Labrador Sea can be seen to have a critical role in ventilating the North Atlantic. The effectiveness of the newly-added parameterization of sill-overflow transport in the parent model was visible in the flows from the GIN Sea. In the Southern Ocean there were no flows resulting from the sill-overflow parameterization, and a lack of bottom-water formation in the Southern Ocean is clearly evident. An estimate of the water in the global ocean ventilated in the North Atlantic was 51% versus 39% from the Southern Ocean. The Southern Ocean contribution appears low compared to estimates from other studies (DeVries and Primeau, 2011; Gebbie and Huybers, 2010; Johnson, 2008). Since the Southern Ocean is important to CO_2 uptake from the atmosphere, the low ventilation from the Southern Ocean in the model can produce biased results.

The results in Chapter 3 were generated using an annually-averaged transport matrix. Although it is not expected that seasonality would have a significant impact on the results in the deep ocean, we should verify that this is the case. That is, we should explore calculating the water mass fractions with seasonally-cycling transport operators.

Additional research, building on this technique, could encompass dividing the surface more finely along physical isopycnal lines, or into Longhurst (Longhurst, 2007) or Teng (Teng et al., 2014) biogeographical regions, and explore the distribution of some of the biological tracers, such as NO_3, PO_4, or O_2. Exploratory questions would relate to the contribution from various sources; how does the distribution change due to mixing of various source waters; and what is the rate of change seen due to biological action as opposed to mixing.

5.4 Summary and Future Research Stemming from Chapter 4

We were able to create a regional model of the Indian Ocean, based on the global offline model whose development was documented in Chapter 2. The regional model isolated the Indian Ocean using a newly developed technique that provides active advection and diffusion on the boundaries of the selected region. It was demonstrated that the distinction between external and within-the-region effects could be made.

Having a tracer that is not biologic, such as ^{14}C, applied to the regional model provided a mechanism to separate the circulation biases from the biological calculation biases within the region. In the case of the Indian Ocean region in this study, it provided reassurance that the circulation biases within the Indian Ocean region would not overshadow the biological computations.

The BEC oxygen production and consumption output from a CMIP5 BEC simulation were used to drive the oxygen regional model. There was a significant difference between the CMIP5 BEC global oxygen concentration results and those obtained with the offline model with CMIP5 BEC-generated values on the boundary. This is attributed to the differences in the spin-up and forcings used. Changing the boundary values to observations for the regional model simulation gave a third set of oxygen results, which were the closest to observations.

The cases we ran in this study need comparable cases in which the CMIP5 circulation is used as a basis; to do that we need the ability to make the CMIP5 simulation a parent of its own offline model. Using the same circulation as a basis will provide more insight into the comparison of local versus remote influences on the BEC production and consumption. This also would make it possible to use ^{14}C as a diagnostic on the circulation resulting from the CMIP5 forcings.

Further research is needed to find an effective preconditioner for oxygen. It is a very integrative quantity for the biological results, which makes this worth pursuing. While the Newton-Krylov method yielded an improvement in the time required to obtain a solution compared to time-stepping: about 110 model years versus 400 for time-stepping, the improvement was significantly less than obtained in the global solution of ^{14}C in Chapter 2. On the other hand, the time-stepped solution for oxygen in the regional model was obtained in fewer model years by a factor of 10 than that required for the global ^{14}C case. This may be the result of having the time-scales and distances of the local forces in the circulation dominate.

A simpler method of calculating production and consumption than is done in the BEC would make sensitivity studies of the parameterizations easier to perform. It would also provide a sanity check for BEC calculations when applied to the same circulation.

The circulation at the surface is greatly affected by the monsoonal seasonality. Our analysis of the ventilation sources was done using an annual-average circulation. It is possible to do the analysis on a seasonal basis, which would show not only where the oxygen ventilation is taking place, but also when. A seasonally based estimate has obvious relevance for the Indian Ocean, but would also be useful for other regions with strong seasonal cycles. An efficient way of making the calculation is needed.

It is quite possible to make other regional models using this approach. There is nothing specific to the Indian Ocean in the derivation of the method. This could, for example, provide a platform for studying variations in export production in a particular region. Regions could be partitioned into Longhurst (Longhurst, 2007) or Teng (Teng et al., 2014) biogeographical regions for further study of the differences in the characteristics of production, export, and oxygen consumption.

Bibliography

Altabet, M.A., Ryabenko, E., Stramma, L., Wallace, D.W.R., Frank, M., Grasse, P., Lavik, G., 2012. An eddy-stimulated hotspot for fixed nitrogen-loss from the peru oxygen minimum zone. Biogeosciences 9, 4897–4908.

Amestoy, P.R., Duff, I.S., Koster, J., L'Excellent, J.Y., 2001. A fully asynchronous multifrontal solver using distributed dynamic scheduling. SIAM Journal of Matrix Analysis and Applications 23, 15–41.

Anderson, T.R., Ryabcenko, V., Fasham, M.J.R., Gorchakov, V.A., 2007. Denitrification in the arabian sea: A 3d ecosystem modelling study. Deep-Sea Research I 54, 2082–2119.

Atmadipoera, A., Molcard, R., Madec, G., Wijffels, S., Sprintall, J., Koch-Larrouy, A., Jaya, I., Supangat, A., 2009. Characteristics and variability of the indonesian throughflow water at the outflow straits. Deep-Sea Research I 56, 1942–1956.

Bacastow, R., Maier-Reimer, E., 1990. Ocean-circulation model of the carbon cycle. Climate Dynamics 4, 95–125.

Balmaseda, M.A., Trenberth, K.E., Kallen, E., 2013. Distinctive climate signals in reanalysis of global ocean heat content. Geophysical Research Letters 40, 1754–1759.

Bange, H.W., Naqvi, S.W.A., Codispoti, L.A., 2005. The nitrogen cycle in the arabian sea. Progress in Oceanography 65, 145–158.

Beal, L.M., Chereskin, T.K., Bryden, H.L., Field, A., 2003. Variability of water properties, heat and salt fluxes in the arabian sea, between the onset and wane of the 1995 southwest monsoon. Deep-Sea Research II 50, 2049–2075.

Bertrand, A., Ballon, M., Chaigneau, A., 2010. Acoustic observation of living organisms reveals the upper limit of the oxygen minimum zone. Plos One 5.

Bianchi, D., Galbraith, E.D., Carozza, D.A., Mislan, K.A.S., Stock, C.A., 2013. Intensification of open-ocean oxygen depletion by vertically migrating animals. Nature Geoscience 6, 545–548.

Bograd, S.J., Castro, C.G., Di Lorenzo, E., Palacios, D.M., Bailey, H., Gilly, W., Chavez, F.P., 2008. Oxygen declines and the shoaling of the hypoxic boundary in the california current. Geophysical Research Letters 35, L12707.

Bopp, L., Le Quere, C., Heimann, M., Manning, A.C., Monfray, P., 2002. Climate-induced oceanic oxygen fluxes: Implicaions for the contemporary carbon budget. Global Biogeochemical Cycles 16, 6–1 – 6–8.

Bopp, L., Resplandy, L., Orr, J.C., Doney, S.C., Dunne, J.P., Gehlen, M., Halloran, P., Heinze, C., Ilyina, T., Seferian, R., Tjiputra, J., Vichi, M., 2013. Multiple stressors of ocean ecosystems in the 21st century: projections with CMIP5 models. Biogeosciences 10, 6225–6245.

Bower, A.S., Hunt, H.D., Price, J.F., 2000. Character and dynamics of the red sea and persian gulf outflows. Journal of Geophysical Research 105, 6387–6414.

Brandes, J.A., Devol, A., Deutsch, C., 2007. New developments in the marine nitrogen cycle. Chemical Review 107, 577–589.

Breuer, E.R., Law, G.T.W., Woulds, C., Cowie, G.L., Shimmield, G.B., Peppe, O., Schwartz, M., McKinlay, S., 2009. Sedimentary oxygen consumption and microdistribution at sites across the arabian sea oxygen minimum zone (pakistan margin). Deep-Sea Research II 56, 296–304.

Briegleb, B.P., Danabasoglu, G., Large, W.G., 2010. An Overflow Parameterization for the Ocean Component of the Community Climate System Model. NCAR Technical Note. NCAR.

Bryan, F.O., Danabasoglu, G., Gent, P.R., Lindsay, K., 2006. Changes in ocean ventilation during the 21st century in the CCSM3. Ocean Modelling 15, 141–156.

Bulow, S.E., Rich, J.J., Naik, H.S., Pratihary, A.K., Ward, B.B., 2010. Denitrification exceeds anammox as a nitrogen loss pathway in the arabian sea oxygen minimum zone. Deep-Sea Research I 57, 384–393.

Burkill, P.H., Mantoura, R.F.C., Owens, N.J.P., 1993. Biogeochemical cycling in the northwestern indian ocean: a brief overview. Deep-Sea Research II 40, 643–649.

Butzin, M., Prange, M., Lohmann, G., 2005. Radiocarbon simulations for the glacial ocean: The effects of wind stress, southern ocean sea ice and heinrich events. Earth and Planetary Science Letters 235, 45–61.

Chan, F., Barth, J.A., Lubchenco, J., Kirincich, A., Weeks, H., Peterson, W.T., Menge, B.A., 2008. Emergence of anoxia in the california current large marine ecosystem. Science 319, 920–920.

Cicerone, R.J., Oremland, R.S., 1988. Biogeochemical aspects of atmospheric methane. Global Biogeochemical Cycles 2, 299–327.

Codispoti, L., Brandes, J.A., Christensen, J., Devol, A., Naqvi, S., Paerl, H.W., Yoshinari, T., 2001. The oceanic fixed nitrogen and nitrous oxide budgets: Moving targets as we enter the anthropocene? Scientia Marina 65 (Suppl 2.), 85–105.

Cowie, G.L., Mowbray, S., Lewis, M., Matheson, H., McKenzie, R., 2009. Carbon and nitrogen elemental and stable isotopic compositions of surficial sediments from the pakistan margin of the arabian sea. Deep-Sea Research II 56, 271–282.

Danabasoglu, G., Bates, S., Briegleb, B., Jayne, S., Jochum, M., Large, W., Peacock, S., Yeager, S., 2012. The CCSM4 ocean component. Journal of Climate 25, 1361–1389.

Danabasoglu, G., Ferrari, R., McWilliams, J.C., 2008. Sensitivity of an ocean general circulation model to a parameterization of near-surface eddy fluxes. Journal of Climate 21, 1192–1208.

Danabasoglu, G., Large, W.G., Briegleb, B.P., 2010. Climate impacts of parameterized nordic seas overflows. Journal of Geophysical Research - Oceans submitted.

Danabasoglu, G., Large, W.G., Tribbia, J.J., Gent, P.R., Briegleb, B.P., McWilliams, J.C., 2006. Diurnal coupling in the tropical oceans of CCSM3. Journal of Climate 19, 2347–2365.

Danabasoglu, G., Marshall, J., 2007. Effects of vertical variations of thickness diffusivity in an ocean general circulation model. Ocean Modelling 18, 122–141.

Davis, J.C., 1975. Minimal dissolved oxygen requirements of aquatic life with emphasis on canadian species: a review. Journal of the Fisheries Research Board of Canada 32, 2295–2332.

Deutsch, C., 2011. Climate-forced variability of ocean hypoxia. Science OMZ collection.

DeVries, T., Primeau, F., 2011. Dynamically- and observationally-constrained estimates of water-mass distributions and ages in the global ocean. Journal of Physical Oceanography 41, 2381–2401.

Doney, S.C., Lindsay, K., Caldeira, K., Campin, J.M., Drange, H., Dutay, J.C., Follows, M., Gao, Y., Gnanadesikan, A., Gruber, N., Ishida, A., Joos, F., Madec, G., Maier-Reimer, E., Marshall, J.C., Matear, R.J., Monfray, P., Mouchet, A., Najjar, R., Orr, J.C., Plattner, G.K., Sarmiento, J.L., Schlitzer, R., Slater, R., Totterdell, I.J., Weirig, M.F., Yamanaka, Y., Yool, A., 2004. Evaluating global ocean carbon models: The importance of realistic physics. Global Biogeochemical Cycles 18.

Ducklow, H.W., Campbell, L., Landry, M.R., Quinby, H.L., Steward, G.F., Azam, F., 2001. Heterotrophic bacterioplankton in the arabian sea: Basin-wide response to year-round high primary productivity. Deep-Sea Research II 48, 1303–1323.

Duffy, P.B., Caldeira, K., Selvaggi, J., Hoffert, M.I., 1997. Effects of subgrid-scale mixing parameterizations on simulated distributions of natural 14c, temperature, and salinity in a three-dimensional ocean general circulation model. Journal of Physical Oceanography 27, 498–523.

Dugdale, R.C., 1977. Nutrient modelling, in: The Sea. Wiley, New York. volume 6, pp. 789–806.

Dutay, J.C., Jean-Baptiste, P., Campin, J.M., Ishida, A., Maier-Reimer, E., Matear, R.J., Mouchet, A., Totterdell, I.J., Yamanaka, Y., Rodgers, K.B., Madec, G., Orr, J.C., 2004. Evaluation of OCMIP-2 ocean models' deep circulation with mantle helium-3. Journal of Marine Systems 48, 15–36.

Emerson, S.R., Watanabe, Y.W., Ono, T., Mecking, S., 2004. Temporal trends in apparent oxygen utilization in the upper pycnocline of the north pacific: 1980-2000. Journal of Oceanography 60, 139–147.

England, M.H., 1995. The age of water and ventilation timescales in a global ocean model. Journal of Physical Oceanography 25, 2756–2777.

England, M.H., Rahmstorf, S., 1999. Sensitivity of ventilation rates and radiocarbon uptake to subgrid-scale mixing in ocean models. Journal of Physical Oceanography 29, 2802 – 2827.

Falkowski, P.G., 1997. Evolution of the nitrogen cycle and its influence on the biological sequestration of CO2 in the ocean. Nature 387, 272–275.

Ferrari, R., McWilliams, J.C., Canuto, V.M., Dubovikov, M., 2008. Parameterization of eddy fluxes near ocanic boundaries. Journal of Climate 21, 2770–2789.

Fine, R.A., Smethie, Jr, W.M., Bullister, J.L., Rhein, M., Min, D.H., Warner, M.J., Poisson, A., Weiss, R.F., 2008. Decadal ventilation and mixing of indian ocean waters. Deep-Sea Research I 55, 20–37.

Follows, M.J., Ito, T., Marotzke, J., 2002. The wind-driven, subtropical gyres and the solubility pump of CO2. Global Biogeochemical Cycles 16.

Fox-Kemper, B., Ferrari, R., Hallberg, R., 2011. Parameterization of mixed layer eddies. part III: Implementation and impact in global ocean climate simulations. Ocean Modelling 39, 61–78.

Franz, J., Krahmann, G., Lavik, G., Grasse, P., Dittmar, T., Riebesell, U., 2012. Dynamics and stoichiometry of nutrients and phytooplankton in waters influenced by the oxygen minimum zone in the eastern tropical pacific. Deep-Sea Research I 62, 20–31.

Gage, J.D., Levin, L.A., Wolff, G.A., 2000. Benthic processes in the deep arabian sea: introduction and overview. Deep-Sea Research II 47, 1–7.

Galbraith, E.D., Kwon, E.Y., Gnanadesikan, A., Rodgers, K.B., Griffies, S.M., Bianchi, D., Sarmiento, J.L., Dunne, J.P., Simeon, J., Slater, R.D., Wittenberg, A.T., Held, I.M., 2011. Climate variability and radiocarbon in the CM2mc earth system model. Journal of Climate 25, 4230–4254.

Garcia, H., Locarnini, R., Boyer, T., Antonov, J.I., Baranova, O.K., Zweng, M.M., Reagan, J.R., Johnson, D.R., 2014. Dissolved oxygen, apparent oxygen utilization, and oxygen saturation, in: World Ocean Atlas 2013. NOAA. volume 3, p. 27.

Gebbie, G., Huybers, P., 2010. Total matrix intercomparison: A method for determining the geometry of water-mass pathways. Journal of Physical Oceanography 40, 1710–1728.

Gebbie, G., Huybers, P., 2012. The mean age of ocean waters inferred from radiocarbon observations: sensitivity to surface sources and accounting for mixing histories. Journal of Physical Oceanography 42, 291–305.

Gent, P.R., McWilliams, J.C., 1990. Isopycnal mixing in ocean circulation models. Journal of Physical Oceanography 20, 150–155.

Gnanadesikan, A., Dunne, J.P., John, J., 2012. Understanding why the volume of suboxic waters does not increase over centuries of global warming in an earth system model. Biogeosciences 9, 1159–1172.

Gnanadesikan, A., Dunne, J.P., Key, R.M., Matsumoto, K., Sarmiento, J.L., Slater, R.D., Swathi, P.S., 2004. Oceanic ventilation and biogeochemical cycling: Understanding the physical mechanisms that produce realistic distributions of tracers and productivity. Global Biogeochemical Cycles 18, GB4010.

Gnanadesikan, A., Slater, R.D., Gruber, N., Sarmiento, J.L., 2002. Oceanic vertical exchange and new production: a comparison between models and observations. Deep-Sea Research II 49, 363–401.

Gomes, H.R., Goes, J.I., Saino, T., 2000. Influence of physical processes and freshwater discharge on the seasonality of phytoplankton regime in the bay of bengal. Continental Shelf Research 20, 313–330.

Gooday, A.J., Bernhard, J.M., Levin, L.A., Suhr, S.B., 2000. Foraminifera in the arabian sea oxygen minimum zone and other oxygen-deficient settings: taxonomic composition, diversity, and relation to metazoan faunas. Deep-Sea Research II 47, 25–54.

Goosse, H., Fichefet, T., 1999. Importance of ice-ocean interactions for the global ocean circulation: A model study. Journal of Geophysical Research 104, 23337–23355.

Gordon, A.L., Giulivi, C.F., Ilahude, A.G., 2003. Deep topographic barriers within the indonesian seas. Deep-Sea Research II 50, 2205–2228.

Gordon, C., Cooper, C., Senior, C.A., Banks, H., Gregory, J.M., Johns, T.C., Mitchell, J.F.B., Wood, R.A., 2000. The simulation of SST, sea ice extents and ocean heat transports in a version of the hadley centre coupled model. Climate Dynamics 16, 147–168.

Graven, H.D., Gruber, N., Key, R., Khatiwala, S., Giraud, X., 2012. Changing controls on oceanic radiocarbon: New insights on shallow-to-deep ocean exchange and anthropogenic CO2 uptake. Journal of Geophysical Research 117, 1–16.

Gray, J.S., Wu, R.S.s., Or, Y.Y., 2002. Effects of hypoxia and organic enrichment on the coastal marine environment. Marine Ecology Progress Series 238, 249–279.

Griffies, S.M., Biastoch, A., Boning, C., Bryan, F., Danabasoglu, G., Chassignet, E.P., England, M.H., Gerdes, R., Haak, H., Hallberg, R.W., Hazeleger, W., Jungclaus, J., Large, W.G., Madec, G., Pirani, A., Samuels, B.L., Scheinert, M., Sen Gupta, A., Severijns, C.A., Simmons, H.L., Trequier, A.M., Winton, M., Yeager, S., Yin, J.J., 2009. Coordinated ocean-ice reference experiments (COREs). Ocean Modelling 26, 1–46.

Gruber, N., Gloor, M., Fan, S.M., Sarmiento, J.L., 2001. Air-sea flux of oxygen estimated from bulk data: Implications for the marine and atmospheric oxygen cycles. Global Biogeochemical Cycles 15, 783–803.

Guilderson, T.P., Caldeira, K., Duffy, P.B., 2000. Radiocarbon as a diagnostic tracer in ocean and carbon cycle modeling. Global Biogeochemical Cycles 14, 887–902.

Haine, T.W.N., Hall, T.M., 2002. A generalized transport theory: Water-mass composition and age. Journal of Physical Oceanography 32, 1932–1946.

Hall, T.M., Haine, T.W.N., 2002. On ocean transport diagnostics: The idealized age tracer and the age spectrum. Journal of Physical Oceanography 32, 1987–1991.

Heinze, C., Maier-Reimer, E., 1991. Glacial pCO2 reduction by the world ocean: Experiments with the hamburg carbon cycle model. Paleoceanography 6, 395–430.

Helly, J.J., Levin, L.A., 2004. Global distribution of naturally occurring marine hypoxia on continental margins. Deep-Sea Research I 51, 1159–1168.

Honjo, S., Dymond, J., Prell, W., Ittekkot, V., 1999. Monsoon-controlled export fluxes to the interior of the arabian sea. Deep-Sea Research II 46, 1859–1902.

Ito, T., Woloszyn, M., Mazloff, M., 2010. Anthropogenic carbon dioxide transport in the southern ocean driven by ekman flow. Nature 463, 80–83.

Ittekkot, V., Kudrass, H.R., Quadfasel, D., Unger, D., 2003. The bay of bengal - an introduction. Deep-Sea Research II 50, 853–854.

Jacobson, M.Z., 2005. Studying ocean acidification with conservative, stable numerical schemes for nonequilibrium air-ocean exchange and ocean equilibrium chemistry. Journal of Geophysical Research - Atmospheres 110.

Jayne, S.R., 2009. The impact of abyssal mixing parameterizations in an ocean general circulation model. Journal of Physical Oceanography 39, 1756–1775.

Jochum, M., 2009. Impact of latitudinal variations in vertical diffusivity on climate simulations. Journal of Geophysical Research 114, C01010.

Johnson, G.C., 2008. Quantifying antarctic bottom water and north atlantic deep water volumes. Journal of Geophysical Research 113, C05027.

Kamykowski, D., Zentara, S.J., 1990. Hypoxia in the world ocean as recorded in the historical data set. Deep-Sea Research 37, 1861–1874.

Kawamiya, M., 2001. Mechanism of offshore nutrient supply in the western arabian sea. Journal of Marine Research 59, 675–696.

Keeling, R.F., Garcia, H.E., 2002. The change in oceanic o2 inventory associated with recent global warming. Proceedings of the National Academy of Sciences 99, 7848–7853.

Keeling, R.F., Kortzinger, A., Gruber, N., 2010. Ocean deoxygenation in a warming world. Annual Revue of Marine Science 2010, 199–229.

Kelley, C.T., 2003. Solving nonlinear equations with Newton's method. Society for Industrial and Applied Mathematics, Philadelphia, PA.

Key, R.M., Kozyr, A., Sabine, C.L., Lee, K., Wanninkhof, R., Bullister, J.L., Feely, R.A., Millero, F.J., Mordy, C., Peng, T.H., 2004. A global ocean carbon climatology: Results for global data analysis project (GLODAP). Global Biogeochemical Cycles 18.

Khatiwala, S., 2007. A computational framework for simulation of biogeochemical tracers in the ocean. Global Biogeochemical Cycles 21.

Khatiwala, S., 2008. Fast spin up of ocean biogeochemical models using matrix-free newtonkrylov. Ocean Modelling 23, 121–129.

Khatiwala, S., Visbeck, M., Cane, M.A., 2004. Accelerated simulation of passive tracers in ocean circulation models. Ocean Modelling 9, 52– 69.

Krakauer, N.Y., Randerson, J.T., Primeau, F.W., Gruber, N., Menemenlis, D., 2006. Carbon isotope evidence for the latitudinal distribution and wind speed dependence of the air-sea gas transfer velocity. Tellus B 58, 390–417.

Kwon, E.Y., Primeau, F., 2008. Optimization and sensitivity of a global biogeochemistry ocean model using combined in situ DIC, alkalinity, and phosphate data. Journal of Geophysical Research 113.

Lamont, P.A., Gage, J.D., 2000. Morphological responses of macrobenthic polychaetes to low oxygen on the oman continental slope, NW arabian sea. Deep-Sea Research II 47, 9–24.

Large, W.G., Danabasoglu, G., Doney, S.C., McWilliams, J., 1997. Sensitivity to surface forcing and boundary layer mixing in a global ocean model: Annual-mean climatology. Journal of Physical Oceanography 27, 2418–2447.

Large, W.G., McWilliams, J.C., Gent, P.R., Bryan, F.O., 1994. Oceanic vertical mixing: A review and a model with a nonlocal boundary layer parameterization. Reviews of Geophysics 32, 363–403.

Large, W.G., Yeager, S.G., 2009. The global climatology of an interannually varying air-sea flux data set. Climate Dynamics 33, 341–364.

Levin, L., 2002. Deep-ocean life where oxygen is scarce. American Scientist 90, 436–444.

Levin, L.A., Gage, J.D., 1998. Relationships between oxygen, organic matter and diversity of bathyal macrofauna. Deep-Sea Research II 45, 129–163.

Levin, L.A., Gage, J.D., Lamont, P., Cammidge, L., Patience, A., Martin, C., 1997. Infaunal community structure in a low-oxygen organic rich habitat on the oman continental slope, NW arabian sea.

Levin, L.A., Gage, J.D., Martin, C., Lamont, P., 2000. Macrobenthic community structure within and beneath the oxygen minimum zone, NW arabian sea. Deep-Sea Research II 47, 189–226.

Li, X., Primeau, F., 2008. A fast newtonkrylov solver for seasonally varying global ocean biogeochemistry models. Ocean Modelling 23, 13–20.

Longhurst, A.R., 2007. Ecological Geography of the Sea. Elsevier Inc.. second edition.

MacDonald, G.M., Case, R.A., 2005. Variations in the pacific decadal oscillation over the past millennium. Geophysical Research Letters 32, 1–4.

Madec, G., Delecluse, P., Imbard, M., Levy, C., 1998. OPA 8.1 ocean general circulation model reference manual.

Madhupratap, M., Gauns, M., Ramaiah, N., PrasannaKumar, S., Muraleedharan, P.M., DeSousa, S.N., Sardessai, S., Muraleedharan, U., 2003. Biogeochemistry of the bay of bengal: physical, chemical and primary productivity characteristics of the central and western bay of bengal during summer monsoon 2001. Deep-Sea Research II 50, 881–896.

Maier-Reimer, E., 1993. Geochemical cycles in an ocean general circulation model. preindustrial tracer distributions. Global Biogeochemical Cycles 7, 645–677.

Maier-Reimer, E., Hasselmann, K., 1987. Transport and storage of CO2 in the ocean - an inorganic ocean-circulation carbon cycle model. Climate Dynamics 2, 63–90.

Matear, R.J., 2001. Effects of numerical advection schemes and eddy parameterizations on ocean ventilation and oceanic anthropogenic CO2 uptake. Ocean Modelling 3, 217–248.

Matear, R.J., Hirst, A.C., 1999. Climate change feedback on the future oceanic CO2 uptake. Tellus 51B, 722–733.

Matear, R.J., Hirst, A.C., 2003. Long-term changes in dissolved oxygen concentrations in the ocean caused by protracted global warming. Global Biogeochemical Cycles 17, 1125.

Matsumoto, K., Sarmiento, J.L., Key, R.M., Aumont, O., Bullister, J.L., Caldeira, K., Campin, J.M., Doney, S.C., Drange, H., Dutay, J.C., Follows, M., Gao, Y., Gnanadesikan, A., Gruber, N., Ishida, A., Joos, F., Lindsay, K., Maier-Reimer, E., Marshall, J.C., Matear, R.J., Monfray, P., Mouchet, A., Najjar, R., Plattner, G.K., Schlitzer, R., Slater, R., Swathi, P.S., Totterdell, I.J., Weirig, M.F., Yamanaka, Y., Yool, A., Orr, J.C., 2004. Evaluation of ocean carbon cycle models with data-based metrics. Geophysical Research Letters 31, L07303.

McCreary, J.P., Yu, Z., Hood, R.R., Vinaychandran, P.N., Furue, R., Ishida, A., Richards, K., 2013. Dynamics of the indian-ocean oxygen minimum zones. Progress in Oceanography 112-113, 15–37.

Mecking, S., Langdon, C., Feely, R.A., Sabine, C.L., Deutsch, C., Min, D.H., 2008. Climate variability in the north pacific thermocline diagnosed from oxygen measurements: An update based on the u.s. CLIVAR/CO2 repeat hydrography cruises. Global Biogeochemical Cycles 22, 1–11.

Meehl, G.A., Arblaster, J.M., Fasulio, J.T., Hu, A., Trenberth, K.E., 2011. Model-based evidence of deep-ocean heat uptake during surface-temperature hiatus periods. Nature Climate Change 1, 360–364.

Moore, J.K., Doney, S.C., 2007. Iron availability limits the ocean nitgrogen inventory stabilizing feedbacks between marine denitrification and nitrogen fixation. Global Biogeochemical Cycles 21, 1–12.

Moore, J.K., Lindsay, K., Doney, S.C., Long, M.C., Misumi, K., 2013. Marine ecosystem dynamics and biogeochemical cycling in the community earth system model [CESM1(BGC)]: Comparison of the 1990s with the 2090s under the RCP4.5 and RCP8.5 scenarios. Journal of Climate 26, 9291–9312.

Morrison, J.M., Codispoti, L.A., Smith, S.L., Wishner, K., Flagg, C., Gardner, W.D., Gaurin, S., Naqvi, S.W.A., Manghnani, V., Prosperie, L., Gundersen, J.S., 1999. The oxygen minimum zone in the arabian sea during 1995. Deep-Sea Research II 46, 1903–1931.

Muller, S.A., Joos, F., Edwards, N.R., Stocker, T.F., 2006. Water mass distribution and ventilation time scales in a cost-efficient, three-dimensional ocean model. Journal of Climate 19, 5479–5499.

Nair, R.R., Ittekkot, V., Manganini, S.J., Ramaswamy, V., Haake, B., Degens, E.T., Desai, B.N., Honjo, S., 1989. Increased particle flux to the deep ocean related to monsoons. Nature 338, 749–751.

Newman, M., Compo, G.P., Alexander, M.A., 2003. ENSO-forced variability of the pacific decadal oscillation. Journal of Climate 16, 3953–3857.

Oguz, T., Ducklow, H.W., Malanotte-Rizzoli, P., 2000. Modeling distinct vertical biogeochemical structure of the black sea: Dynamical coupling of the oxic, suboxic, and anoxic layers. Global Biogeochemical Cycles 14, 1331–1352.

Orr, J.C., 2002. Global ocean storage of anthropogenic carbon (GOSAC), EC environment and climate programme final report.

Oschlies, A., Schulz, K.G., Riebesell, U., Schmittner, A., 2008. Simulated 21st century's increase in oceanic suboxia by CO2 -enhanced biotic carbon export. Global Biogeochemical Cycles 22.

Pacanowski, R.C., Griffies, S.M., 1999. The MOM 3 manual, apha version.

Paulmier, A., Ruiz-Pino, D., 2009. Oxygen minimum zones (OMZs) in the modern ocean. Progress in Oceanography 80, 113–128.

Paulmier, A., Ruiz-Pino, D., Garcon, V., 2011. CO2 maximum in the oxygen minimum zone (OMZ). Biogeosciences 8, 239–252.

Paulmier, A., Ruiz-Pino, D., Garcon, V., Farias, L., 2006. Maintaining of the eastern south pacific oxygen minimum zone (OMZ) off chile. Geophysical Research Letters 33, 1–6.

Prakash, S., Nair, T.M.B., Bhaskar, T.V.S.U., Prakash, P., Gilbert, D., 2012. Oxycline variability in the central arabian sea: An argo-oxygen study. Journal of Sea Research 71, 1–8.

PrasannaKumar, S., Muraleedharan, P.M., Prasad, T.G., Gauns, M., Ramaiah, N., DeSousa, S.N., Sardessai, S., Madhupratap, M., 2002. Why is the bay of bengal less productive during summer monsoon compared to the arabian sea? Geophysical Research Letters 29, 881–884.

Primeau, F., 2005. Characterizing transport between the surface mixed layer and the ocean interior with a forward and adjoint global ocean transport model. Journal of Physical Oceanography 35, 545–564.

Primeau, F., Holzer, M., 2006. The ocean's memory of the atmosphere: Residence-time and ventilation-rate distributions of water masses. Journal of Physical Oceanography 36, 1439–1456.

Qu, T., Yu, J.Y., 2014. ENSO indices from sea surface salinity observed by aquarius and argo. Journal of Oceanography 70, 367–375.

Ramaiah, N., Raghukumar, S., Mangesh, G., Madhupratap, M., 2005. Seasonal variations in carbon biomass of bacteria, thraustochytrids and microzooplankton in the northern arabian sea. Deep-Sea Research II 52, 1910–1921.

Raper, S.C.B., Gregory, J.M., Stouffer, R.J., 2002. The role of climate sensitivity and ocean heat uptake on AOGCM transient temperature response. Journal of Climate 15.

Ravichandran, M., Girishkumar, M.S., Riser, S.C., 2012. Observed variability of chlorophyll-a using argo profiling floats in the southeastern arabian sea. Deep-Sea Research I 65, 15–25.

Reid, J.L., 2005. On the world-wide circulation of the deep water from the north atlantic ocean. Journal of Marine Research 63, 187–201.

Reid, J.L., Lynn, R.J., 1971. On the influence of norwegian-greenland and weddell seas on the bottom waters of the indian and pacific oceans. Deep Sea Research 18, 1063–1088.

Resplandy, L., Levy, M., Bopp, L., Echevin, V., Pous, S., Sarma, V.V.S.S., Kumar, D., 2012. Controlling factors of the oxygen balance in the arabian sea's OMZ. Biogeosciences 9, 5095–5109.

Resplandy, L., Levy, M., Madec, G., Pous, S., Aumont, O., Kumar, D., 2011. Contribution of mesoscale processes to nutrient budgets in the arabian sea. Journal of Geophysical Research 116, 1–24.

Rogers, A.D., 2000. The role of the oceanic oxygen minima in generating biodiversity in the deep sea. Deep-Sea Research II 47, 119–148.

Roussenov, V., Williams, R.G., Follows, M.J., Key, R.M., 2004. The role of bottom water transport and diapycnic mixing in determining the radiocarbon distribution in the pacific. Journal of Geophysical Research 109.

Rubin, S.I., Key, R.M., 2002. Separating natural nd bomb-produced radiocarbon in the ocean: The potential alkalinity method. Global Biogeochemical Cycles 16, 1105–1124.

Sabine, C.L., Key, R.M., Kozyr, A., Feely, R.A., Wanninkhof, R., Millero, F.J., Peng, T.H., Bullister, J.L., Lee, K., 2005. Global ocean data analysis project (GLODAP): Results and data.

Saravanan, R., McWilliams, J.C., 1998. Advective ocean-atmosphere interaction: An analytical stochastic model with implications for decadal variability. Journal of Climate 11, 165–188.

Sarma, V.V.S.S., Krishna, M.S., Viswanadham, R., Rao, G.D., Rao, V.D., Sridevi, B., Kumar, B.S.K., Prasad, V.R., Subbaiah, C.V., 2013. Intensified oxygen minimum zone on the western shelf of bay of bengal during summer monsoon: influence of river discharge. Journal of Oceanography 69.

Sarmiento, J.L., Herbert, T., 1988. Mediterranean nutrient balance and episodes of anoxia. Global Biogeochemical Cycles 2, 427–444.

Schott, F., Dengler, M., Schoenefeldt, R., 2002. The shallow overturning circulation of the indian ocean. Progress in Oceanography 53, 57–103.

Schott, F., McCreary, J.P.J., 2001. The monsoon circulation of the indian ocean. Progress in Oceanography 51, 1 – 123.

Shankar, D., Vinayachandran, P.N., Unnikrishnan, A.S., 2002. The monsoon currents in the north indian ocean. Progress in Oceanography 52, 63–120.

Smith, R., Jones, P., Briegleb, B., Bryan, F., Danabasoglu, G., Dennis, J., Dukowitz, J., Eden, C., Fox-Kemper, B., Gent, P., Hecht, M., Jayne, S., Jochum, M., Large, W., Lindsay, K., Maltrud, M., Norton, N., Peacock, S., Vertenstein, M., Yeager, S., 2010. Parallel ocean program (POP) reference manual.

Stramma, L., Johnson, G.C., Sprintall, J., Mohrholz, V., 2008. Expanding oxygen-minimum zones in the tropical oceans. Science 320, 655–658.

Stramma, L., Oschlies, A., Schmidtku, S., 2012. Mismatch between observed and modeled trends in dissolved upper-ocean oxygen over the last 50 yr. Biogeosciences 9, 4045 – 4057.

Stramma, L., Schmidtko, S., Levin, L.A., Johnson, G.C., 2010. Ocean oxygen minima expansions and their biological impacts. Deep-Sea Research I 57, 587–595.

Swallow, J.C., Pollard, R.T., 1988. Flow of bottom water through the madagascar basin. Deep-Sea Research 35, 1437–1440.

Swift, S.A., Bower, A.S., 2003. Formation and circulation of dense water in the persian/arabian gulf. Journal of Geophysical Research 108, 4–1:4–15.

Talley, L.D., McCartney, M.S., 1982. Distribution and circulation of labrador sea water. Journal of Physical Oceanography 12, 1189–1205.

Teng, Y.C., Primeau, F.W., Moore, J.K., Lomas, M.W., Martiny, A.C., 2014. Global-scale variations in the carbon to phosphorus ratio of exported marine organic matter. in prep .

Thiele, G., Sarmiento, J.L., 1990. Tracer dating and ocean ventilation. Journal of Geophysical Research 95, 9377–9391.

Toggweiler, J.R., Dixon, K., Bryan, K., 1989a. Simulations of radiocarbon in a coarse-resolution world ocean model 1. steady state prebomb disributions. Journal of Geophysical Research 94.

Toggweiler, J.R., Dixon, K., Bryan, K., 1989b. Simulations of radiocarbon in a coarse-resolution world ocean model 2. distributions of bomb-produced carbon 14. Journal of Geophysical Research 94, 8243–8264.

Tomczak, M., Godfrey, J.S., 2003. Regional Oceanography: an Introduction. Daya Publishing House, Delhi. second edition.

Trenberth, K.E., Stepaniak, D.P., 2001. Indices of el nino evolution. Journal of Climate 14, 1697–1701.

Vaquer-Sunyer, R., Duarte, C.m., 2008. Thresholds of hypoxia for marine biodiversity. Proceedings of the National Academy of Sciences 105, 15452–15457.

Ward, B.B., Devol, A., Rich, J.J., Chang, B.X., Naik, H.S., Pratihary, A.K., Jayakumar, A., 2009. Denitrification as the dominant nitrogen loss process in the arabian sea. Nature 461, 78–81.

Waugh, D.W., Hall, T.M., Haine, T.W.N., 2003. Relationships among tracer ages. Journal of Geophysical Research 108, 3138.

Whitney, F.A., Freeland, H.J., Robert, M., 2007. Persistently declining oxygen levels in the interior waters of the eastern subarctic pacific. Progress in Oceanography 75, 179–199.

Wishner, K., Levin, L., Gowing, M., Mullineaux, L., 1990. Involvement of the oxygen minimum in benthic zonation on a deep seamount. Nature 346, 57–59.

Wyrtki, K., 1962. The oxygen minima in relation to ocean circulation. Deep-Sea Research 9, 11–23.

Yakushev, E.V., Neretin, L.N., 1997. One-dimensional modeling of nitrogen and sulfer cycles in the aphotic zones of the black and arabian seas. Global Biogeochemical Cycles 11, 401–414.

Yamanaka, Y., Tajika, E., 1996. The role of the vertical fluxes of particulate organic matter and calcite in the oceanic carbon cycle: Studies using an ocean biogeochemical general circulation model. Global Biogeochemical Cycles 10, 361–382.